

Influence of Soot on the Transport Mechanisms inside the Filter Wall of SCR-Coated Diesel Particulate Filters

Von der Fakultät für Physik und Geowissenschaften
der Universität Leipzig

genehmigte

DISSERTATION

zur Erlangung des akademischen Grades

DOCTOR RERUM NATURALIUM

(Dr. rer. nat.)

vorgelegt

von M. Sc. Marcus Purfürst

geboren am 10.03.1988 in Schleiz

Gutachter:

Prof. Dr. Marius Grundmann (Universität Leipzig)

Prof. Dr. Olaf Deutschmann (Karlsruher Institut für Technologie)

Tag der Verleihung: 23.04.2018

Bibliographic Description

Purfürst, Marcus

Influence of Soot on the Transport Mechanisms inside the Filter Wall of SCR-Coated Diesel Particulate Filters

Universität Leipzig, Dissertation, 2018

123 pages, 178 references, 66 figures, 6 tables

The effect of soot on the catalytic properties of a diesel particulate filter coated with a catalyst for the selective catalytic reduction of NO_x with ammonia (SDPF) was studied by means of model-gas experiments. After loading of the SDPF with model soot from 0 to 10 g l^{-1} , the NH_3 storage as well as the catalytic DeNO_x behavior of the standard SCR reaction was investigated. The model soot present in the filter was shown to have an NH_3 storage capacity. The soot deposit inside the SDPF filter wall lead to a decreased NO conversion in SCR experiments of up to 20 %. The NH_3 breakthrough was found to be shifted towards earlier time-on-stream during NH_3 adsorption on soot loaded SDPF samples. Both effects could be attributed to a diffusive mass transport limitation of the gas species through the soot to reach at the chemically active sites inside SDPF filter wall. The self-diffusion coefficient of NH_3 probe molecules within a soot layer could be measured using Pulsed Field Gradient-NMR technique. The unit collector model is capable of describing the backpressure upon soot loading with a depth filtered (inside filter wall) soot amount of 1 g l^{-1} and 0.36 g l^{-1} , respectively, for both SDPF types under investigation. Based on Scanning Electron Microscopy (SEM) investigation a 1-D microscopic soot filter wall-model was set up. The model implies soot as diffusion barrier for mass transport. It was calibrated based on experimental observations and allows to conclude on the distribution of the soot within the filter wall. Thus, a high soot-coverage of the porous filter wall close to the inlet channel, a slightly covered middle part and a soot free zone close to the outlet explains the observed reduction in NO conversion as well as the NH_3 breakthrough at earlier time-on-stream during NH_3 adsorption experiments for SDPF samples loaded with soot. A modelled homogeneous soot distribution ($0.6 \mu\text{m}$ soot layer on top of washcoat) within the whole SDPF was shown to result in NO conversion drop up to 45 %.

Keywords

selective catalytic reduction, diesel particulate filter, soot, temperature programmed desorption of ammonia, kinetic modelling, diffusion, PFG-NMR

Statement of Authorship

I hereby declare that this doctoral thesis is the result of my own work, unless otherwise acknowledged in the text. All references and verbatim extracts have been quoted, and all sources of information have been specifically acknowledged. This thesis has not been submitted for any other degree.

This work was prepared between August 2013 and April 2017 under the supervision of Prof. Dr. Roger Gläser (Faculty of Chemistry and Mineralogy, Universität Leipzig) and Prof. Dr. Marius Grundmann (Faculty of Physics and Earth Sciences, Universität Leipzig).

Leipzig, 23.04.2017

A handwritten signature in blue ink, appearing to read 'M. Purfürst', with a stylized flourish at the end.

Marcus Purfürst

Acknowledgements

At first, I would like to thank my supervisor Prof. Dr. Roger Gläser for establishing the cooperation between the IAV GmbH and the Institute of Chemical Technology (ITC), Universität Leipzig. Although my previous career started in the physics department, he put his trust in me to broaden my scope. So, I had the possibility to treat a very relevant and application-related topic on catalysis for the automotive industry. I greatly thank him for his scientific advice and guidance. Furthermore, a big thank goes to Prof. Dr. Marius Grundmann. He was my former supervisor during my master thesis in the semiconductor physics group at Universität Leipzig. I am very thankful, that he, without any hesitation, agreed to review my Ph.D. thesis for the physics department, although it was mainly crafted in the chemistry department under the guidance of Prof. Gläser. His nice advice concerning the Ph.D. examination process has to be mentioned, too. Also, the support of PD Dr. Rustem Valiullin should be acknowledged. He performed the PFG-NMR measurements on my samples.

My very big gratitude goes to Prof. Dr. Kay-Jochen Langeheinecke and Dr. Sergej Naumov as representatives for the IAV GmbH. I thank them for choosing me as the candidate for the industrial cooperation, for their trust and especially for all the financial support I received from IAV during my Ph.D. work. I would like to offer my sincere thanks to Sergej for all the scientific discussions and advice, for his support and finally for his encouragement. Also, the help of Ilya Semenov has to be acknowledged.

I have been very lucky to share my office and the laboratory with very interesting and helpful people. Special thanks go to Thomas Rammelt, Robert Echrich, Karl Skadell, Eric Ebersbach, Felix Link, Erisa Saraci as well as Dr. Jürgen Böhm for their practical and mental help. Nevertheless, all the members of the ITC are acknowledged for their support in scientific, technical or bureaucratic issues.

The financial support of the Research Academy Leipzig (RAL) and the Graduate School Build MoNa to attend scientific conferences are greatly acknowledged. I am thankful for the possibility to take part in very interesting scientific workshops.

This work would not have been possible without the love and support of my family and my friends. I received so much love, friendship and freedom to do the things I wanted to do. It's you, making my life worthy to live. My deepest gratitude goes to my fiancée, Laura. I enjoyed all the moments together with you and I look forward for the things to come.

Table of Contents

1	Introduction and Objectives	8
2	Literature Overview	11
2.1	Exhaust Gas Aftertreatment for Diesel Engines	11
2.1.1	Challenges and Emission Legislation	11
2.1.2	Components and Principles	15
2.2	Selective Catalytic Reduction of Nitric Oxides	17
2.2.1	State-of-the-art Catalysts	18
2.2.2	Novel Catalysts	21
2.3	Diesel Particulate Filters	22
2.3.1	Soot Particles	24
2.3.2	Material Properties and Pressure-Drop	26
2.4	SCR-coated Diesel Particulate Filter	35
2.5	Gas Diffusion through Soot	37
3	Experimental Section	38
3.1	Materials	38
3.1.1	Preparation	38
3.1.2	Dissolution of the zeolite from the SDPF	40
3.2	Characterization	40
3.2.1	Hg-Intrusion on SDPF Sample	40
3.2.2	Scanning Electron Microscopy of SDPF Sample	40
3.2.3	Pulsed Field Gradient Nuclear Magnetic Resonance on Model Soot	41
3.3	Soot Loading Apparatus	42
3.3.1	Set-up	43
3.3.2	Soot Characterization	45
3.3.3	Soot loading procedure for the Particulate Filters	46
3.4	Catalytic Characterization using Model Gas Experiments	47

3.4.1	Pretreatment, Regeneration and Hydrothermal Ageing	48
3.4.2	Temperature Programmed Desorption of NH ₃	48
3.4.3	Standard-SCR-Experiments.....	49
3.4.4	NO Adsorption Experiments on NO _x Storage Catalyst	49
4	Modelling.....	50
4.1	Mathematical Model.....	50
4.2	Kinetic Model	56
4.3	Model Environment and Calibration	59
5	Results and Discussion	60
5.1	Model-Soot.....	60
5.1.1	NH ₃ -Storage Capacity of the Model Soot	61
5.1.2	Catalytic Properties: NH ₃ -SCR	62
5.1.3	Gas Diffusion through a Soot Layer	63
5.2	SDPF Sample.....	65
5.2.1	NH ₃ Storage Capacity	65
5.2.2	Activity of SCR-DeNO _x	75
5.3	Modelling.....	79
5.3.1	Backpressure.....	79
5.3.2	Adsorption of NH ₃ on soot free SDPF samples.....	80
5.3.3	Influence of in-wall Soot Distribution on the Adsorption of NH ₃	83
5.3.4	Influence of in-wall Soot Distribution on the SCR DeNO _x Behavior	90
5.3.5	Adaption to Flow-Through Catalysts	102
6	Conclusions and Outlook.....	107
7	References	109
8	Appendix	116
8.1	Additional Data.....	116
8.2	Curriculum Vitae.....	124

8.3	List of Publications.....	125
8.3.1	Oral Presentations.....	125
8.3.2	Journal Publications.....	125
8.3.3	Poster Presentations	125

List of Abbreviations

cpsi	Cells per square inch
CRT	Continuous Regeneration Trap
DOC	Diesel Oxidation Catalyst
EEPS	Engine Exhaust Particle Sizer
EGR	Exhaust Gas Recirculation
FTIR	Fourier Transform Infrared Spectrometer
MSS	Micro Soot Sensor
NEDC	New European Driving Cycle
NMR	Nuclear Magnetic Resonance
NSC	NO _x Storage Catalyst
OP	Operation Point of soot-generator
PAH	Polycyclic aromatic hydrocarbon
PFG	Pulsed Field Gradient
RDE	Real Driving Emissions
SCR	Selective Catalytic Reduction
SDPF	SCR-coated Diesel Particulate Filter
SEM	Scanning Electron Microscopy
TPD	Temperature Programmed Desorption
VWT	Vanadium-, tungsten-, titanium-oxides
wc	Washcoat
WLTP	Worldwide harmonized light vehicle test procedure

List of Symbols

Symbol	Unit	Meaning
α	-	NH ₃ -to-NO _x ratio
β	m s ⁻¹	Mass transfer coefficient
γ	-	NO ₂ -to-NO _x ratio
Γ_j	mol m ⁻³ _{wc}	NH ₃ storage capacity of storage site j
Δp	Pa	backpressure
ϵ	-	porosity
θ_j	-	NH ₃ storage filling ratio (0...1) of storage site j
λ	m	Mean free path
λ	-	air-fuel equivalence ratio
μ	kg m ⁻¹ s ⁻¹	Exhaust gas dynamic viscosity
ν	m ² s ⁻¹	Kinematic viscosity
ν	-	Diffusion volume (tabulated in [1])
ρ	kg m ⁻³	density
τ_k	-	Tortuosity of gas specie k through soot
ϕ	-	Saturation coefficient
χ	-	Shape factor
ψ	-	Percolation factor
A_i	s ⁻¹	Pre-exponential factor of reaction i
A_f	m ²	Filtration area
A_{wc}	m ²	Surface area of washcoat per collector cell
A_s	m ²	Surface area of the soot in a collector cell
$c_{id, gas}$	mol m ⁻³	Molar concentration of an ideal gas
D	m	Channel width
d_c	m	Collector unit diameter
d_{cell}	m	Collector cell diameter
d_s	m	Thickness of in-wall soot layer (varying between bricks)
$D_{eff, k}$	m ² s ⁻¹	Effective diffusion coefficient of gas specie k through soot
$D_{s/g}$	m ² s ⁻¹	Surface diffusivity (s) or gaseous phase diffusivity (g)

d_p	m	Pore width
$E_{A,i}$	kJ mol^{-1}	Activation energy of reaction i
E_{DA}	kJ	Adsorption energy (Dubinin-Astakhov)
$f()$	-	Kuwabara function
G_i	-	Inhibition constant of reaction i
k	m^2	Permeability of porous medium (soot layer or filter wall)
k_i	s^{-1}	Reaction rate constant of reaction i
Kn	-	Knudsen number
\dot{m}	kg h^{-1}	Mass flow
$\dot{m}_{\text{soot,OP}}$	kg h^{-1}	Mass flow of soot in Operation Point
m_{soot}	g l^{-1}	Soot mass loaded in the sample per liter sample volume
$m_{\text{soot,wall}}$	g l^{-1}	Soot mass loaded in the filter wall per liter sample volume
$m_{\text{s,cell}}$	kg	Soot mass in collector cell
$m_{\text{s,sat,cell}}$	kg	Saturation mass of collector cell
MW_k	kg mol^{-1}	Molecular weight of gas specie k
N	-	Total number of open channels
n_{cell}	-	Number of collector cells
n	-	Heterogeneity parameter (or Astakhov exponent)
$p_{1,2}$	Pa	Pressure at inlet channel (1) / outlet channel (2)
$p_0(T)$	kPa	Saturation vapor pressure at temperature T
p	kPa	Equilibrium pressure
$p_{s/g}$	-	Relative weight of diffusivity (s–surface, g–gaseous phase)
q	m^{-1}	Magnetic field gradient intensity (for PFG-NMR)
q_0	g l^{-1}	Maximum mass of adsorbed species per unit volume of sorbent
$q(p)$	g l^{-1}	Mass of adsorbed species at equilibrium pressure p
R	$\text{J mol}^{-1} \text{K}^{-1}$	Universal gas constant
r	m	Radius
r_i	s^{-1}	Reaction rate of reaction i
S	-	Spin-echo diffusion attenuation
SCF	-	Stokes-Cunningham factor
s_{ki}, s_{ji}	-	Stoichiometric coefficient
T	K	Absolute temperature

T_{ads}	K	Temperature at adsorption
t_d	s	Diffusion time
V_{sample}	m^3	Volume of the sample
$V_{\text{s,layer}}$	m^3	Volume of the soot accumulation zone in a collector unit
\dot{V}	$\text{m}^3 \text{ h}^{-1}$	Gas volume flow rate through sample
V_{void}	m^3	Void volume per collector cell
V_{wc}	m^3	Volume of washcoat per collector cell
v_w	m s^{-1}	Filter wall velocity
w	m	Filter wall thickness
w_s	m	Soot cake layer thickness in inlet channel
$x_{\text{in},k}$	-	Molar fraction of gas specie k entering one brick (for brick #1, $x_{\text{in},k}$ equals the molar fraction in the inlet channel, otherwise it equals the outlet molar fraction of the brick above)
$x_{g,k}$	-	Molar fraction of gas specie k in void of the porous wall of one brick
$x_{s,k}$	-	Molar fraction of gas specie k at surface of soot layer inside the porous wall of one brick
$x_{wc,k}$	-	Molar fraction of gas specie k at the washcoat within the brick
$y(j)$	ppm	Volume fraction (concentration) of gas species j

Subscripts**Meaning**

g	Exhaust gas
i	Reaction number
j	Storage site
k	Gas specie
pl	Particulate cake layer
s	soot
w	Porous wall with soot
w_o	Porous wall (soot free)
w, e	Porous wall with areas being soot free and areas being soot loaded

1 Introduction and Objectives

In 2009 the German federal government accepted the European regulation for the reduction of CO₂ emitted by passenger cars. The main goal is the achievement of a maximum CO₂ emission of 95 g km⁻¹ until 2020. Due to the higher fuel efficiency of the diesel engine compared to the gasoline engine, diesel-technology became indispensable for the car manufacturers to reach their CO₂ fleet emission goals. The appropriate manufacturers marketing strategy combined with a positive technological development of the diesel engines regarding driving comfort, dynamics and fuel consumption led to a high costumers acceptance over the past years, resulting nowadays in a share of 33 % of diesel engine cars in the passenger car sector in Germany. In the truck and transportation sector the diesel engine is since the year dot the powertrain of choice due to its fuel efficiency and possibility to fulfill the special demands for transportation vehicle.

The main drawback of a diesel engine is the elevated amount of particulate matter and NO_x emissions compared to a gasoline engine. This results from a higher temperature regime and an overstoichiometric availability of oxygen under which the diesel fuel is burned. Changes in the in-engine combustion process merely either lead to low NO_x and high particle production or *vice versa*, which is known as the NO_x-particle trade-off. Although recent improvements in the combustion process due to improved diesel injection strategies as well as exhaust gas recirculation (EGR) resulted in lower engine-out NO_x levels, a combined exhaust gas aftertreatment system for the abatement of particulate matter and NO_x is absolutely essential to fulfill current emission legislations (see **Fig. 1**). For the particulate reduction the diesel particulate filter (DPF) has been developed. It features a very high filtration efficiency (close to 100 % of the particulate mass emitted). Nevertheless, from time to time the collected soot-particles need to be removed by so called regeneration, which is a heat induced oxidation of the carbon. Driven by immense effort of the catalyst scientific community the selective catalytic reduction (SCR) of NO_x could be established in vehicle application for the NO_x abatement. The SCR active catalyst combined with a system for the injection of a NO_x reducing agent into the exhaust gas were positioned within the exhaust branch. Thereby, ammonia (NH₃) is used as the reducing agent. As it is toxic and due to technical challenges, an aqueous urea solution, called AdBlue®, has been chosen to provide the NH₃ on road. Both, the DPF

and the NH_3 -SCR are nowadays the state-of-the-art exhaust gas aftertreatment technology for passenger cars and trucks.

For the fulfillment of more and more stringent emission legislation, especially in the passenger car sector, technical and economic demands have forced the development of new technologies and strategies for emission reduction. As a conventional SCR system, which is positioned downstream the engine, has problems to achieve enough temperature for high NO_x conversion rates, the combination of the SCR-catalyst on the DPF (component called SDPF) could be located close to the engine for improved thermal management. Otherwise the application of only one component for abatement of both harmful species (NO_x and particulates) has its advantage in lower costs and weight. As in the combined system the soot filtration is realized in close vicinity to the active sites for the catalytic De NO_x reaction, a negative interaction of both functionalities is highly probable. To fully benefit from the whole potential of the SDPF included in a vehicles exhaust gas aftertreatment system, a fundamental understanding of the physico-chemical mechanisms inside the SDPF is indispensable. Only a scientifically correct adoption of the onboard control strategies will ensure low emission levels of harmful species to protect the environment.

In this work the influence of soot on the NH_3 -SCR De NO_x reaction inside the porous filter wall of an SDPF is investigated in detail. On one hand, NH_3 storage is the fundamental process responsible for the reduction of NO_x . On the other hand, a change in the NH_3 adsorption behavior will result in a changed NH_3 slip at the outlet of the SCR-catalyst, which is to be avoided due to its toxicity.

So, one aim of this work is to study the NH_3 adsorption process on a soot loaded SDPF. Another aim is a comprehensive study on the soot induced changes in the SDPFs NO_x conversion. In order to realize investigations on soot loaded filter samples, a soot loading apparatus based on a model soot-generator was set up and is reported here. A contribution of the soot itself to the SDPFs NH_3 storage capacity as well as an interaction of the soot to the SCR-De NO_x reaction is studied. The fundamental microscopic processes inside the filter wall are explained by means of a physico-chemical model. An implementation of a chemical model in the unit collector cell model is, to the best of our knowledge, reported the first time in literature to explain the processes inside the SDPF. Hereby the soot is implemented as a diffusion barrier for the gas transport to the

catalytically active sites. The diffusive barrier was approved by means of pulsed field gradient nuclear magnetic resonance (PFG-NMR) studies. Finally, the results are evaluated regarding their practical relevance for real vehicle application.

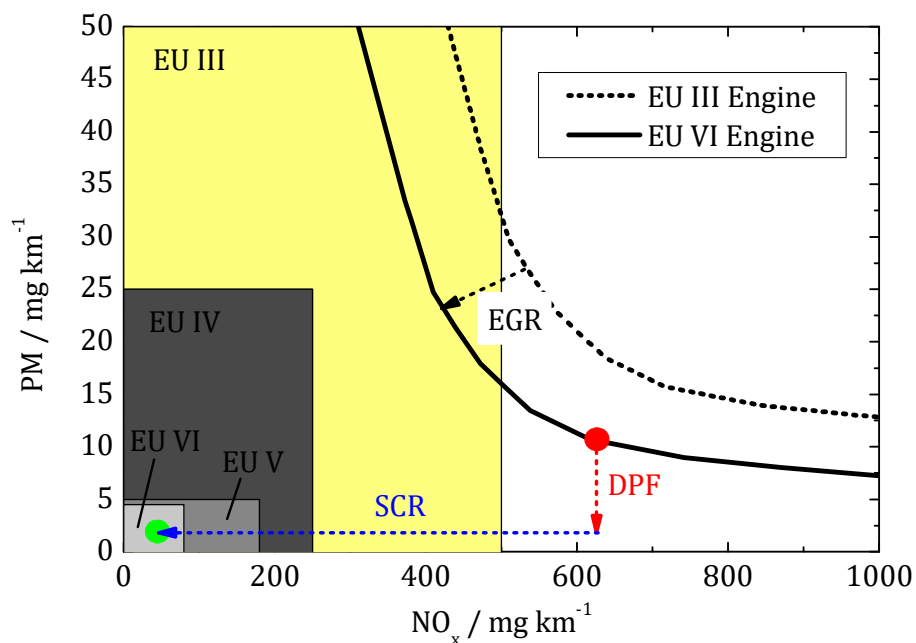


Fig. 1 Engine-out emission trade-off for particulate matter vs. NO_x (black line). The red and blue arrows indicate the exhaust gas aftertreatment by means of the particulate filter and the SCR-DeNO_x to fulfill current European emission legislation (depicted as rectangles).

2 Literature Overview

2.1 Exhaust Gas Aftertreatment for Diesel Engines

2.1.1 Challenges and Emission Legislation

In 1992 the European Union established the emission legislation for passenger cars and heavy duty vehicle [2]. Thus, the manufacturers were forced to develop exhaust gas aftertreatment techniques to ensure low emission of harmful pollutants in Europe. Compared to gasoline engines, the raw exhaust of diesel engines contains less pollutants and much more oxygen (see **Fig. 2**) [3,4]. The main pollutants are carbon monoxide (CO), partially oxidized hydrocarbons (HC), particulate matter (PM or soot) and nitric oxides. CO, HC and PM are the result of an incomplete combustion of the fuel. Whereas the nitric oxides are formed at peak temperatures of 1300 K within the combustion chamber. The NO_x-formation in detail is described by the extended ZELDOVICH-mechanism [5,6]. Although the sulfur content of the diesel fuel is restricted [7], sulfur dioxide (SO₂) is a result of its oxidization during combustion.

The European Environment Agency analyzed the emissions data of all the 28 member states between 1990 and 2014 [8]. Thereby, in 2014, 39 % of all the NO_x released in the environment were caused by the road transportation sector with an equal share between passenger cars and the heavy duty vehicles (including buses). Furthermore 13 % of all the particulate matter were emitted by vehicles.

The health risks of combustion engine emissions are widely discussed in literature. Carbon monoxide is a respiratory poison to human bodies. Even low doses cause headaches and the impairment of the manual coordination when breathed in [9]. Hydrocarbons are in debate to support cancer formation [10]. Nitric oxides are known to cause cellular damages on mammalian cells. Its cytotoxicity originates from the formation of peroxynitrite out of NO, which reacts with DNA or proteins and thus supports several diseases [11,12]. Furthermore NO₂ and SO₂ could cause acid rain, which is harmful for humans and the environment [13]. Particulate matter emission from vehicles are in the focus as a health risk for the formation of allergies, airway inflammation, cardiopulmonary disease and even lung cancer [14,15]. Engine out particles consists of inorganic and organic constituents. Therefrom especially the polycyclic aromatic hydrocarbons (PAH) are known to damage human DNA, causing several serious diseases

[16]. Due to the individual health risks of each component discussed above, in 2012 the International Agency for Research on Cancer classified the exhaust gases from diesel engines to be carcinogenic to humans [17,18]. This emphasizes the importance of an ongoing development in the field of exhaust gas aftertreatment to ensure low emissions.

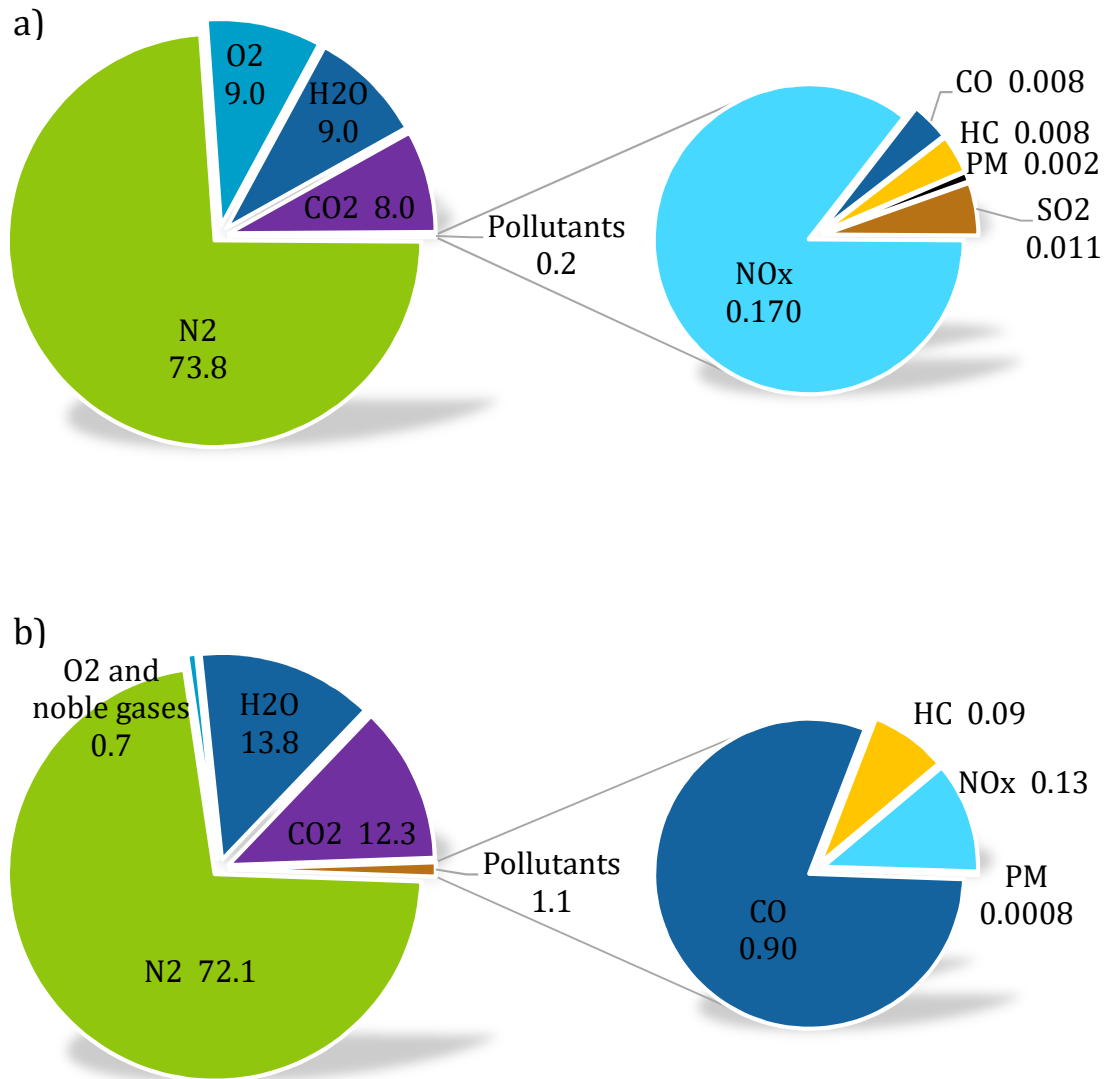


Fig. 2 Typical raw exhaust gas composition (number in volume percent) of a diesel engine a) and a gasoline engine b) [4]. Original illustration based on [5].

However the operation conditions for diesel and for gasoline vehicles differ [4]. One measure for the process of the combustion is the air-fuel equivalence ratio λ (2.1). An excess of oxygen during combustion is called »lean« ($\lambda > 1$), an excess of fuel is called »fat« ($\lambda < 1$).

$$\lambda = \frac{\dot{m}_{\text{air}}}{\dot{m}_{\text{air,stoichiometric}}} \quad (2.1)$$

Regulated by the throttle valve a gasoline engine is usually operated at $\lambda=1$ [5]. The state-of-the-art aftertreatment component is a three-way catalytic converter, which oxidizes HC and CO while reducing NO_x over Platinum-Palladium (Pt-Pd) active sites [19,20]. In diesel engines on the other hand, the fuel is injected and burned under oxygen excess, usually at $\lambda>2$. Despite this oxygen rich condition HC, CO and PM are being formed. This is caused by local inhomogeneities in the cylinder-mixture between $\lambda=0$ and $\lambda=8$. The elevated temperature regime and oxygen partial pressure during diesel combustion (compared to gasoline) favor the NO_x formation [3]. Nevertheless, the exhaust gas recirculation (EGR), patented already in the 1972, offers an in-engine technique to reduce the raw emission of NO_x and is nowadays the standard for new diesel passenger cars. Thereby, raw exhaust gas recirculates in the cylinder and lowers the flame temperature and oxygen concentration [21]. The drawback is an increased PM emission, due to the reduced oxygen concentration. The so-called PM-NO_x trade-off describes the principle, that an increased temperature leads to less PM but favors the NO_x formation and *vice versa* (see **Fig. 1**) [3]. Changing the combustion condition cannot simultaneously result in reduction of both, PM and NO_x. Also, HC and CO cannot be fully avoided by means of in-engine methods. Consequently, an exhaust gas aftertreatment system is essential for diesel engines.

Besides the regulations for CO₂ abatement [22,23], the European Union defines the emission standards for light and heavy duty vehicles [4,24,25]. To ensure improving air quality as well as an ongoing development in the exhaust gas aftertreatment sector, the emission levels are decreased in regular intervals. At introduction of the Euro 1 standard in 2012, the emission levels were the same for gasoline and diesel engines. Recent emission standards for diesel engines are more stringent in CO standards but allow higher NO_x emissions. **Tab. 2.1** gives the development of the European emission standards for diesel passenger cars. While gasoline engines were excluded from PM emission standards until Euro 4, the introduction of the Euro 5 level ensures low particulate emission of 0.005 mg km⁻¹ for both (gasoline and diesel). Since in 2014 the current Euro 6 standard was approached, especially the manufacturers of diesel engines phase the very challenging goal of 80 mg km⁻¹ NO_x as well as a limit for the number of emitted particles. These goals could not be fulfilled with pure in-engine techniques to prevent emissions. An

exhaust gas aftertreatment system is absolutely essential. Until 2017 the emissions are tested over predefined driving cycles (e.g. the New European Driving Cycle (NEDC) or the Worldwide harmonized light vehicle test procedure (WLTP) [26]. Between 2017 and 2021 the Real Driving Emission Test (RDE) will be introduced for emission legislation. This test procedure will ensure vehicle emissions in real operation, outside a laboratory testing setup [27]. Recently huge discrepancies between the emission test results of the emission legislation test in the laboratory and the RDE test results culminated in a crisis for diesel engines. It was revealed by West Virginia University in 2014, which published RDE test results [28].

Tab. 2.1: Emission standards for diesel passenger cars in Europe. The table is based on [29].

Tier	Date	CO / g km ⁻¹	HC / g km ⁻¹	HC+NO _x / g km ⁻¹	NO _x / g km ⁻¹	PM / g km ⁻¹	PN / # km ⁻¹
Euro 1	1992	2.72	-	0.97	-	0.1400	-
Euro 2	1996	1.00	-	0.70	-	0.0800	-
Euro 3	2000	0.64	-	0.56	0.50	0.0500	-
Euro 4	2005	0.50	-	0.30	0.25	0.0250	-
Euro 5	2009	0.50	-	0.23	0.18	0.0050	-
Euro 6	2014	0.50	-	0.17	0.08	0.0045	6 · 10 ¹¹

Fig. 3 shows the development of the number of new registered cars in Germany over the last decade. In 2015 diesel engine cars have a market share of 48.0 %, while 50.2 % of all new registered vehicles have a gasoline engine. Although the German government forces the development of electric powertrain vehicles, their market share in 2015 merely is 0.48 % for pure electric cars and 1.05 % for hybrid cars. In future their market will certainly grow and they will play a major role in the transportation sector. But over the last decade until now, the market is still dominated by fuel burning engines. Even after the diesel scandal became known to the public in 2015, the number of new registered diesel cars in Germany increased from 122558 (May 2015) to 132758 (May 2016), which is a plus of 8.3 % [30]. So, diesel engine cars have still a positive awareness of the costumers and they are very important for the manufacturers to reach their fleet CO₂ emission goals. A change in the transportation sector towards electric engines will be a

slow process. Hence the research on the field of the exhaust gas aftertreatment for diesel engines is very important to ensure low emission under all testing conditions to ensure a clear environment.

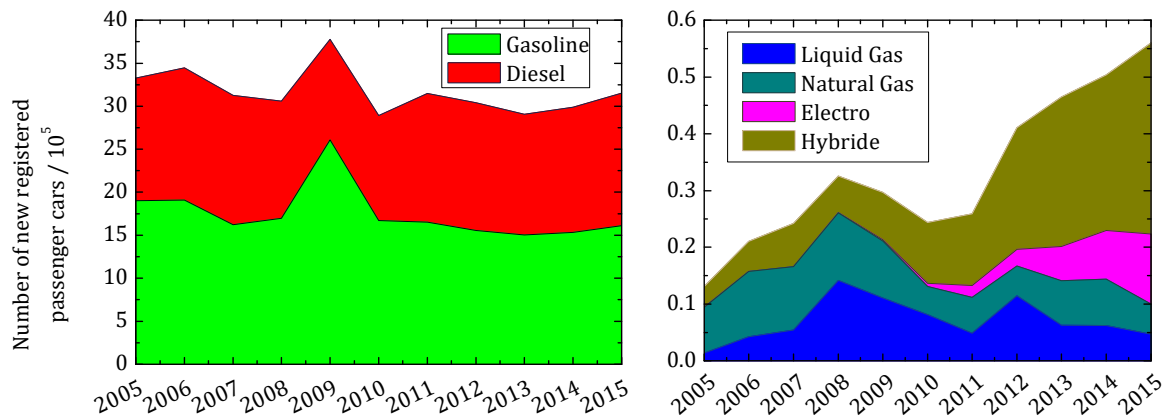


Fig. 3 Statistics of the number of new registered passenger cars in Germany from 2005 to 2015 in terms of powertrain technology. Left: Diesel and gasoline engines, right: alternative powertrain technologies. The illustration is based on data from the Kraftfahrt-Bundesamt [31].

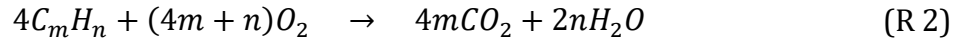
2.1.2 Components and Principles

Within this subchapter the Diesel Oxidation Catalyst (DOC) and the NO_x Storage Catalyst (NSC) are briefly described. As the main focus of this work are studies on SCR coated DPFs, the principles of the selective catalytic reduction of NO_x, the soot filtration in DPF and its combination, the SDPF, will be described in extra chapters. All these five above mentioned exhaust gas aftertreatment components characterize the state-of-the-art principles applied for abatement of diesel engine emissions [3].

2.1.2.1 Diesel Oxidation Catalyst

Today an oxidation catalyst is incorporated in the aftertreatment system of almost all vehicles [4,32]. It consists of a flow-through monolith with 400 to 800 cpsi (cells per square inch). The walls are washcoated with a material providing high surface area *e.g.* Al₂O₃, which carries the catalytically active particles [4]. Due to the lean engine operation of a diesel engine, compared to the stoichiometric operated gasoline engine, it emits much less HC and CO. A DOC is able to abate nearly all of the raw CO (R 1) and HC (R 2) emissions [3]. In contrast to the Three-Way-Catalysts (TWC) used for gasoline engines, a reduction of NO_x is not possible due to the higher volume fraction of O₂ in the diesel exhaust gas [4]. The excess of oxygen even leads to an oxidation of NO to NO₂ (R 3), which is beneficial for

downstream aftertreatment systems like SCR-catalysts (see chapter 2.2) or DPF (see chapter 2.3).



The common choice for the catalyst are platinum particles with diameters of 5 to 20 nm [4,33,34], offering light-off temperatures relevant for automotive purpose. Nevertheless, their drawback is the sintering ongoing with a loss in catalytic activity by thermal ageing [35]. The use of bimetallic Pt/Pd DOCs offers several advantages. Palladium is much cheaper than Platinum and significantly stabilizes against sintering associated with much higher activity after the thermal ageing [36,37]

2.1.2.2 NO_x Storage Catalyst

As NO_x Storage Catalysts are potent NO_x adsorbers even at room temperature [38], they offer high potential for abatement of NO_x emissions during engine cold-start. Next to Pt or Rd catalyst particles [39,40], a further storage component *e.g.* alkali metals or earth alkaline metals are washcoated on the monolith (compare **Fig. 4**). This component is able to adsorb NO_x as a nitrate. Barium as storage component is present as BaCO₃ in the CO₂ rich atmosphere of the exhaust [41,42]. During lean engine operation, NO_x are stored as BaNO₃ at the outer shell of the BaCO₃ particles. In regular intervals the NSC has to be regenerated. During fat engine operation condition the present reducing agents *e.g.* HC, CO and H₂ release the stored NO_x from the BaCO₃ followed by their reduction over the Pt-catalyst. Compared to NH₃-SCR, the NSC is a simple technique for NO_x abatement, as no additional reducing agent has to be provided by a tank. Nevertheless, due to the Pt/Rd particles, it is expensive. A further problem, similar to DOCs, is the deactivating due to catalyst ageing or poisoning by SO₂ [43]. If barium sulfate has formed at the surface of a Barium particle, it is no longer active for NO_x storage.

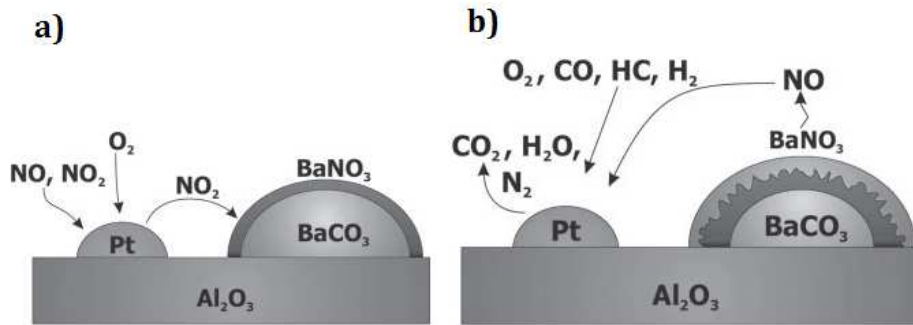
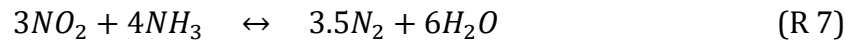
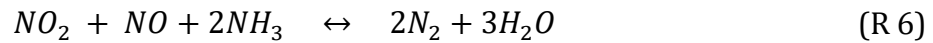
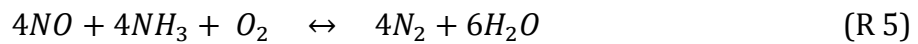
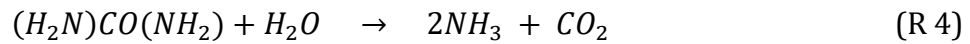


Fig. 4 Pt and BaCO_3 particles on the catalytic surface of a NSC: a) illustrates the principle of NO_x storage during lean engine operation, b) shows the regeneration of the storage catalyst. The illustration originates from [3].

2.2 Selective Catalytic Reduction of Nitric Oxides

An effective way to reduce NO_x from gas phase is the selective catalytic reduction (SCR) of NO and NO_2 to N_2 [4]. One measure for the performance of an SCR system is the light-off temperature (T_{50}), which characterizes the lowest temperature at which the catalyst shows 50 % NO_x conversion. As reducing agent for this heterogeneous catalytic reaction hydrogen (H_2), hydrocarbons (HC), ethanol and ammonia (NH_3) are widely discussed in literature. Metal-ion exchanged zeolites *e.g.* Pd/ZSM-5 or Co/ZSM-5 in combination with HC as reducing agent showed NO conversion of up to 70 % at temperatures above 600 °K as well as high selectivities towards the N_2O formation. Similar results were also found for HC -SCR on other metal/zeolite combinations [44,45], making them not suitable for the demands of the automotive industry, where high NO_x conversion rates (close to unity), low N_2O formation and early light-off (below 450 K) is mandatory. Also ethanol-SCR over $\text{Ag}/\text{Al}_2\text{O}_3$ catalysts could not fulfill the requirements of automotive application, as the light-off is at 520 K or above [46,47]. With the current state of technology, NH_3 is used as reducing agent. Since 2004 the first trucks were equipped with NH_3 -SCR technology. The NH_3 is usually generated *in situ*. An aqueous solution of urea (32.5 %, named »AdBlue®«) is injected in the hot exhaust and decomposes by hydrolysis (R 4) [48]. Although an additional tank for AdBlue has to be installed in the car, its advantage is the safety issue, as there is no need for the transportation of compressed NH_3 . The acidic catalysts for SCR are washcoated on flow-through monoliths. They are characterized by high NH_3 adsorption capacity [49,50]. The reduction of NO with NH_3 (R 5) is described by the so called »Standard SCR reaction« [51]. At NO_2 -to- NO_x ratio, $\gamma = \frac{n(\text{NO}_2)}{n(\text{NO}_x)}$, of 0.5, NO_x are converted to N_2 by the so-called »Fast SCR reaction« (R 6), which is about ten times faster

than (R 5) [52,53]. Both have a NH_3 -to- NO_x stoichiometry of $\alpha = \frac{n(\text{NH}_3)}{n(\text{NO}_x)} = 1$. As the DOC oxidizes NO to NO_2 , adjusting the NO_2 -to- NO_x ratio by DOC towards 0.5 will increase the SCR performance of the whole exhaust gas aftertreatment system. At $\gamma > 0.5$ the » NO_2 SCR reaction« (R 7) becomes important. It is much slower than the standard SCR reaction and with $\alpha = \frac{4}{3}$, NH_3 is overconsumed. The NO_2 -SCR reaction occurs according to a mechanism wherein surface nitrates are first formed by NO_2 disproportionation, followed by their catalytic reduction to nitrogen by ammonia [54].



2.2.1 State-of-the-art Catalysts

Vanadium-, tungsten-, titanium-oxides (VWT) were the first catalysts used for NH_3 -SCR [55]. Drawbacks are the toxicity of vanadium, the high oxidation rate of SO_2 to SO_3 , hydrothermal instability and the limited temperature window (500 K to 700 K) of appropriate NO_x conversion performance as well as low storage capacity for NH_3 [53,56–58].

Although new catalyst-concepts, like vanadium and cerium on MnO_x - TiO_2 [59] or amorphous MnO_x catalysts [60,61] showed improved light-off at 400 K or even lower, VWT- and oxide-catalysts were not able to assert on the market for passenger car diesel engine aftertreatment. The second generation of SCR-catalysts focuses on metal-ion exchanged zeolites. Medium pore-size zeolites *e.g.* ZSM-5, Beta or Y could be proven as good candidates for catalytic application [53,62]. Primarily Cu-ZSM-5 [56] and Fe ZSM-5 [58,63–65] became famous (in following abbreviated as Cu-zeolite or Fe-zeolite). They show very good conversion in a broad temperature window and durability towards H_2O and SO_2 poisoning [63]. Among others Cavataio *et al.* [66] reported a better light-off behavior for the Cu-ZSM-5, while the Fe ZSM-5 has better NO_x conversion in high temperature regime. After ageing for 64 h at 670 °C (to represent roughly 120 k mi on a diesel vehicle with a regenerating soot filter), it was obvious that vanadium-based SCR was not an option [60], due to the dramatic decrease in NO_x conversion performance

(compare **Fig. 5**). Furthermore Cu-zeolites show higher NH_3 storage capacity compared to Fe-zeolites, which is beneficial for the De NO_x reaction [49]. Many preparation methods for Cu-zeolites are reported and compared in literature. Park *et al.* [62] found the optimal De NO_x performance for ion-exchange rates of 4 wt.-% Cu into the ZSM-5 zeolite. Consequently Cu or Fe exchanged into the Beta- or ZSM-5-zeolite framework have promising properties for application and are currently introduced into the market [4]. Metkar *et al.* even proved the combined Fe/Cu-zeolite catalysts to have higher NO_x conversion activity over broader temperature range compared to the individual Fe- or Cu-zeolite catalysts [52,67].

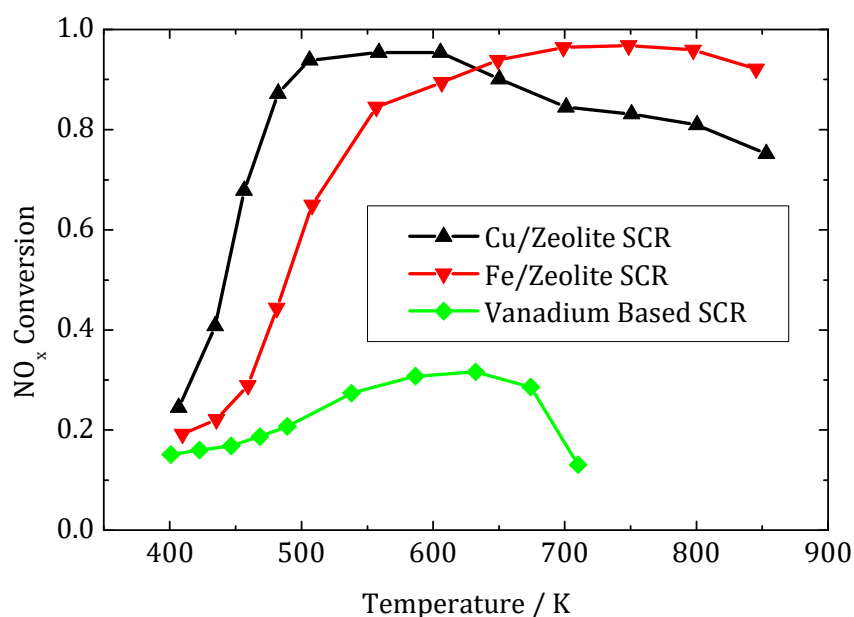


Fig. 5 NO_x conversion of Cu, Fe and Vanadium based SCR formulations as a function of temperature. 350 ppm NO , 350 ppm NH_3 , 14 % O_2 , 5 % H_2O , 5 % CO and N_2 balance at GHSV 30.000 h^{-1} . Original illustration, based on [60,66].

Next to the experimental studies, many theoretical work on the field of modelling were published over the last decade. Sjövall *et al.* [50,51,68–71] presented a detailed kinetic model description of the NH_3 -SCR over Cu-ZSM-5. Thereby, NH_3 adsorption seems to be the key for good catalytic properties. Three storage sites were distinguished: NH_3 adsorption at 1) the exchanged Cu-ions, 2) Brönsted acid sites from Si/Al zeolite framework and 3) weakly bound storage sites [50,51].

As shown by Nova *et al.* [72,73] another obstacle of NH_3 -SCR over Fe-zeolites as well as VWT catalysts is the inhibition of the Standard and Fast SCR reaction rate by excess NH_3 . They found a kinetic description for this phenomenon but it seems not to be significant for their analyzed copper zeolite catalyst [49]. For higher temperatures, different side

reactions are conceivable *e.g.* the oxidation of NH_3 by O_2 or NO_2 forming N_2 , NO or even N_2O . Nevertheless, especially for the Fe-zeolite a very high selectivity (up to 100 %) for the reduction of NO_x to N_2 and only negligible amounts of formed N_2O were observed [65].

The main drawback of Cu- and Fe-zeolites is their hydrothermal stability [53,57,65]. A decrease of NH_3 storage capacity is reported to be associated with a dramatic loss in NO_x conversion performance as well as a decreased selectivity towards N_2 formation. Appropriate NH_3 Temperature Programmed Desorption (TPD) experiments on hydrothermally aged Cu-Beta zeolites were performed by Wilken *et al.* [57]. The results are exemplarily depicted in **Fig. 6**. They observed the deactivation of acid sites for strongly bound NH_3 (shift of peak-maximum towards lower temperatures for the NH_3 released during temperature ramp up at times > 60 min). Also, the amount of weakly bound NH_3 (released during flushing, minute 35 to minute 60) is reduced, resulting in a decrease of the overall NH_3 storage capacity (inset). These negative phenomena could be attributed to the destruction of zeolite structure (decreased surface area and pore volume) and the agglomeration of active Cu phase [74,75].

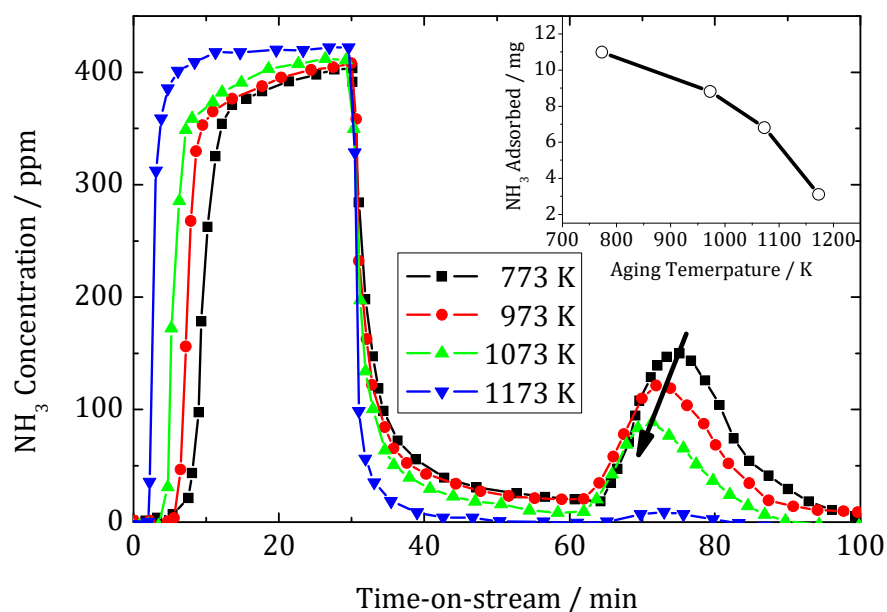


Fig. 6 NH_3 concentration as a function of the time-on-stream for Temperature Programmed Desorption (TPD) experiments on hydrothermally aged Cu-Beta zeolites (Ageing: 3h at 773 K, 973 K, 1073 K and 1173 K in 8 % O_2 , 5 % CO_2 and 5 % H_2O , Adsorption at 423 K, temperature ramp: 10 K min^{-1} up to 773 K. The inset shows the loss of NH_3 storage capacity with ongoing hydrothermal ageing. The illustration originates from [57].

2.2.2 Novel Catalysts

The key to overcome the stability issues towards hydrothermal ageing of Cu- or Fe-exchanged ZSM-5- or Beta-zeolites seems to be a change in the zeolite system. Very recently many studies on small pore size zeolites with the chabazite framework topology *e.g.* CU-SSZ-13 [76,77], CU-SAPO-34 [78–80] or Cu-CHA [52] were published. CU-SSZ-13 and CU-SAPO-34 show superior SCR performance, both before and after high-temperature hydrothermal treatment compared to medium pore size zeolites CU-ZSM-5. Even after hydrothermal ageing, a wide temperature operation window with nearly 100 % NO_x conversion between 450 K and 750 K has been reported [81].

Compared to Cu- or Fe-ZSM-5-zeolites, for which the NO_x reduction strongly depends on the NO₂-to-NO_x feed ratio (SCR performance optimal at 0.5), for Cu-CHA the enhancement in the NO_x reduction activity by NO₂ is not nearly as significant [52]. Furthermore a higher NH₃ storage capacity and better light-off at low temperatures of Cu-CHA compared to Fe-ZSM-5 is reported [52]. This features Cu-CHA for a broader range of operation conditions.

The Cu-SSZ-13 was proven to combine a preferable light-off performance ($T_{50} < 400$ K, even better as Cu-ZSM-5) with the high temperature DeNO_x performance of the Fe-ZSM-5 (compare **Fig. 5**) [76,77]. This wide temperature window for operation as well as high thermal stability supporting the CU-SSZ-13 as a potential candidate for future application. The thermal stability of CU-SSZ-13 against hydrothermal ageing was examined by Kwak *et al.* [76]. Exemplary results of their work are given in **Fig. 7**. As Cu-ZSM, Cu-Beta and Cu-Y show decreased NO_x conversion after hydrothermal ageing, the CU-SSZ-13 remains its high DeNO_x performance. The SCR of NO_x to N₂ over CU-SSZ-13 is characterized by very high selectivity (close to unity) and nearly no N₂O formation even after hydrothermal ageing, while Cu-ZSM-5 or Cu-Y show increased N₂O release after hydrothermal ageing [76,77,82].

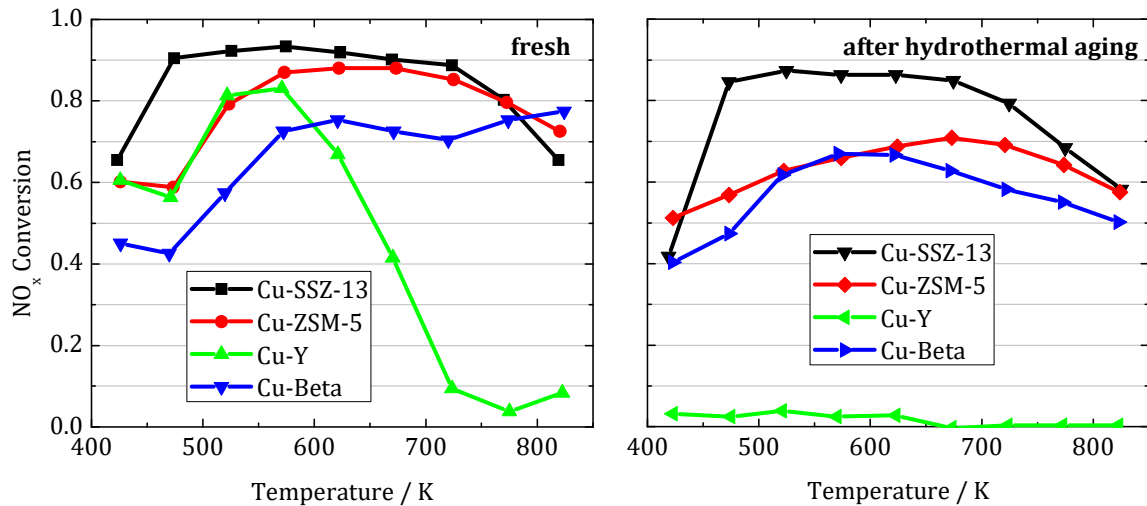


Fig. 7 NO_x conversion as a function of the temperature (feed: 175 ppm NO, 175 ppm NO₂, 350 ppm NH₃, 14 % O₂, 10 % H₂O in balance N₂) for different Cu-zeolites. Left: for fresh catalysts, right: after hydrothermal ageing (10 % H₂O in air at 1073 K for 16 h). Original Illustration based on [76].

2.3 Diesel Particulate Filters

To reduce the particulate matter, originating from the combustion process of a diesel engine, the state of the art technology is the so called diesel particulate filter (DPF) [3]. The honeycomb monolithic structures consist of parallel channels, whereas inlet and outlet channels are alternatively plugged (compare **Fig. 8**). This structure forces the gas flow to go through to porous filter wall. During gas transport, particles stick to the porous wall, causing soot filtration. Appropriate filters are named »wall flow filters«.

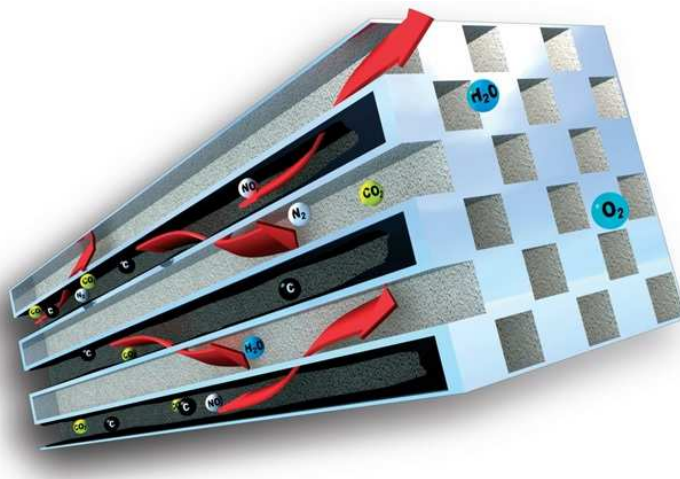


Fig. 8 Honeycomb wall flow diesel particulate filter. The arrows indicate the gas flux through the porous channel walls. The illustration originates from [83].

Nevertheless, an increasing mass of filtered soot leads to elevated backpressure, which has to be avoided due to higher fuel consumption and a decreasing engine efficiency [84].

Hence soot removal is necessary in regular intervals. A controlled rise in the exhaust gas temperature up to 873 K [85,86] together with the oxygen excess in diesel exhaust gas results in burn off the flammable soot components (called »active regeneration«). The combustion of the total accumulated soot amount (up to 10 g l^{-1} , gram per liter filter volume) within the filter causes extreme temperature conditions till 1300 K, putting high requirements on the thermal stability of the filter material [87]. To avoid this scenario, several approaches are discussed in literature. One way is to reduce the light off temperature by promoting an oxidation catalyst e.g. CeO_2 on the filter [4,88,89], reducing the soot combustion temperature by more than 150 K. Another option is the oxidation of the soot particles (carbon) by means of the radical NO_2 as reducing agent [90]. Thus, an oxidation catalyst like Pt is utilized in the filter, continuously oxidizing NO to NO_2 [91]. As shown in **Fig. 9**, NO_2 assisted soot oxidation runs at significantly lower temperature ($> 500 \text{ K}$) compared to O_2 assisted combustion of soot ($> 700 \text{ K}$). Hence a continuous regeneration (»passive regeneration« or continuous regeneration trap (CRT)) by NO_2 could be achieved. Furthermore modelling of the particulate filter helps to adopt the regeneration strategy for car application [92]. Next to soot particles, also lubricant derived ash components continuously plug the DPF. As they are not removable by means of oxidation, they remain in the filter, reducing its lifetime [93].

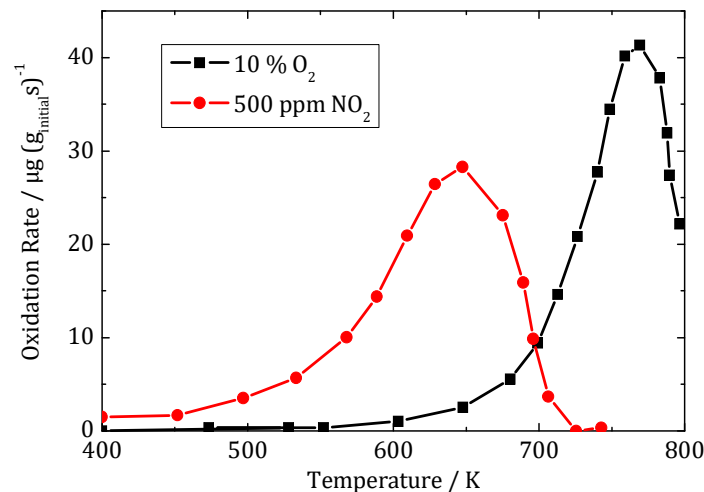


Fig. 9 Soot-oxidation rate as a function of the temperature for Printex®U model soot oxidized with O_2 (black curve) and NO_2 (red curve). Original illustration based on [90].

2.3.1 Soot Particles

2.3.1.1 Origin of the Soot Particles

The nucleation of soot primary particles is considered as the least well understood step in the soot formation process [94]. Many soot precursors are discussed in literature [95], *e.g.* acetylene, polyacetylene, benzene and polycyclic aromatic hydrocarbons (PAH). Nevertheless, the fundamental process for the formation of soot particles is the formation of PAHs inside the combustion chamber [96,97]. They arise from fuel constituents via several reaction pathways [5] *e.g.* from acetylene. By collision with other PAHs or by agglomeration of further HCs, a PAH grows to a so called »soot-nucleus«. These soot-nuclei agglomerate to spherical particles, called »primary particles«. For typical diesel soot, their diameter ranges from 5 nm to 20 nm [98]. The primary particles further agglomerate, resulting in fractal structures consisting of soot chains or clusters that are typically 50 to 150 nm in diameter (»soot particle«). A measure for the shape of the soot particles is the fractal dimension [99]. It describes the deviation of the soot particles shape to a perfect spherical particle. In the combustion chamber a temperature-window of $1600\text{ K} < T < 1900\text{ K}$ at HCs excess ($\lambda < 0.5$) is mentioned to be promoting for the soot-formation [5].

The inhomogeneous mixture within the cylinder of direct injection engines *e.g.* diesel is a promotion factor for the formation of large particulates. Nevertheless, during gasoline combustion, particles are also emerging. Harris *et al.* [100] compared the particle size distribution between different combustion engine technologies. In **Fig. 10** two exemplary distributions are shown. While the promoting effects in a diesel engine lead to mean particle sizes between 60 nm and 120 nm (for the engine soot under their study) having a symmetric size distribution on logarithmic scale. This variety is due to different engine operation conditions *e.g.* EGR rate. Particles arising within a gasoline engine are significantly smaller with the majority emitted at 10 nm to 25 nm size. The mean particle size based on mass is in the range of 40 nm to 80 nm.

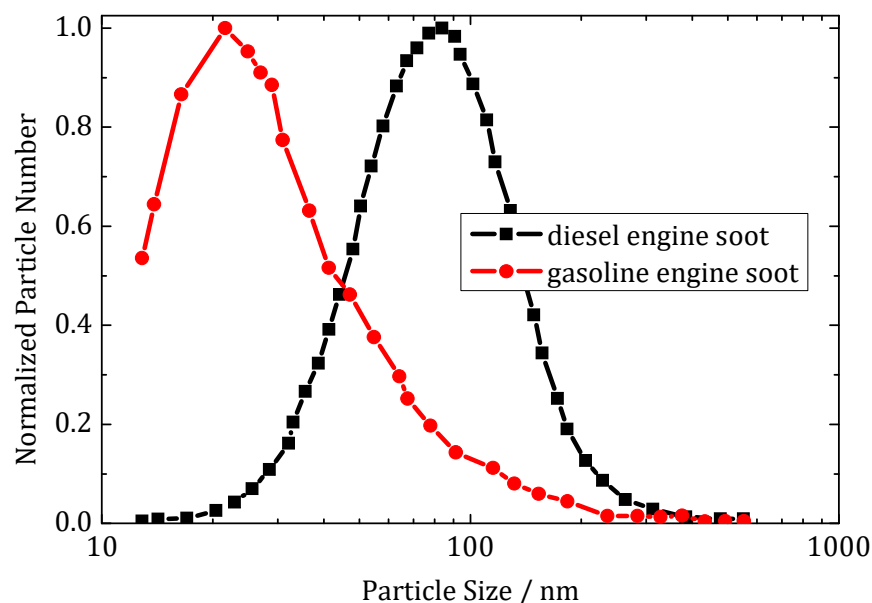


Fig. 10 Normalized particle number as a function of particle size. The data originates from [100]. The particle size distribution of a typical diesel engine soot is compared to a typical gasoline engine soot.

2.3.1.2 Model Soot and Engine Soot

Main characteristics of a bunch of soot particles are the particle size distribution, specified by the mean particle size, and the chemical composition. Latter is analyzed in terms of the share between EC (elemental carbon) and OC (organic carbon). Soot particles consist of a core of graphitic or graphene like structures [101] with some organic constituents attached to the primary particulates surface. The chemical composition is known to determine the oxidation behavior [90]. Earlier soot oxidation was found for higher OC rate. Engine soot changes in composition and size by means of the engine operation mode, fuel composition or engine milage [96,102]. Consequently its oxidation behavior is not constant, *e.g.* idle soot is more reactive than full load soot [90]. Also, lubricant derived components could attach to the soot particles, changing their chemical composition depending on engine operation point.

To overcome the stability issues of engine soot, several kinds of model soot are suggested in literature [96,103,104]. Spark discharge soot (GfG) [105] and Printex®U (graphite powder) represent the higher and lower reactivity limits toward oxidation. Engine soot was found to be in between [106]. A further possibility to produce highly stable model soot is a commercial soot-generator utilizing propane or liquid fuels as source for soot particles [104]. Quenching the diffusion flame by N₂ leads to zones of HC excess, promoting soot particle generation. The controllable quenching and gas flow allow a wide

range of parameters being adjusted, producing stable model soot in terms of mean particle sizes between 26 μm and 340 μm as well as EC contents between 20 and 99 % (rest is OC) [104,107]. For diesel engine out soot a EC rate between 60% and 80 % [96,108] is reported. Nevertheless, experimental results were more reproducible for the oxidation of the model flame soot than for the oxidation of diesel soot, and the flame soot was recommended as good model for diesel soot in oxidation studies [103,109]. Nowadays the application of a DOC upstream the particulate filter in the exhaust branch is standard. As the DOC converts most of the HCs attached to the soot particles, the soot collected within the DPF shows a high ratio of EC (> 90 %), which is the same for model soot from a propane burner [109].

2.3.2 Material Properties and Pressure-Drop

The channel wall thickness of typical monolithic wall flow DPFs ranges from 300 μm to 400 μm [3] with cell densities between 90 cpsi and 300 cpsi. The porous walls consist of silicon carbide or cordierite, utilizing porosities between 45.1 % and 49.1 % at median pore sizes of 11.8 μm to 26.6 μm [110] (example shown in **Fig. 11 c**)). Also other ceramic filters *e.g.* sintered powders, fibers or open celled foams consisting of aluminum titanate or silicon nitride were considered as potential diesel particulate filters [111]. Another class are the metal supported flow-through particulate traps [112]. Nevertheless, their properties in terms of filtration efficiency, thermal stability, durability *etc.* are far behind those from wall flow monoliths made of silicon carbide or cordierite. This explains why they have only negligible market share but are still used in some niche applications.

The basic principle of any kind of diesel filter is the separation of the soot particles, carried by the gas flow, on a collective surface. The separation involves passing the gas stream through a porous barrier, which retains the particles. Depending on the type of this barrier in principle two filter mechanisms could be distinguished (compare **Fig. 11 a**) and **b**)). In case the mean diameter of the collected particles is smaller compared to the mean pore size of the filter media, the collection mode is called deep bed filtration. In case of particles, smaller than the mean pores of filter media, the filtration is referred to as surface filtration or »cake filtration« [92]. Ceramic wall flow monoliths used as diesel particulate filters work with a combination of both filter mechanisms. If the filter is clean, on first stage of loading soot particles are collected by means of depth filtration inside the porous wall. As the depth filtration capacity is saturated, the surface pores close to the inlet

channel are plugged [113,114]. A cake layer consisting of filtered soot particles forms within the inlet channel. In ongoing soot loading the particles in the cake layer itself act as elemental collectors. Particles with small diameter are collected within the soot layer by means of deep bed filtration, large particles are filtered on the cake layer surface. Typically the cake layer thickness within the inlet channel reaches 30 to 60 μm until a regeneration is required due to elevated backpressure.

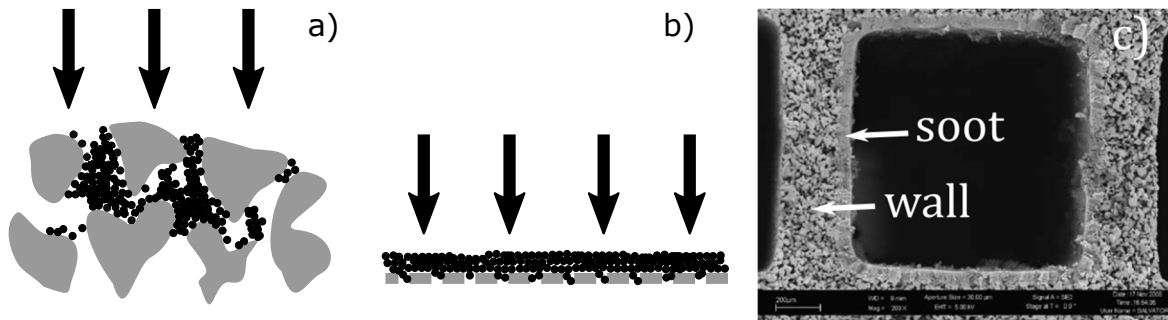


Fig. 11 Schematic representation of the filter mechanisms inside a particulate filter: a) depth filtration within the porous wall and b) cake filtration as distinct layer in the inlet channel. In c), a SEM picture of a channel cross section of a soot loaded DPF, presented by Bensaid *et al.* [113], is given.

For the depth filtration three main processes of aerosol deposition could be distinguished (see **Fig. 12**) [115,116]. A massive particle approaching the filter structure will not exactly follow the air stream lines around the obstacle. Due to its inertia, it follows a straighter path, ending up on the filter media. The higher the particle mass, the greater will be the deviation of the velocity vector compared to the gas flow direction. This process is called »inertial impaction«. Small particles (negligible inertia) follow the stream lines even at high gas velocities around the obstacles. If the distance between the streamline and the obstacle surface is smaller than the particle radius, it will stick to the filter media. This is called »interception«. The smallest particles in the gas stream collide with the gas molecules. This changes their direction of motion, compared to the gas stream lines, following random paths. This kind of motion in close proximity to a filter medium leads to a contact. A concentration gradient between the bulk of the flow and the flow near the obstacle establishes, increasing the »Brownian motion« towards the obstacle. The smaller the particles, the more efficient is this kind of filtration. Quantitatively it could be described by means of the Peclet number [92].

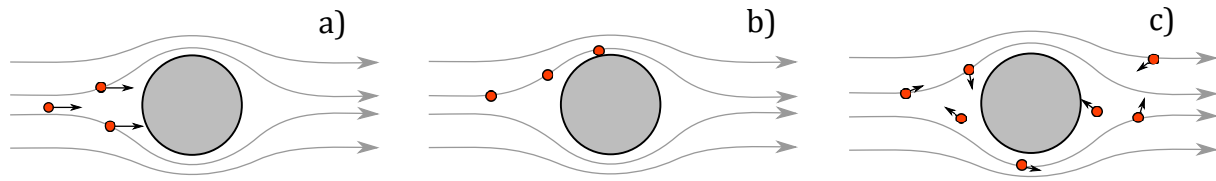


Fig. 12 Schematic representation of the three aerosol deposition modes occurring during depth filtration: a) Inertial Impaction, b) Interception and c) Brownian motion. The illustration is based on [115].

Combining both major filter mechanisms, deep bed filtration and surface filtration, as well as the buildup of the soot cake layer in progression of the soot loading, itself acting as an efficient filter for particulate removal, the diesel particulate filters nowadays are very efficient. Many reports on filtration efficiency are presented in literature [117–119]. Studying 40 different DPFs (differing in porosity, mean pore width *etc.*), in [117] the total particle number filtration efficiencies of >98 % over a particle size range of 20–300 nm are reported. As engine soot always shows a distinct particle size distribution (compare **Fig. 10**), the filtration efficiency for each separate particle size is hard to distinguish. Yang *et al.* [98] reported on evaluation of single particle size filtration efficiencies using dry ammonia sulfate particles with size varying from 30 to 615 nm. Filter under study was a SiC filter (NGK Insulators Ltd.) with 42 % porosity, wall thickness of 360 μm and volumetric mean pore width of 9 μm . As shown in **Fig. 13**, during the initial stage of filter loading (deep bed filtration) they observed best filtration (close to 100 %) for the largest particles with 455 and 615 nm. Also, the smallest particles between 30 and 40 nm revealed very good filtration performance > 90 %. Particles larger than 80 nm and smaller than 200 nm initially were filtered worse with efficiencies below 70 %. Nevertheless, after 8 min under their experimental condition of loading (unfortunately mass flow not mentioned) the filtration mode changed from deep bed filtration to cake filtration, revealing filtration efficiencies for all particle sizes under study close to 100 % for the rest of the loading time. The particulate penetration depth inside the porous filter wall (in distance to the inlet channel) was determined to be about 80 μm .

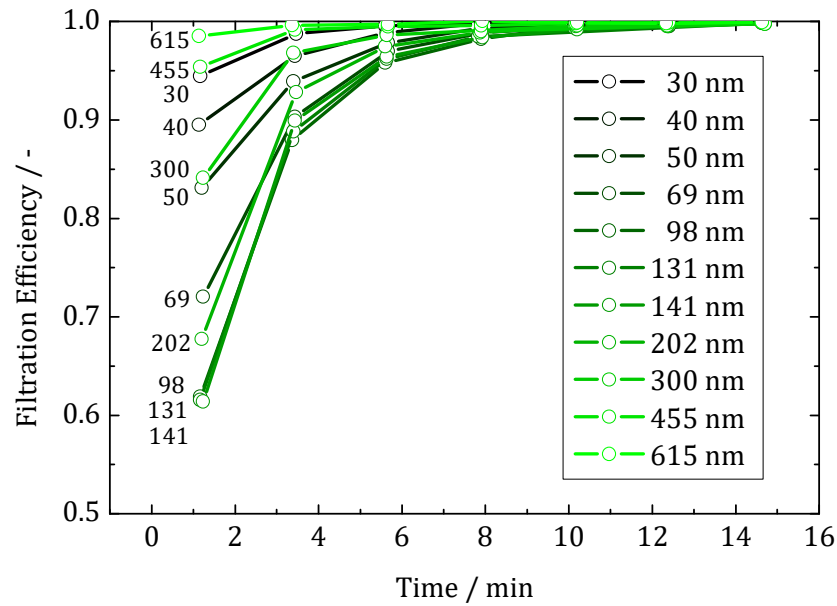


Fig. 13 DPF filtration efficiency as a function of loading time for different particle sizes (laboratory generated dry ammonia sulfate particles). Data originates from [98] (for further experimental details, the reader is advised to this article).

Next to the filtration efficiency also the backpressure of the DPF depends on the filtration mode [98,120–122]. In **Fig. 14** (left) the backpressure as a function of loaded soot mass is depicted. At initial stage (indicated with 1) of the loading process, the clean DPF reveals a certain backpressure as it is a flow barrier for the gas stream. Typical values are in the range of 0.5 to 2 kPa. Calculatory analysis on the dependencies of the filter backpressure from material parameters *e.g.* porosity, narrowness of the pore size distribution as well as median pore width were carried out, among others, by Merkel *et al.* [121]. They found a higher porosity (> 50 %) and a narrow particle size distribution around 12 μm to result in low filter backpressure. Nevertheless, if the porosity is too high, the material stability could not be guaranteed. At stage 2 (**Fig. 14** left) of the deep bed filtration, the walls of the porous filter material close to the inlet channel are covered with soot. This results in increasing backpressure with increasing soot mass. At stage 3, soot is plugging the necks of the surface pores, characterized by a steep slope of the backpressure curve. When all the surface pores are blocked, the deep bed filtration is saturated and filtration mode changes to surface filtration establishing a cake layer on top of the porous wall inside the inlet channel. This fourth stage of loading is featured by a less steep linear growth of the filter backpressure. Typical values for the deep bed filtered soot amount ranges from 0.2 to 1 g l^{-1} (compare **Fig. 14** right). The deep bed filtration process on DPF was already studied in detail. Sanui *et al.* [114] reported on a soot penetration depth of 40 μm based

on SEM measurements on DPF (porosity 50 %, mean pore size 15 μm). Soot distribution studies by means of VP-SEM (variable Pressure-SEM) and UV (ultraviolet) microscope technique done by Yapaulo *et al.* [123] revealed the bulk of the particles to be deposited close to surface with penetration depths up to 100 μm . Nevertheless, as the filtration efficiency is less than 100 % during deep bed filtration (compare **Fig. 13**), a small amount of particles slipped through the porous wall, penetrating deeper zones. Furthermore, they investigated the influence of filtration velocity (4 m s^{-1} and 8 m s^{-1}). A higher filtration velocity results in higher soot mass loaded within the porous wall, whereas the penetration depths remain nearly the same.

The main contribution of the filter backpressure is based on deep bed filtered soot within the porous wall. That is why, among others, Koltsakis *et al.* [120] suggested a special layered DPF design, based on a theoretical filter model calculation. The implementation of a thin »stop layer« in the inlet channel on top of the porous wall with mean pore width of 4 μm and a porosity of 50 % will decrease the mass of deep bed filtered soot from 1 g l^{-1} to 0.3 g l^{-1} . Associated with the faster overcome of the deep bed filtration in wall, the filtration efficiency will be maximized and the backpressure could be significantly reduced. The resulting backpressure as a function of the soot loading is given in **Fig. 14** (right).

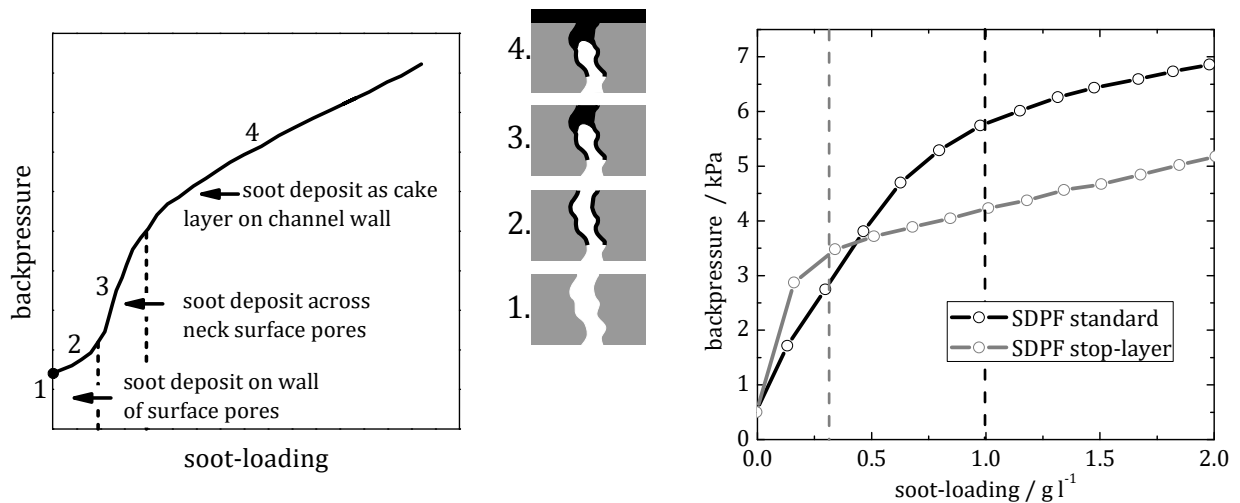


Fig. 14 Left: Filter backpressure as a function of the soot loading. The domains characterized by numbers (1...4) explain the conceptual model of DPF filling depicted in the middle [121]. Right: Filter backpressure as a function of the soot loading for an SDPF without and with a further stop-layer inside the filter channel towards the porous wall (55 % porosity and mean pore width of 14 μm). Further details and original illustration is given in [120]. The dashes lines indicate the transition from depth filtration to cake layer filtration.

Much effort has been done on the field of modelling and calculating the filter backpressure evolving during soot loading [124–127]. Haralampous *et al.* [125] presented a detailed description of the individual backpressure contributions. The contraction of the gas at the inlet channels (eq. (2.3)), the soot deposited as cake layer in the inlet channels (eq. (2.4)), the porous filter wall (eq. (2.5)), the channels themselves (eq. (2.6)) and the gas expansion at the outlet channels (eq. (2.7)) represent individual flow resistances, increasing the overall filter backpressure, as given in eq. (2.2). The channel cross section as calculatory domain, the above equations refer to as, is schematically illustrated in **Fig. 15** (left).

$$p_1 - p_2 = \Delta p_{\text{Contraction}} + \Delta p_{\text{Soot}} + \Delta p_{\text{Wall}} + \Delta p_{\text{Channel}} + \Delta p_{\text{Expansion}} \quad (2.2)$$

$$\Delta p_{\text{contraction}} = \left[1.1 - 0.4 \frac{(D - 2w)^2}{2(D + w_w)^2} \right] \frac{RT\dot{m}^2}{2p_1 M_g N^2 (D - 2w)^4} \quad (2.3)$$

$$\Delta p_{\text{soot}} = \frac{RT}{M_g \bar{p}} \left[\frac{\mu D \dot{m}}{2k_{pl} A_f} \right] \ln \left(\frac{D}{D - 2w} \right) + \frac{\beta D w \dot{m}^2}{A_f^2 (D - 2w)} \quad (2.4)$$

$$\Delta p_{\text{wall}} = \frac{\mu v_w}{k_{w0}} \cdot w_s = \frac{RT}{M_g p_2} \left(\frac{\mu w_w \dot{m}}{k_{w0} A_s} \right) \quad (2.5)$$

$$\Delta p_{\text{channel}} = \frac{a_1 \mu R T L \dot{m}^2}{3 M_g N} \left[\frac{1}{p_2 D^4} - \frac{1}{p_1 (D - 2w)^4} \right] \quad (2.6)$$

$$\Delta p_{\text{expansion}} = \left[1 - \frac{D^2}{2(D + w_w)^2} \right] \frac{RT\dot{m}^2}{2p_2 M_g N^2 D^4} \quad (2.7)$$

Equation (2.5) represents the well-known »Darcy's Law« for description of the flow resistance of a permeable medium [92], involving the mediums permeability k . Darcy suggested this description of the pressure drop in 1856, studying the water flow-through packed beds of sand.

For calculation of the permeability k several approaches are discussed in literature, among others, by Pulkrabek *et al.* [128] or Konstandopoulos *et al.* [129]. Latter suggested the following set of equations (eq. (2.8) to eq. (2.12)) for calculation of the soot layer permeability k_{pl} . Nevertheless, as given here, it could also be applied on the porous filter wall to determine its permeability k_{w0} .

$$k_{w0} = f(\epsilon_{w0}) d_{c,w0}^2 \text{SCF}_{w0} \quad (2.8)$$

$$f(\epsilon_{w0}) = \frac{\frac{2}{9} \left(2 - \frac{9}{5} (1 - \epsilon_{w0})^{1/3} - \epsilon_{w0} - \frac{1}{5} (1 - \epsilon_{w0})^2 \right)}{1 - \epsilon_{w0}} \quad (2.9)$$

$$d_{p,w0} = \frac{2}{3} \frac{\epsilon_{w0}}{1 - \epsilon_{w0}} d_{c,w0} \quad (2.10)$$

$$SCF_{w0} = 1 + Kn_{w0} \left(1.257 + 0.4e^{-\frac{1.1}{Kn_{w0}}} \right) \quad (2.11)$$

$$Kn_{w0} = \frac{2 \lambda}{d_{p,w0}} \quad (2.12)$$

$$\lambda = v \sqrt{\frac{\pi MW_j}{2 R T}} \quad (2.13)$$

Depending on filter wall porosity ϵ_{w0} and mean pore width $d_{p,w0}$, the wall permeability k_{w0} could be calculated. The calculation involves the Kuwabara function $f(\epsilon_{w0})$, the Knudsen number Kn_{w0} , the mean free path λ as well as the Stokes-Cunningham factor SCF_{w0} . Details are given in [93].

k_{w0} ranges from $1.8 \cdot 10^{-13} \text{ m}^2$ to $1.2 \cdot 10^{-12} \text{ m}^2$ [124,125]. The same result was found by Wirojsakunchai *et al.* evaluating the permeability of different filter substrates. They report on values of $k_{w0} = 1.10 \cdot 10^{-13} \text{ m}^2$ to $3.96 \cdot 10^{-13} \text{ m}^2$ for porosities between 45.1 % and 49.1 % and median pore sizes ranging from 11.8 μm to 26.6 μm [110].

Replacing $d_{p,w0}$ by the diameter of the aggregated soot particle ($d_{\text{aggregate}}$) in eq. (2.10) and (2.12) as well as replacing $d_{c,w0}$ by the primary particles diameter (d_{primary}) in eq. (2.8) and (2.10), values for the soot layer permeability k_{pl} could be calculated. Depending on the soot layer porosity ϵ_{pl} , values of k_{pl} between 10^{-14} m^2 and 10^{-13} m^2 are reported [129]. The soot layer features soot densities ρ_{pl} between 70 kg m^{-3} [130] and 120 kg m^{-3} [93]. Comparing with graphite (density of 2300 kg m^{-3}), its porosity could be determined to be in the range of $90 \% < \epsilon_{pl} < 100 \%$.

Nevertheless, the backpressure description by Haralampous *et al.* [125] (as given above) does not take the soot mass deposited within the porous filter wall and its evolution during loading time into account. Serrano *et al.* [126] and Konstandopoulos *et al.* [129] presented a »Unit Collector Cell« model. The wall is assumed to be a dense packaging of collector cells (illustrated in **Fig. 15** left). These spheres consist of a spherical unit

collector (consisting of solid wall material with radius d_{c0}), which is surrounded by void, so that the experimentally determined wall porosity ϵ_{w0} and mean pore width $d_{p,w0}$ are represented. This configuration with radius $d_{cell,w}$ is called collector cell, schematically presented in **Fig. 16 a**). When soot is trapped inside the wall during loading, it distributes around the collector unit, resulting in its increased diameter $d_{c,w}$, which is given by eq. (2.14). Soot particles themselves are not spherical, having a certain fractal dimension [99]. To account for irregular deposition of aggregated particles around the unit collector in the wall, the shape factor χ (ranging from 0 to 1, higher values indicate more spherical particle arrangement) was multiplied with the density of the soot in the porous substrate $\rho_{s,w}$. A schematic is given in **Fig. 16 b**) and c). Consequently, the decreased porosity of the soot loaded wall has to be calculated with eq. (2.15). As there is less void available for the gas flow, the permeability k_w of the soot loaded porous wall decreases with increasing amount of wall-soot (eq. (2.16)), which leads to an elevated backpressure. When the saturation coefficient ϕ approaches to 1, the collector unit is saturated with soot (eq. (2.18)) and the filter mechanism will change to cake filtration. Thereby, the percolation factor ψ defines the onset of pore bridging [126]. As there may be parts of the wall, filled up with soot and other parts, which are soot free, the overall permeability $k_{w,e}$ of the soot loaded wall is calculated by means of eq. (2.19). Using Darcy's law (eq. (2.5)) the backpressure contribution of the soot loaded wall could be evaluated.

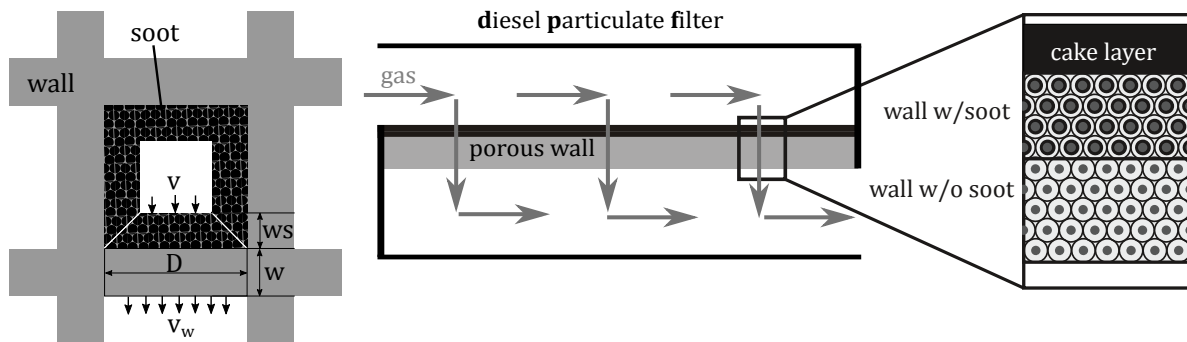


Fig. 15 Left: Schematic representation of a cross section of a filter wall channel (grey area). The black area indicates the soot deposited as cake layer inside the channel. Right: Schematic representation of a pair of inlet/outlet channels. The arrows indicate the gas flow-through the porous wall. On the right a zoom of the soot loaded wall is depicted, representing the arrangement of the unit collectors as representation of the porous filter wall.

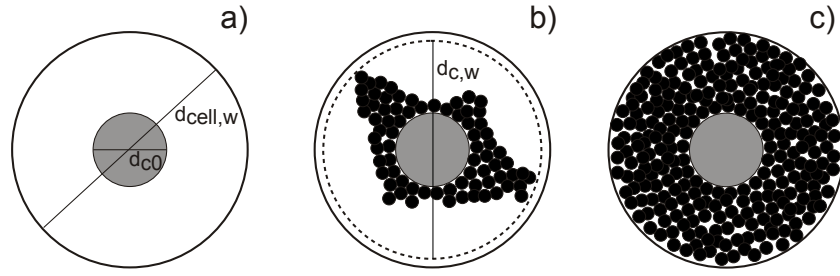


Fig. 16 Different states of the collector unit cell during soot loading process: a) represents the initial state of a clean collector unit, b) describes the case of irregular growth around the collector unit with low soot mass, leading to low shape factor and c) saturated cell with high shape factor. The schematic is based on Serrano *et al.* [126].

$$d_{c,w} = 2 \left(\frac{d_{c,w0}^3}{8} + \frac{3m_{s,cell}}{4\pi\chi\rho_{s,w}} \right)^{1/3} \quad (2.14)$$

$$\epsilon_w = 1 - \frac{d_{c,w}^3}{d_{cell,w}^3} \quad (2.15)$$

$$k_w = f(\epsilon_w) d_{c,w}^2 SCF_w \quad (2.16)$$

$$\phi = \frac{d_{c,w}^3 - d_{c,w0}^3}{(\psi d_{cell,w})^3 - d_{c,w0}^3} \quad (2.17)$$

$$m_{s,sat,cell} = \frac{3}{4} \pi \left(\left(\frac{\psi d_{cell,w}}{2} \right)^3 - \left(\frac{d_{c,w0}}{2} \right)^3 \right) \rho_{s,w} \quad (2.18)$$

$$k_{w,e} = \left(\frac{1}{k_{w0}} + \frac{1}{k_w} \right)^{-1} \quad (2.19)$$

Due to the shape factor, the soot density within the porous filter wall $\rho_{s,w}$ is reported to be smaller than the soot density in the cake layer ρ_{pl} . Values between 8 kg m^{-3} and 14 kg m^{-3} were determined in [124] by means of calculation. Furthermore a filtration model, based on the unit collector cell model was presented by Konstantopoulos *et al.* [124]. For Brownian motion as well as for interception, collector filter efficiencies are calculated, resulting in deposition of incoming particulates within the collector units. The increased diameter leads to increased filter efficiency for the next iteration time step. Inertial impaction was found to have no influence on the trapping of soot particulates [114].

2.4 SCR-coated Diesel Particulate Filter

The increasing efficiency of diesel engines leads to a decrease of the exhaust-gas temperature and thus to more stringent requirements for the thermal design of the exhaust-gas branch. A combination of an NH_3 -SCR active catalyst (nowadays Cu-zeolite) with a DPF utilizes the DeNO_x functionality together with PM abatement within one aftertreatment component. Next to an improved size and weight (compared to separate SCR-catalyst and DPF), the main advantage of the SDPF is the better thermal management, as it could be placed closer to the engine [131]. The washcoat is coated within the porous walls of a high porosity (> 50 %) DPF substrate [121], decreasing its porosity. This results in slightly increased backpressure compared to DPF without coating. Nevertheless, finding the right porosity and washcoat amount is always a compromise between mechanical stability, backpressure and achieved catalytic performance [120]. For the catalytically active component within the washcoat mostly a zeolite (Cu or Fe) is chosen, as the VWT catalysts have a worse resistance against the thermal stress during regular regeneration [131].

The drawback of such an integrated system is the overlap of functionalities. The interaction of soot particles and the catalyst for ammonia-based SCR of NO_x is still controversially discussed in literature [132–134]. For instance, Schrade *et al.* [135] and Mihai *et al.* [136] observed only a slight decrease of the NO_x conversion (up to 5 %) for the standard-SCR reaction in presence of engine soot in the SDPF (loaded on engine test-bench). They explained this phenomenon by blocking of the active catalytic sites [135,136]. Cavataio *et al.* [137] also reported on a loss in NO_x conversion (see **Fig. 17** right) for standard- and fast-SCR of soot loaded SDPF, but on much larger extent (up to 20 %, using model-soot from soot-generator). They also explained the behavior by the blocking of active sites. Unfortunately, the amount of deep bed filtered soot (or a backpressure curve) is not given in [66,135,136]. Using a physical mixture of powdered SDPF and the commercial Printex®U soot, a similar situation (high loss in NO_x conversion) was found from Tronconi *et al.* [138,139]. They presented comprehensive studies on the interaction between soot and the SCR DeNO_x catalyst. The focus of their work was the role of NO₂ within the SDPF reaction network in terms of the competing NO₂-soot combustion vs. Fast- and NO₂-SCR reaction. Thereby, at temperatures above 523 K NO₂ is reduced by the oxidation of soot. This leads for fast-SCR to decreased NO_x conversion as it shifted towards the slower standard SCR stoichiometry $n(\text{NO}_2)/n(\text{NO}_x) < 0.5$. On the other hand

in the presence of soot, the NO_2 reduction by soot oxidation for the NO_2 -SCR results in higher conversions, as the $n(\text{NO}_2)/n(\text{NO}_x)$ ratio is shifted towards 0.5, promoting the fast-SCR reaction [135,138,139]. The results found by Schrade *et al.* for light-off experiments are given in **Fig. 17** (left). Also the *vice versa* effect of a reduced passive soot oxidation (by NO_2) when the fast SCR reaction is active, has been reported [140]. Nevertheless, in order to not deal with the cross reaction of NO_2 in the reaction gas to soot, only standard SCR reaction was considered here to evaluate the physico-chemical influence of soot on the DeNO_x behavior.

Next to the soot-influence on the DeNO_x properties, there are controversial results reported regarding the influence of soot on the NH_3 storage capacity of SDPFs. While a decrease in the NH_3 storage capacity was found upon soot loading [132,141], also elevated amount of stored NH_3 were reported. Schrade *et al.* [135] found 0.1 g l^{-1} to 0.2 g l^{-1} more NH_3 storage in the presence of soot, Mihai *et al.* [142] found an increase of $69 \mu \text{ mol}_{\text{NH}_3}$ and Tronconi *et al.* [138] reported $28 \mu \text{ mol}_{\text{NH}_3} \text{ g}_{\text{cat}}^{-1}$ more NH_3 storage, if soot is present. An increased ammonia storage capacity was explained by additional acid sites for NH_3 adsorption provided by the soot itself [143].

Despite the studies and results referred to above, there is still a lack of understanding of the microscopic processes governing the interaction of soot with the catalytic component in SPDFs.

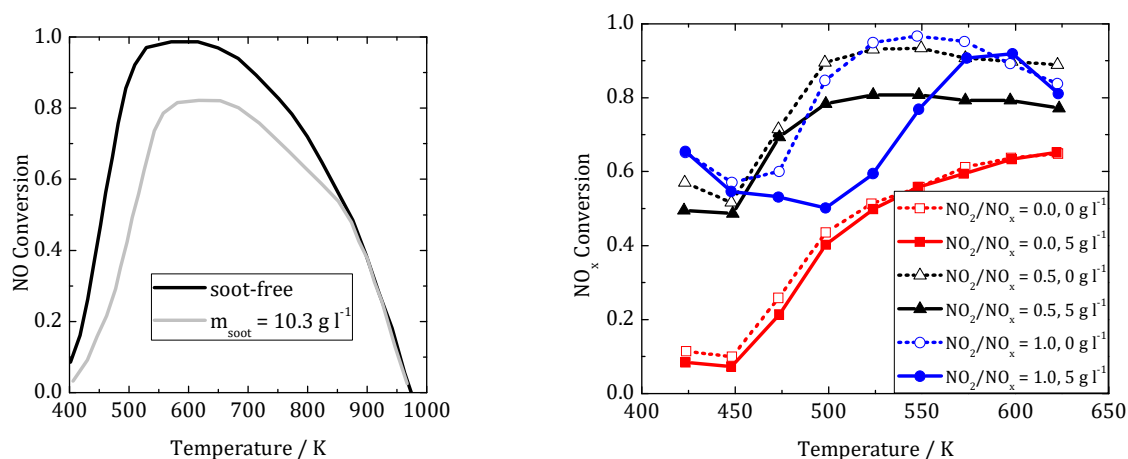


Fig. 17 Left: NO conversion as a function of temperature during standard SCR reaction (350 ppm NH_3 and 350 ppm NO dosed with 5 vol.-% H_2O and 14 vol.-% O_2 in N_2 during temperature was linearly ramped at 5 K min^{-1} from 400 K to 973 K) performed on SDPF samples with Cu-zeolite washcoat (soot free sample and soot loaded sample $m_{\text{soot}} = 10.3 \text{ g l}^{-1}$). The illustration originates from [66]. Right: NO_x conversion as a function of temperature for different NO_2 -to- NO_x ratios (0.0, 0.5 and 1.0) as well as for different soot loadings (0 g l^{-1} and 5 g l^{-1}). Experimental conditions and original illustration given in [135].

2.5 Gas Diffusion through Soot

Only few reports take a mass transport limitations inside the porous wall of soot loaded filters [144,145] into consideration, although the necessity for the gas species to diffuse through the soot layer deposited on top of the washcoat is evident. According to Park *et al.* [145], the soot inside the wall has much more impact on the SCR reactions compared to the soot as cake layer in the inlet filter channel. They extended the concept of the Thiele modulus (normally used for description of diffusion inside the catalyst washcoat) on the soot layer inside the porous wall. Hence, an effectiveness factor was introduced, reducing the reaction rates in the presence of soot in the porous filter wall. As soot particles (primary particle size 5 to 20 nm) deposit as a porous medium (porosity ϵ_{pl} , tortuosity τ_k and pore width d_p) with very small length scale, Knudsen diffusion was suggested as the relevant transport mechanism for the gas molecules through a soot layer [109,144,145]. The Knudsen diffusion for gas species k through a porous medium is calculated by means of equation (2.20):

$$D_k = \frac{\epsilon_{pl} d_p}{\tau_k} \frac{1}{3} \sqrt{\frac{8 R T}{\pi MW_k}} \quad (2.20)$$

MW_k represents the molecular weight of the gas molecules.

Nevertheless, regarding the gas diffusivity through a soot deposit, there is still a lack of understanding. To the best of our knowledge, a measurement of the self-diffusion coefficient of probe gas molecules within soot has not been reported yet in literature.

3 Experimental Section

3.1 Materials

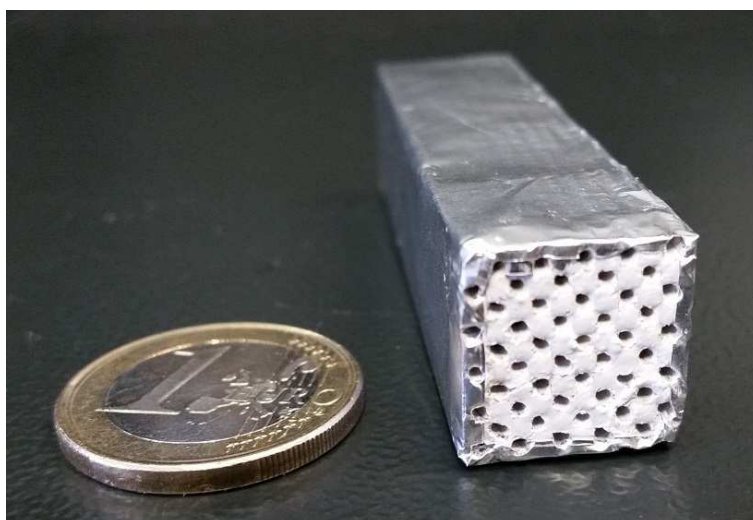
3.1.1 Preparation

The samples under study were two SDPFs, one SCR-catalyst (flow-through) and one NSC (flow-through). All are commercial products, supplied by the industrial partner (IAV GmbH). The SDPFs, consisting of a porous SiC wallflow filter with a Cu-containing zeolite washcoat as NH_3 -SCR active component. The specifications are given in **Tab. 3.1**. To prepare the SDPF samples studied here, the full-size SDPF monolith was cut. The channels of the cut SDPF pieces were alternatingly plugged to restore the particulate filter layout (preparation conforms [66]). An example of a prepared sample is given in **Fig. 18**. The plugging was done by dipping the sample headfirst in an $\alpha\text{-Al}_2\text{O}_3$ suspension (10 μm powder, 99.5 %, Sigma-Aldrich®, 1 g Al_2O_3 on 1 ml water), followed by stitching out the Al_2O_3 plug from every second channel. Finally, the sample was dried in an oven at 393 K for 1 h in ambient air. In prior tests, Al_2O_3 was proven to have no influence on any catalytic properties [4]. To avoid spatial distribution of soot in the axial channel direction, a short sample length was chosen: 60 mm for SDPF1 and 81 mm for SDPF2. The sample cross-section was 10 times 10 channels at a cell density of 350 cpsi or 286 cpsi, respectively. By means of mercury intrusion porosimetry, the porosity of the filter wall of SDPF1 was determined to be 48.0 % and its mean pore width to be 26.6 μm . Unless otherwise stated, investigations performed on SDPF samples refer to SDPF1.

Also a flow-through SCR-catalyst and a flow-through NO_x storage catalyst (NSC) were analyzed. The sample lengths were 7.5 cm and 4.4 cm respectively (as provided by the industrial partner, IAV GmbH). As both have been flow-through substrates, the channels are not plugged at the ends. No filter effect is intended and the walls themselves are not porous. All specifications are given in **Tab. 3.1**.

Tab. 3.1: Specifications of the samples used in this study.

Filter Parameter	SDPF1	SDPF2	SCR-Catalyst	NSC
Type	Wall flow	Wall Flow	Flow-through	Flow-through
Wall Material	SiC	SiC	Cordierite	Cordierite
Length / cm	6.0	8.1	7.5	4.4
Frontal area / cm ²	1.69	2.26	2.10	1.45
# Channels on front	100	100	121	80
Cell density / cpsi	350	286	375	400
Wall thickness / μm	300	300	150	100
Material porosity / %	48.0	41.2	-	-
Mean pore size / μm	26.6	17.0	-	-
Catalytic coating	Cu-zeolite	Cu-zeolite	Cu-zeolite	Pt/Pd/Rh and Ba/Ce on Al ₂ O ₃
Washcoat manufacturer	Johnson Matthey	-	-	BASF
Substrate Manufacturer	Corning	-	-	-

**Fig. 18** Photographic picture of an SDPF sample prepared for soot loading and model gas measurements.

3.1.2 Dissolution of the zeolite from the SDPF

In order to determine catalytic properties of the pure soot, the zeolite layer was removed from the SDPF sample before soot loading to obtain a bare soot filter. For that purpose, the SDPF sample was immersed in 1 M aqueous NaOH solution at a temperature of 353 K for 24 h, followed by washing the resulting SiC filter substrate (referred to as »bare filter substrate«) with distilled water and drying for 2 h at 423 K in an oven while flushing with ambient air. Then, the bare filter substrate was loaded with soot (see chapter 3.3.3) prior to model gas experiments. In preliminary experiments the bare filter substrates were proved to show no NH₃ storage or NH₃ DeNO_x performance.

3.2 Characterization

3.2.1 Hg-Intrusion on SDPF Sample

Mercury (Hg) intrusion porosimetry has been used to determine the pore size distribution of the porous filter wall material. Prior to porosimetry investigation, a piece of the SDPF was coarse grained in a manner, that only the channels were destroyed but not the porous walls. The investigations were performed on a Porotec Instrument (Pascal 440 Series). Using the Porotec software, the mean macropore width was calculated applying the Washburn equation. Pores diameters ranging from 0.005 µm to 100 µm were analyzed.

3.2.2 Scanning Electron Microscopy of SDPF Sample

Soot free and soot loaded SDPF samples were analyzed by means of scanning electron microscopy combined with energy-dispersive X-ray spectroscopy (SEM-EDX) to examine the structure and the elemental distribution. Prior to investigation, the soot free SDPF sample was cut perpendicular to the channel axes to reveal the channels cross section. The thickness of the cut SDPF pieces was 2 mm. Then it was mounted on a sample holder. For investigation of the soot loaded SDPF sample, prior to soot loading (see chapter 3.3.3) the mid part (3 mm) of the sample was sawed out (compare **Fig. 19**). Afterwards it was accurately adjusted (channel on channel to restore filter layout) and wrapped in adhesive heavy-duty aluminum foil. After soot loading, the mid part was carefully removed and mounted on a SEM sample holder. Using a MED 010 device (Balzers) gold was vapor deposited on the sample. SEM measurements were performed on a LEO 1530 (Leo Electron Microscopy Ltd.) using an acceleration voltage of 5 kV and a working distance of 10 mm.

To prepare a cut SDPF piece for SEM-EDX investigation, it was embedded in an epoxy resin, manually grinded and polished in a Dimple Grinder (Gatan, Pleasanton, CA, USA) using 0.05 μm Al_2O_3 suspension in water (Buehler, MasterPrep Polishing Suspension). After mounting on a holder, carbon was vapor deposited on the sample using a CED 030 device (Balzers). SEM-EDX measurements were performed on a LEO 1530 (Leo Electron Microscopy Ltd.) applying a Link Pentafet EDX detector (Oxford Instruments) using an acceleration voltage of 20 kV and a working distance of 15 mm. The program Inca 4.06 (Oxford Instruments) was used for the elemental analysis and mapping.

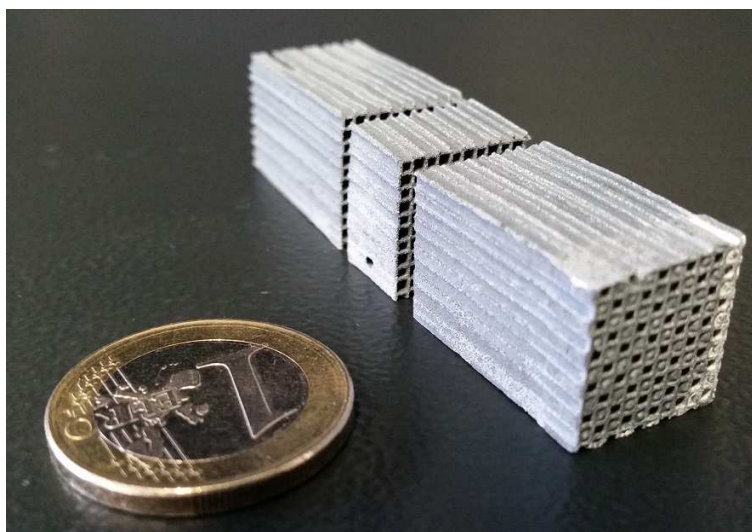


Fig. 19 Photographic picture of an SDPF sample, as it was prepared for soot loading prior to SEM investigation.

3.2.3 Pulsed Field Gradient Nuclear Magnetic Resonance on Model Soot

The Pulse Field Gradient NMR (PFG-NMR) is a technique to measure molecular self-diffusivities. Thereby, a specially designed sequence of radio frequency pulses (RF) and magnetic field gradient pulses are applied, leading to the formation of a spin-echo. Its intensity depends on the sequence parameters, the nuclei under study and the molecular self-diffusivity of the species carrying the nuclei [146]. The PFG-NMR technique is of non-invasive nature as it only acts on the nuclear magnetic moment of the system under study. Two types of information are accessible by the NMR measurement: The amount of molecules (derived from signal intensity of the free induction decay, FID) and the molecular self-diffusivity (derived by means of PFG-NMR). A comprehensive introduction into PFG-NMR can be found in [147,148].

In this study the measurements were carried out using the homebuilt PFG-NMR spectrometer FEGRIS 400 NT operating at a ^1H resonance frequency of 400 MHz [149]. For all measurements, the 13-interval pulse sequence was applied [148,150]. The self-diffusivities presented here are obtained by measuring the attenuation of the spin-echo signal S as a function of the amplitude of the applied field gradient. The amplitude was varied from 0.05 T m^{-1} to a maximum value of 20 T m^{-1} .

The samples for PFG-NMR were prepared as follows. Prior to measurement, the SDPF sample was soot loaded (see chapter 3.3.3) and cut (see chapter 3.2.2 and **Fig. 19**). About 300 mg of the chopped SDPF sample (filter structure preserved) were introduced into an NMR tube. Then the tube was connected to a vacuum system. The sample was activated by keeping it under high vacuum at 673 K for 20 h. Subsequently, the test gas molecules, e.g. NH_3 , were adsorbed on the sample at 298 K using the computer-controlled adsorption setup explained in [146]. The soot loaded SDPF samples were saturated with NH_3 at 10^5 Pa . Upon loading with the test gas molecules, the tube was sealed and removed from the vacuum system before introducing in the PFG-NMR device. The measurements were performed with a diffusion time of $t_d = 5 \text{ ms}$, 10 ms and 20 ms of the 13-interval pulse sequence.

3.3 Soot Loading Apparatus

During diesel combustion in an engine, next to the soot particles several other fuel or lubricant derived components could form, attaching to the soot. Furthermore the soot mass flow and properties (particle size distribution, OC-to-EC-ratio) strongly depend on the engine operation mode [109]. To have a defined and reproducible soot, which equals real diesel soot in its main properties and enables a fast DPF loading in the laboratory, a model soot is essential. Due to very good conformance to diesel engine soot, a propane burning soot-generator was strongly recommended for appropriate studies [104,109].

In this work, soot has been generated by a miniCAST (Combustion Aerosol Standard) soot-generator (Model 5201 Type C) from Jing Ltd. The soot generation is realized by means of a diffusion flame with propane (purity > 99.5 %, Linde-Gas) as fuel. In the diffusion flame oxygen and the fuel gas could only react in the flame front. As the lighter hydrogen atoms (compared to carbon or hydrocarbon) faster diffuse to the flame front, the inner part of the flame is carbon rich. Oxygen excess leads to high particle formation rates within the inner zone. Flushing an inert gas (e.g. nitrogen) as quench gas into the upper part of the

diffusion flame stops a further oxidation of the particles, resulting in high particulate output [109,151]. A schematic illustration of the combustion chamber is given in **Fig. 20**. Hence, depending on fuel gas, air and quench gas composition, highly stable particulate mass flow with mean particle sizes between 26 μm and 340 μm could be produced. Thereby, the chemical composition (EC-to-OC-ratio) depends on the particulate size. Larger particles have a higher ratio of elemental carbon [109]. The particle size distribution with a mean particle size of 70 nm to 100 nm represent the particle size distribution of diesel engines. The chemical composition of propane burner soot was proven to be 90 % to 96 % EC [107], which is the same for soot filtered in DPF downstream a DOC (converts most of HCs attached to soot) [109]. Hence, the oxidation behavior of model soot with 85 nm in diameter is equal to diesel engine soot, making it to a highly representative replacement of diesel engine soot for laboratory studies. For the phenomenological investigation presented here, a stable soot is essential.

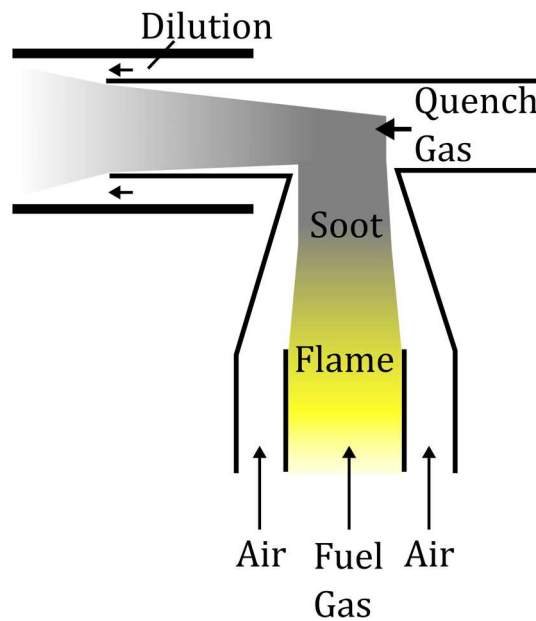


Fig. 20 Schematics of the combustion chamber within the soot-generator.

3.3.1 Set-up

A soot loading apparatus was developed and built to bring a defined soot loading in an SDPF sample. A photographic picture of the apparatus is given in **Fig. 21** on the left. The appropriate flow diagram is shown on the right. In this study, an SDPF sample holder as described by Bensaid *et al.* [113,152] was used. It allows the measurement of the pressure upstream (p_{up}) and downstream (p_{down}) of the filter sample while loading with soot. The difference of p_{up} and p_{down} is subsequently called backpressure Δp . The backpressure was

measured by means of a 0 kPa – 500 kPa pressure sensor module (from Hygrosens). A self-written MATLAB® tool was used for data logging and plotting. Furthermore, it calculated (eq. (3.1)) in real time the soot loaded amount to monitor the loading status of the SDPF sample. The sample holder allowed maximum sample length of 24 cm and a maximum diameter of 22 mm. All pipes (stainless steel) were heated on 473 K to prevent condensation of water arising during combustion. The sample holder itself was heatable up to 973 K. Heating cords as well as HT43 temperature controllers from Hillesheim™ were used.

The core unit of the soot loading apparatus is the miniCAST soot-generator (as explained above). It was supplied with propane, nitrogen and air. The miniCAST was controlled via its miniCAST control software enabling a variation of the fuel gas composition and hence of the soot particulate properties. Propane could be dosed in the range of 20 ml min⁻¹ to 80 ml min⁻¹. Oxygen was variable in the range of 0 to 2 l min⁻¹, which results in air-fuel equivalence ratios (λ) between 0 and 4.1. To adjust the size of the output particles, the propane could be diluted with up to 400 ml min⁻¹ of N₂ prior to combustion. Nevertheless, not every fuel gas composition ended up in stable combustion and soot production (see chapter 5.1). Additionally, up to 20 l min⁻¹ air could be dosed into the exhaust gas for dilution purpose or to adjust the space velocity over the sample while soot loading.

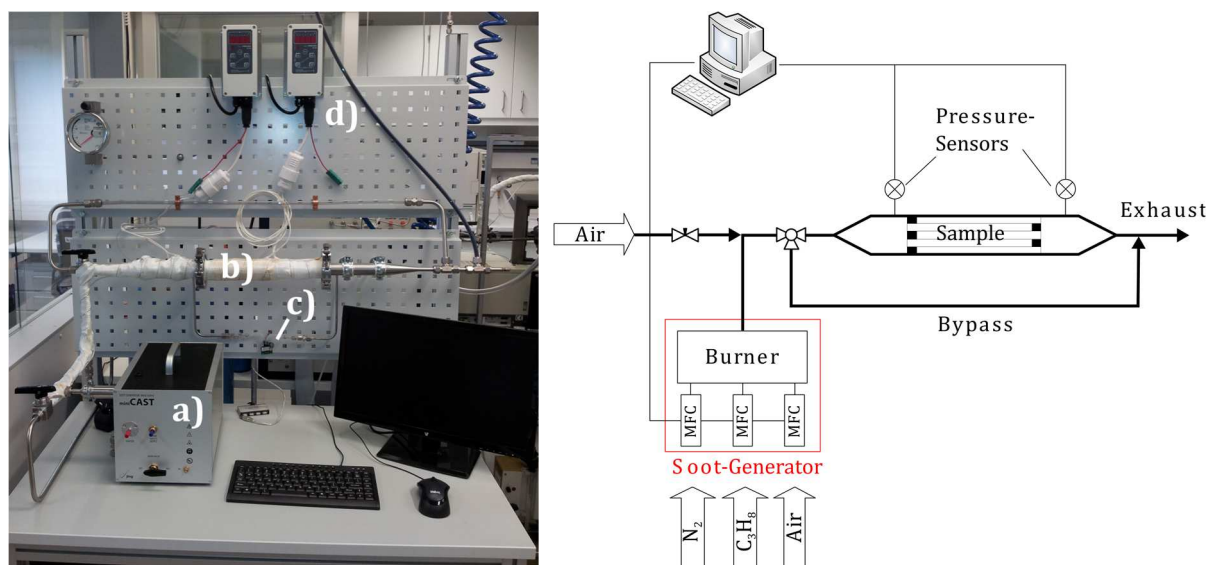


Fig. 21 Left: Photographic picture of the set up apparatus for soot loading of samples with: a) soot-generator, b) sample holder, c) differential pressure sensor and d) heat controller. Right: Flow diagram of the apparatus used for soot loading of the samples (MFC: Mass Flow Controller).

3.3.2 Soot Characterization

The miniCAST soot-generator allows a wide range of operation conditions due to a variation of the fuel gas composition (as given above). The combustion process is affected by the fuel gas composition. Hence, the properties of the output soot particulate flow depend on the fuel gas. Within this study a set of operation conditions (**Tab. 8.2**, Appendix) was evaluated by means of particle size distribution and particulate mass flow to find a model soot, which equals real diesel engine soot in its main properties.

3.3.2.1 Particle Size Distribution

The particle size distribution was measured by a TSI Engine Exhaust Particle Sizer Spectrometer (EEPS™) 3090. The principle of operation is briefly described in following. Prior to analyzation the particles within the gas stream are charged. The detection column consists of an array (32) of oppositely charged precision electrodes. The charged particles are attracted towards the electrodes. Due to its inertia, heavier particles hit a detector more downstream compared to lighter particles. This allows to distinguish particle sizes between 5.6nm and 560 nm into 32 fractions while counting the number of particle hitting each detector electrode. As the maximum detectable particle concentration per detector electrode (up to 1.7×10^6 per cm^3) was exceeded by the particle output of the miniCAST, a Rotating Disc Thermodiluter (Model 379020) of TSI with 3000-fold dilution was installed in between the miniCAST and the EEPS. An electric conductive tube (TSI) was used as connection between the devices to prevent particulate deposits on the inner surface of the tube.

3.3.2.2 Particle Mass Flow

The soot mass flow was determined by means of an AVL 483 Micro Soot Sensor (MSS). The soot particles in the measuring chamber become thermally stimulated by a modulated laser beam. Their periodic pulsation could be detected as acoustic wave, which is translated in a mass flow signal by the AVL software. As the maximum detectable soot mass flow (up to 50 mg m^{-3}) was exceeded by the particle output of the miniCAST, a Rotating Disc Thermodiluter (Model 379020) of TSI with 33-fold dilution was installed in between the miniCAST and the MSS.

3.3.3 Soot loading procedure for the Particulate Filters

Prior to soot loading, the sample was wrapped in heavy duty aluminum foil (compare **Fig. 18**). After its positioning in the sample holder, the gap between the sample and the wall was filled with quartz wool and $\alpha\text{-Al}_2\text{O}_3$ suspension (99.5 %, 10 μm powder, Sigma Aldrich Co.) to form a gastight seal after drying at room temperature for 60 min (see **Fig. 23** left). This technique was already proven in [4]. Preventing gas and soot to bypass the sample is essential to have a reproducible loading and to correctly determine the soot loaded amount in the filter. The cross section of the sample was chosen to be quadratic with a certain amount of parallel channels (see **Tab. 3.1**). None of the outer channel walls (in axial direction) were damaged to sustain the filter effect. Prior to soot loading, the SDPF sample was kept in the sample holder for 30 min at 473 K under air-flow until the temperature was constant within ± 2 K. Unless otherwise stated, the operation point used for the soot-generator was set to 60 ml min^{-1} propane mixed with 100 ml min^{-1} N_2 and 1.57 l min^{-1} air. The appropriate soot particles have a mean size of 80 nm. The soot mass flow was determined to be 42 mg h^{-1} at this operation point (see chapter 5.1). During soot loading (also performed at 473 K), a GHSV of 100.000 h^{-1} (volumetric gas flow of 18.7 l min^{-1} over SDPF1 sample) was fixed to establish a gas velocity inside the filter, which is close to real car applications. In a very good approximation of a filtration efficiency of close to 100 % [98,119], the trapped soot mass could be calculated by integrating the soot mass flow over time (eq. (3.1)). The obtained soot mass loaded in the filter samples were validated against the carbon-balance from the sample regeneration in model gas (integrated carbon mass from CO and CO_2 released during oxidation, eq. (3.2)). Both methods were in good agreement (see **Fig. 61**, Appendix). In the following, the soot mass loaded on the sample is abbreviated as m_{soot} . Corresponding values are given in g soot per l of SDPF volume (in g l^{-1}). **Fig. 22** shows a soot loaded SDPF sample used in this work. On the left, the sample is shown immediately after the soot loading procedure, still mounted in the sample holder. On the right, the front end of the heavily loaded ($m_{\text{soot}} = 10 \text{ g l}^{-1}$) SDPF sample was cut, revealing that every second channel (inlet channel) is filled with soot.

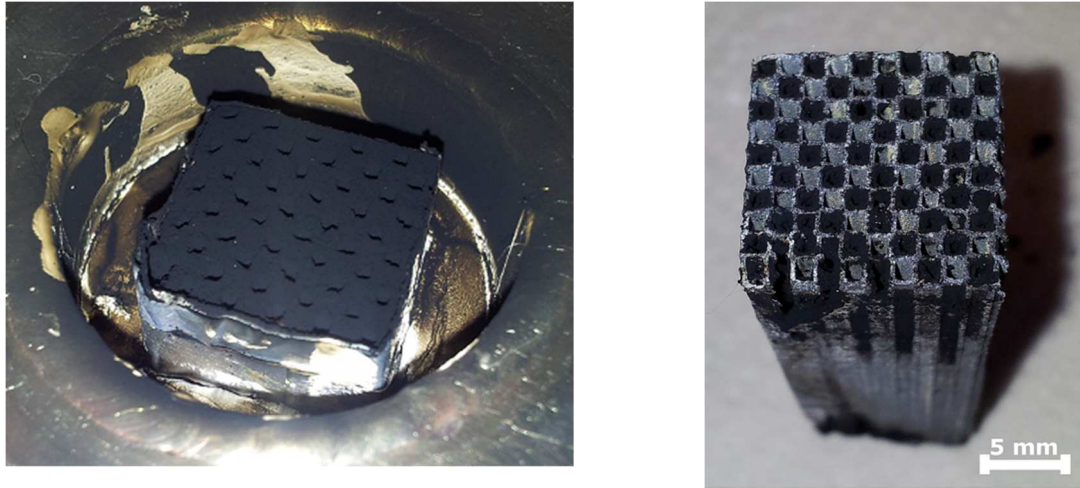


Fig. 22 Left: Photographic picture of a soot loaded sample immediately after termination of soot loading (still remained in the sample holder), Right: Soot loaded monolithic SDPF sample. For better visibility of the soot loading, the plugs at the top end were removed by cutting the sample.

$$m_{\text{soot}} = \int \dot{m}_{\text{soot,OP}} dt / V_{\text{sample}} \quad (3.1)$$

$$m_{\text{soot}} = \int \left((y(\text{CO}) + y(\text{CO}_2)) \frac{\dot{V} \cdot \text{MW}_c}{c_{\text{id.gas}}} \right) dt / V_{\text{sample}} \quad (3.2)$$

3.4 Catalytic Characterization using Model Gas Experiments

A bench flow reactor was used to study the catalytic properties of the samples. The model gas test bench, as described earlier [4,153], utilized a gas mixture of up to nine different components (*e.g.* NH_3 , NO , NO_2 , O_2 , water vapor). The samples, mounted in a steel reactor with a coating of amorphous silicon by SilcoTek (Bellefonte, PA, USA), is impinged with the model gas mix. The outlet concentrations are measured by means of a multigas 2030 FTIR by mks instruments (Andover, MA, USA) and an OXY-FLEX-0 oxygen sensor by SST Sensing (Coatbridge, UK). The reactor was embedded in a tube furnace.

Prior to investigation, the sample under study was equipped with thermocouples at the entry and the exit as well as another one 2 cm above the entry to measure gas temperature. After positioning the sample in the reactor (see **Fig. 23** right), the gap to the reactor wall was filled with quartz wool. $\alpha\text{-Al}_2\text{O}_3$ suspension (purity > 98 %, 10 μm powder, Sigma Aldrich Co.) was used as gastight seal. Preventing gas to bypass the catalyst sample is essential to correctly determine the NO_x conversion or the NH_3 slippage.

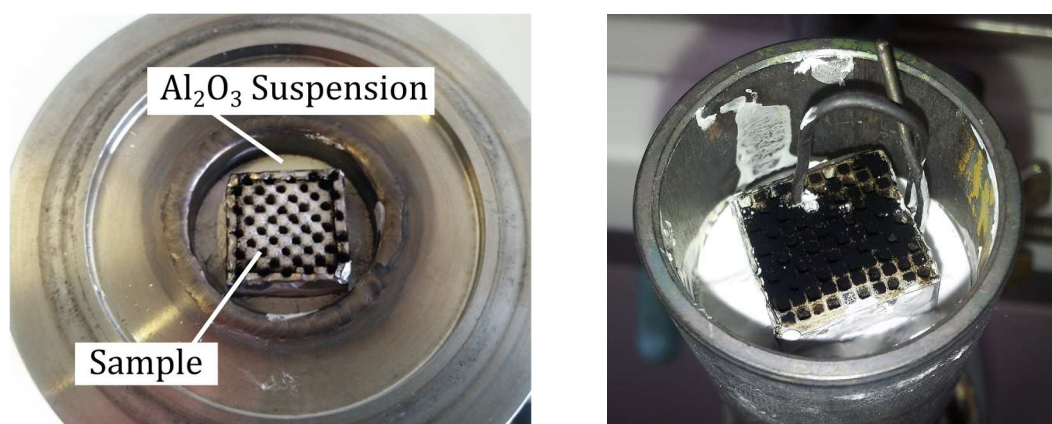


Fig. 23 Left: Photographic picture of an SDPF sample mounted in the sample holder for soot loading. Right: Photographic picture of a soot loaded SDPF sample, equipped with thermocouples, mounted in the reactor for investigation in model gas. In both cases the sample was stabilized in the tube by means of quartz wool, a Al_2O_3 suspension was used as gastight seal.

3.4.1 Pretreatment, Regeneration and Hydrothermal Ageing

New samples (as cut from the full size SDPF), were degreened for 120 min in a furnace at 923 K in ambient air. Soot removal (regeneration) was achieved by heating the soot loaded sample to 923 K (linear ramp of 10 K min⁻¹) and holding this temperature for 60 min in a gas-stream (GHSV = 40.000 h⁻¹) containing 10 vol.-% O₂ in N₂. The regeneration procedure was performed after either the NH₃-SCR or the TPD experiments. The concentrations of CO and CO₂ released during oxidation were recorded by means of a FTIR (Fourier Transform Infrared Spectrometer). This data was used to calculate the amount of carbon deposited on the SDPF sample.

Hydrothermal (HT) ageing was done by heating the SDPF sample up to 923 K in a furnace in ambient air and remaining at this temperature for several hours e.g. 18h or 39 h. After HT treatment, the sample was characterized in model gas.

3.4.2 Temperature Programmed Desorption of NH₃

For characterizing the NH₃ storage behavior over soot free and soot loaded samples, adsorption/desorption experiments were conducted. Prior to each experiment, the sample was heated to 873 K (10 K min⁻¹) in flowing N₂ (GHSV = 40.000 h⁻¹) to remove adsorbed volatile organic compounds from the catalyst surface. After cooling to the adsorption-temperature of 423 K, 523 K or 623 K in N₂, NH₃ (200 ppm, 1000 ppm or 3000 ppm) is added to the N₂ feed gas until the inlet NH₃ concentration equals the outlet NH₃ concentration (compare, **Fig. 34** part a)). Then, NH₃ dosing is switched off, followed

by flushing with N_2 to remove loosely bonded NH_3 (part b) and a temperature-programmed desorption (TPD) with a heating rate of 10 K min^{-1} (part c) to desorb the strongly bonded NH_3 . The space velocity GHSV = 40.000 h^{-1} , 80.000 h^{-1} or 120.000 h^{-1} was kept constant during the whole experiment. The NH_3 storage was calculated from the area under the curve of the desorbed NH_3 volume fraction (in following referred to as concentration in ppm). It is given as mass of desorbed NH_3 per SDPF volume (g l^{-1}). The amount of adsorbed NH_3 was calculated as the area between the inlet and the outlet NH_3 concentration during part a (adsorption). The equation is given in (3.3). Applying eq. (3.3) on part b and c yields the amount of desorbed NH_3 .

$$m_{NH_3} = \left| \int (y(NH_3, \text{in}) - y(NH_3, \text{out})) \frac{\dot{V} \cdot MW_{NH_3}}{c_{id, \text{gas}}} dt \right| / V_{\text{sample}} \quad (3.3)$$

3.4.3 Standard-SCR-Experiments

The SCR activity of the samples before and after soot loading were investigated for their catalytic properties on the NH_3 -SCR of NO. The gas hourly space velocity (GHSV) was kept at 40.000 h^{-1} or 80.000 h^{-1} . For a light-off curve, first 1000 ppm NH_3 were dosed with 5 vol.-% H_2O and 10 vol.-% O_2 in N_2 at 423 K. When the NH_3 saturation was reached (NH_3 inlet concentration equals NH_3 outlet concentration), additionally 800 ppm NO were added to the feed gas, while the temperature was ramped from 423 K to 673 K at 2 K min^{-1} .

3.4.4 NO Adsorption Experiments on NO_x Storage Catalyst

To characterize the NO_x storage behavior of a soot free and soot loaded NSC sample, NO adsorption/regeneration experiments were conducted. Prior to the experiment, the sample was heated to the appropriate adsorption temperature (473 K, 523 K or 573 K) in a stream of 10 vol.-% O_2 in N_2 (GHSV = 40.000 h^{-1}). Additionally, 1000 ppm propylene was dosed for 60 min to release all bound NO_x from the NSC. For the adsorption experiment propylene was switched off and 200 ppm NO was dosed in a stream of 10 vol.-% O_2 in N_2 for 60 min, followed by 10 min of flushing with 10 vol.-% O_2 in N_2 to release loosely bound NO_x . For regeneration again 1000 ppm propylene was additionally dosed until the inlet concentration equals the outlet concentration.

4 Modelling

4.1 Mathematical Model

To study the effect of soot deposited within the porous filter wall upon the SCR DeNO_x behavior, the relation between the SCR catalyst location in the wall and the location of the in-wall soot deposits is of major importance. If, by depth filtration, the soot only penetrates inside the filter wall in close vicinity to the inlet channel and the SCR catalyst is (by washcoating technique) solely coated at the downstream portion of the filter wall, thus, no influence of soot on the SCR DeNO_x is expected. In case of soot deposition on top of the SCR catalyst containing washcoat within the porous wall, an influence of the soot on the catalytic behavior is possible. To set up a model, representing the physico-chemical situation within the SDPF porous filter wall under study, SEM measurements were used for structural investigations. In SEM-EDX (**Fig. 24** and **Tab. 4.1**) two different structures are visible. The coarse grains belong to the SiC filter substrate while the washcoat containing the Cu-zeolite is represented by the fine grains. The Cu-zeolite is homogeneously distributed over the entire thickness of the porous filter wall. This feature was implemented in the model as described below (**Fig. 26**, middle part). An appropriate SEM image is given in the appendix (**Fig. 59**).

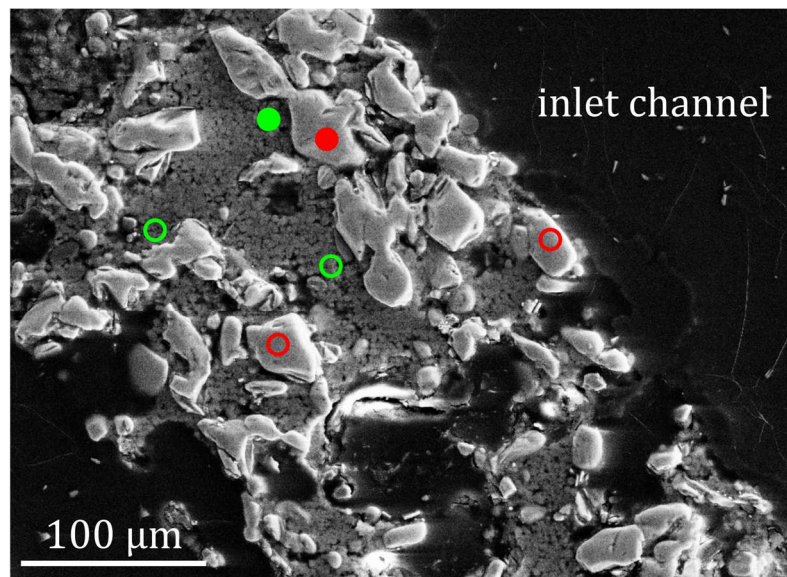


Fig. 24 SEM picture of a cross section of the porous filter wall of SDPF1. The cut surface was sealed with epoxy resin and polished. The colored circles indicate the positions of the SEM-EDX measurements for element detection. The coarse grains (red circles) belong to the SiC filter substrate while the finely grained section (green circles) is the washcoat containing the Cu-zeolite. The corresponding analysis results are given in **Tab. 4.1**.

Tab. 4.1 Molar fractions of the elements detected via SEM-EDX in the cross section of the SDPFs porous filter wall (presented in **Fig. 24**, full colored circles) for two representative positions. Additional positions (colored rings) were analyzed and show similar results (standard deviation given in the table). The C signals was caused by the sample preparation with epoxy resin.

molar fraction / %	SiC	Zeolite
C	56.51 ± 1.31	34.96 ± 4.18
O	1.57 ± 0.91	42.09 ± 4.16
Al	0.00 ± 0.10	4.10 ± 0.48
Si	41.92 ± 0.48	18.26 ± 0.12
Cu	0.00 ± 0.04	0.59 ± 0.00

Next to the homogeneous distribution of the washcoat inside the wall, the SEM pictures reveal that there is no “stop-layer” on top of the inlet channel. The stop-layer SDPF configuration was already discussed in [120]. Thus, a permeable layer without catalytic activity and of a fine porosity located on top of the porous and washcoated wall of the filter substrate towards the inlet channel is absent in the studied samples. Such a stop-layer would prevent the soot to penetrate inside the washcoated SDPF pores.

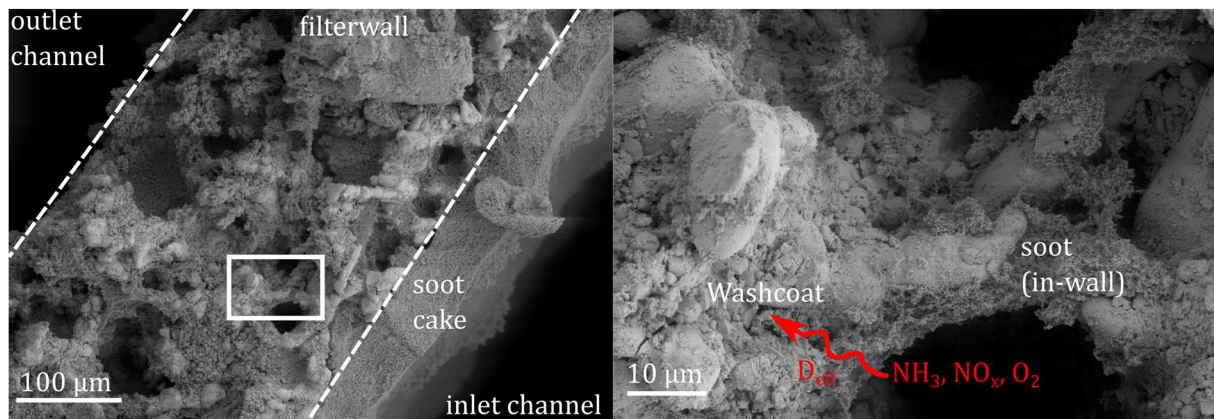


Fig. 25 SEM images of the cross section of one porous SDPF1 filter wall. The sample was soot loaded with $m_{\text{soot}} = 7 \text{ g l}^{-1}$, Left: cross section at 200 times magnification, Right: cross section at 1500 times magnification revealing the soot layer on top of the washcoat inside the porous filter wall. The arrow indicates the assumed gas transport through the soot layer inside the wall.

In **Fig. 25** a SEM measurement of a cross section of the porous SDPF filter wall is depicted. The sample was soot loaded with $m_{\text{soot}} = 7 \text{ g l}^{-1}$. The image with 200 times magnification (left side) clearly reveals the two possible locations for soot deposition [114,126,145]. When the wall is saturated and the surface pores are blocked [114], soot will form a cake layer in the inlet channel on top of the porous filter wall. In the initial stage of the loading

process, soot will be trapped inside the porous wall. There, soot deposits are formed, covering the Cu-zeolite containing washcoat (**Fig. 25** right and **Fig. 60**, Appendix). To get to the active sites located in the washcoat, the reaction gas molecules have to diffuse through the porous soot deposits. The diffusive gas transport within the porous filter wall was implemented in the model as explained in the following.

The SCR coated wall flow diesel particulate filter is modelled as a set of channel pairs (**Fig. 26** left). The unit collector model is used as calculatory domain to mimic the porous filter wall. The in-wall soot deposits are modelled as a layer covering the washcoat. For modelling purpose its thickness is called d_s . To account for an inhomogeneous soot distribution throughout the filter wall, the simulation was done brickwise. Perpendicular to the direction of the gas flow the filter wall was divided into bricks (all of the same size, **Fig. 26**, middle part). Each brick represents a calculatory domain for which the system of differential equations (4.1) to (4.4) for mass conservation has been solved. Implementing soot layer with thicknesses $d_{s,1...n}$ (on top of the washcoat) of each brick, a soot distribution throughout the filter wall could be achieved. Each d_s indicates, by the unit collector model, the amount of soot in this brick. As the geometric parameters of a unit collector cell (**Fig. 27**) depend on the amount of soot inside, the prefactors on the right hand side of equations (4.1) to (4.3) are different among the bricks when a soot distribution is considered. For each gas species, the outlet concentration of each brick was set equal to the inlet concentration of the following brick in flow direction towards the outlet channel. For the first brick, the inlet concentration equals the concentration at the inlet channel. Iteratively for each gas species, the outlet concentration of the whole filter wall can thus be calculated. In this study, the wall is represented by 40 bricks, which provides a compromise between local resolution and calculation time.

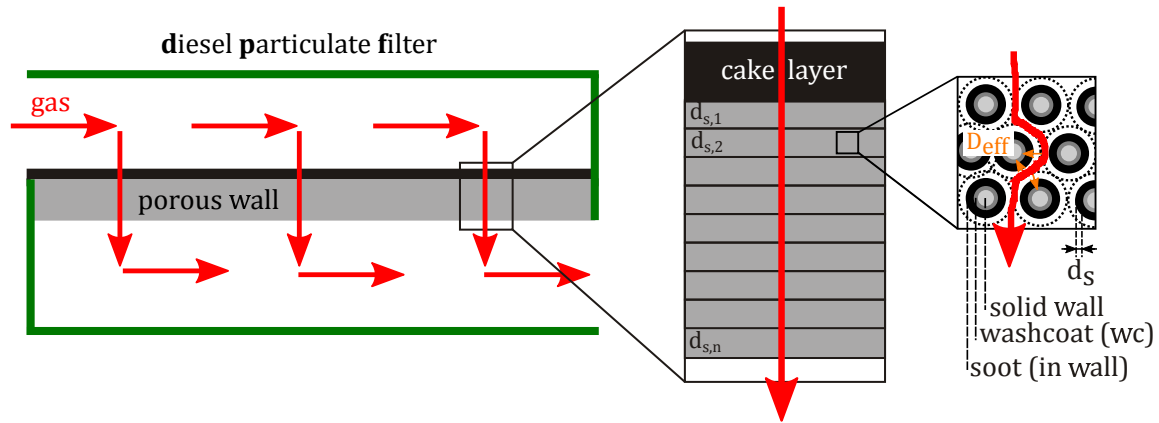


Fig. 26 Schematic representation of a channel-pair model within a wall flow SDPF showing the location of soot deposition as a “cake” on the pore wall (left and middle part), a magnification of the pore wall section with the cake layer and the porous wall divided into several bricks with different soot layer-thickness $d_{s,1}$, $d_{s,2}$, ..., $d_{s,n}$ along the direction of the gas flow (middle part) and a magnification of a section within a brick schematically displaying the porous filter wall consisting of unit collector cells with the washcoat and the in-wall filtered soot as well as the gas transport inside the filter wall (right part).

To calculate the filter backpressure, the unit collector model after Serrano *et al.* [126] (see chapter 2.3.2) has been applied (**Fig. 43**). Next to the backpressure contribution by the cake layer inside the channel, Serrano’s model is able to describe the initial stage of filtering when the soot is trapped inside the porous wall. The wall is assumed to be a dense packaging of collector cells. These spheres consist of a spherical unit collector (wall material, diameter d_{co}) which is surrounded by void so that the experimentally determined wall porosity and mean pore width are represented (values given in **Tab. 3.1**). This configuration with diameter d_{cell} is called collector cell, schematically presented in **Fig. 27**. When soot is trapped inside the porous wall during loading, it distributes around the collector unit, resulting in its diameter-increase. As there is less void available for the gas flow, the permeability of the porous wall decreases with increasing amount of wall-soot, which leads to an elevated backpressure. The geometric aspects of this wall filtration model allow the estimation of the soot layer-thickness d_s covering the inner unit collector, on which the washcoat with a volume of V_{wc} is located. The soot density $\rho_{s,w}$ is obtained as a fit parameter, applying Serrano’s model to the experimental backpressure curve.

Under the assumption that all inlet channels have the same boundary conditions, *i.e.* no radial gradients, one pair of inlet/outlet channel is sufficient to describe the overall system. In this study, the mass conservation equations for the gas phase species (based on [68,154]) were applied on the unit collector model. The mass conservation equations

were complemented by diffusive transport equations to account for the situation in SDPF. Thus, the concentration profiles at each brick of the porous wall could be calculated.

$$\frac{dx_{g,k}}{dt} = \frac{\dot{V}}{n_{\text{cell}}V_{\text{void}}} (x_{\text{in},k} - x_{g,k}) - \beta_k \frac{A_s}{V_{\text{void}}} (x_{g,k} - x_{s,k}) \quad (4.1)$$

$$\frac{dx_{s,k}}{dt} = \beta_k \frac{A_s}{V_{s,\text{layer}}} (x_{g,k} - x_{s,k}) - \frac{A_{wc}}{V_{s,\text{layer}}} \frac{D_{\text{eff},k}}{d_s} (x_{s,k} - x_{wc,k}) \quad (4.2)$$

$$\frac{dx_{wc,k}}{dt} = \frac{A_{wc}}{V_{wc}} \frac{D_{\text{eff},k}}{d_s} (x_{s,k} - x_{wc,k}) - \sum_{i=1}^{nr} s_{km} r_i(x_{wc,k}, \theta) \quad (4.3)$$

$$\frac{d\theta_j}{dt} = \frac{c_{\text{id,gas}}}{\Gamma_j} \sum_{i=1}^{nr} s_{ji} r_i(x_{wc,k}, \theta) \quad (4.4)$$

Since the heat associated with NH_3 SCR is very low a heat balance was not included [68]. Further, the SDPF sample was placed inside the heating zone and the measured temperatures were used for calculation. The concentration and mass flow gradient over the channel length have been neglected since the experimentally accessible values of NH_3 slip and NO conversion are average values over the channel length. The authors in [68] and [51] proved the applicability of a 0-D channel model for sufficiently small samples (studying short monolithic samples with length below 60 mm).

The coefficients in eq. (4.1) to eq. (4.3) were chosen in accordance to the geometry of the unit collector model presented in **Fig. 27**. For the sake of simplicity, no momentum balance was considered. In the calculation, four concentrations are involved: 1. $x_{\text{in},k}$ the mole fraction of gas species k entering one brick (**Fig. 26**, middle part), 2. $x_{g,k}$ the mole fraction of the gas species k inside the void of the porous wall inside of one brick, 3. $x_{s,k}$ the mole fraction of species k at the surface of the soot layer inside the porous wall of one brick and 4. $x_{wc,k}$ the mole fraction of species k at the washcoat within the brick. The term $\frac{\dot{V}}{n_{\text{cell}}V_{\text{void}}} (x_{\text{in},k} - x_{g,k})$ on the right hand side of eq. (4.1) is the source term for the gas concentration within the pores of the filter wall $x_{g,k}$. Thus, it assigns $x_{g,k}$ with the appropriate concentration entering the brick under consideration of the volumetric flow rate \dot{V} through the void volume $n_{\text{cell}}V_{\text{void}}$ in the porous wall. n_{cell} is the number of collector cells and V_{void} is the volume of the void per collector cell. The terms implementing the mass transfer coefficient β_k in eq. (4.1) and (4.2) cause the convective

transport of species k from the gas stream ($x_{g,k}$) to the top of the soot layer within the porous wall ($x_{s,k}$) or *vice versa*. For the calculation of β_k , the description of [1] was followed, involving the calculation of the Sherwood number and the binary diffusion coefficient D_{AB} .

$$D_{AB} = \frac{1.013 \cdot 10^{-2} T^{1.75} \sqrt{\frac{1}{M_A} + \frac{1}{M_B}}}{p[(\sum v_i)^{1/3}_A + (\sum v_i)^{1/3}_B]^2} \quad (4.5)$$

According to the previous study of Park *et al.* [145], the negative impact of the soot deposit on the NO conversion was assumed here to have its nature in a mass transfer limitation. To account for this, Park applied the concept of the Thiele modulus (normally used for description of a diffusion inside the washcoat) to the soot inside the porous wall of the SDPF. Park *et al.* suggested the diffusion process through soot to be Knudsen diffusion. The reaction rates involved in SCR were reduced by an effectiveness factor, which is smaller than unity due to the gas diffusion through the soot deposit on top of the washcoat. Hence, Park reduced the reaction rates in presence of soot to take account for the observed effects.

To account for mass transfer limitation by the soot, in this study the gas concentrations $x_{s,k}$ and $x_{wc,k}$, were introduced. Fick's first law for diffusion (J_k ...molar flux in $\text{mol m}^{-2} \text{s}^{-1}$ and c_k ...concentration in mol m^{-3})

$$J_k = -D_{\text{eff},k} \frac{\partial c_k}{\partial x} \quad (4.6)$$

was directly implemented in the governing equations for gas phase species transport eqs. (4.2) and (4.3) to take the diffusion through the in-wall soot layer into account. This results in a system of ordinary differential equations. Thereby, $D_{\text{eff},k}$ indicates the effective diffusivity of gas species k through the soot layer. The terms on the right hand side of eq. (4.2) and eq. (4.3) implementing $D_{\text{eff},k}$, thus, cause diffusive transport of the gas species from the surface of the soot layer to the washcoat or *vice versa*. The outer surface of the soot in the collector cell (area A_s , volume $V_{s,\text{layer}}$) is assumed to be an accumulation zone for the species from the gas phase. Their diffusive gas flux through the soot-barrier is driven by the concentration gradient between the concentrations at the surfaces of the soot layer $x_{s,k}$ and at the washcoat $x_{wc,k}$, respectively. Only the gas species that diffuse through the soot-barrier (with thickness d_s) take part in the chemical

reactions at the catalyst containing washcoat (area A_{wc} , volume V_{wc}). The summation-terms on the right hand side of eq. (4.3) and eq. (4.4) implement the kinetic model (given in chapter 4.2) into the gas transport mechanism (eq. (4.1) to (4.3)) and the NH_3 storage equation (4.4), respectively, in analogy to [68]).

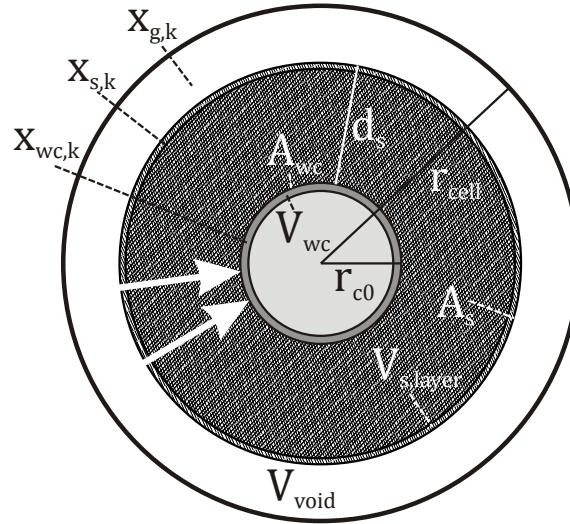


Fig. 27 Schematic representation of the model of a unit collector cell (see **Fig. 26**). The labels are model parameters *e.g.* the thickness of the in-wall soot layer (d_s) as well as other geometric parameters. The white area represents the void space for the convective gas flow, the shaded area indicates the volume occupied by soot and the arrows indicate the diffusive gas flux to the washcoat.

4.2 Kinetic Model

A kinetic model for NH_3 storage and NO conversion was developed and validated against experimental data. The Arrhenius equation (4.7) is used to capture the temperature dependence of the reaction rate constant k_i , where i indicates the number of the reactions given in **Tab. 4.2**.

$$k_i = A_i \exp\left(-\frac{E_{A,i}}{RT}\right) \quad (4.7)$$

$E_{A,i}$ represents the activation energy for reaction i , A_i the pre-exponential factor of reaction i , R the gas constant and T the temperature. The reaction rates r_i were generally modelled as non-linear functions of the species mole fraction, the NH_3 storage filling ratio θ and the kinetic rate parameters k . For the standard SCR reaction, the following inhibition factor (suggested by Koebel *et al.* [155]) was implemented:

$$G_j = 1 + A_j \exp\left(\frac{E_A}{RT}\right) \theta_j \quad (4.8)$$

where j indicates each of the storage sites. As suggested by Sjövall *et al.* [50,51] or Gong *et al.* [154] for zeolite Cu-ZSM-5, a multiple adsorption site model for NH_3 was implemented. In the investigated temperature range of 423 K to 873 K, two types of strong active sites for NH_3 storage were evident from the experimental TPD results (chapter 5.2.1). Additionally, loosely bonded NH_3 , which is carried out from the sample by N_2 feed gas immediately after NH_3 dosing is switched off (part b in Fig. 34 (left) and discussed in [57]), was considered with an additional NH_3 storage site. Thus, three storage sites (denoted as $j = s1, s2, s3$) for the zeolite were implemented in the kinetic model. The NH_3 adsorption on the zeolite is considered by the dimensionless NH_3 storage filling ratio θ_j in eq. (4.4), Γ_j stands for its storage capacity and $c_{\text{id.gas}} = \frac{10^3 \text{ mol}}{22.4 \text{ m}^3}$ indicates the molar concentration of an ideal gas. To account for an appropriate reaction mechanism for each gas species k or each storage site j in eqs. (4.3) and (4.4), the stoichiometric coefficients s_{ki} and s_{ji} were considered. The binding site $s1$ for adsorption and desorption of loosely bonded NH_3 was considered to be not involved in further chemical reactions. Hence, the chemical reactions only take place at chemical binding sites $s2$ and $s3$. The overall kinetic model is able to account for NH_3 adsorption/desorption phenomena, NH_3 oxidation as well as NO conversion according to the standard SCR reaction [68] under soot free and soot loaded conditions. The effect of soot loading was accounted for by a diffusion barrier inside the mass balance eqs. (4.2) and (4.3). The contribution to NH_3 storage by the soot itself was assumed to be small compared to the NH_3 storage of the zeolite (see chapter 5.1.1) and was, therefore, not implemented into the kinetic model.

All kinetic parameters as well as a complete set of the mass conservation equations are given in the appendix (**Tab. 8.1**). The stoichiometric coefficients (s_{ki} and s_{ji}) have been chosen in accordance to the reactions given in **Tab. 4.2**. Thereby, the mole fractions were normalized to NH_3 .

Tab. 4.2 List of reactions implemented in the kinetic model.

No.	Reaction and Reaction rate	Description
1	$\text{NH}_3 + \text{s1} \leftrightarrow \text{NH}_3(\text{s1})$ $r_1 = k_{\text{s1,ads}}(1 - \theta_{\text{s1}})x_{\text{wc,NH}_3} - k_{\text{s1,des}}\theta_{\text{s1}}$	NH ₃ adsorption and desorption at site s1 (loosely bonded NH ₃)
2	$\text{NH}_3 + \text{s2} \leftrightarrow \text{NH}_3(\text{s2})$ $r_2 = k_{\text{s2,ads}}(1 - \theta_{\text{s2}})x_{\text{wc,NH}_3} - k_{\text{s2,des}}\theta_{\text{s2}}$	NH ₃ adsorption and desorption at site s2 (chemisorbed NH ₃)
3	$\text{NH}_3 + \text{s3} \leftrightarrow \text{NH}_3(\text{s3})$ $r_3 = k_{\text{s3,ads}}(1 - \theta_{\text{s3}})x_{\text{wc,NH}_3} - k_{\text{s3,des}}\theta_{\text{s3}}$	NH ₃ adsorption and desorption at site s3 (chemisorbed NH ₃)
4	$4 \text{NH}_3(\text{s2}) + 4 \text{NO} + \text{O}_2 \rightarrow 4 \text{N}_2 + 6 \text{H}_2\text{O} + 4 \text{s2}$ $r_4 = \frac{k_{\text{s2,StdSCR}}\theta_{\text{s2}}x_{\text{wc,NO}}x_{\text{wc,O}_2}}{G_{\text{s2,Inh}}}$	Standard SCR reaction at active site s2
5	$G_{\text{s2,Inh}} = 1 + A_{\text{s2,Inh}} \exp\left(\frac{E_{\text{A,s2,Inh}}}{RT}\right)\theta_{\text{s2}}$	Inhibition of the standard SCR reaction at active site s2 [155]
6	$4 \text{NH}_3(\text{s3}) + 4 \text{NO} + \text{O}_2 \rightarrow 4 \text{N}_2 + 6 \text{H}_2\text{O} + 4 \text{s3}$ $r_6 = \frac{k_{\text{s3,StdSCR}}\theta_{\text{s3}}x_{\text{wc,NO}}x_{\text{wc,O}_2}}{G_{\text{s3,Inh}}}$	Standard SCR reaction at active site s3
7	$G_{\text{s3,Inh}} = 1 + A_{\text{s3,Inh}} \exp\left(\frac{E_{\text{A,s3,Inh}}}{RT}\right)\theta_{\text{s3}}$	Inhibition of the standard SCR reaction at active site s3
8	$2 \text{NH}_3(\text{s2}) + \frac{3}{2} \text{O}_2 \rightarrow \text{N}_2 + 3 \text{H}_2\text{O} + 2 \text{s2}$ $r_8 = k_{\text{s2,NH}_3\text{Oxi}}\theta_{\text{s2}}x_{\text{wc,O}_2}$	NH ₃ oxidation reaction at active site s2 [68]
9	$2 \text{NH}_3(\text{s3}) + \frac{3}{2} \text{O}_2 \rightarrow \text{N}_2 + 3 \text{H}_2\text{O} + 2 \text{s3}$ $r_9 = k_{\text{s3,NH}_3\text{Oxi}}\theta_{\text{s3}}x_{\text{wc,O}_2}$	NH ₃ oxidation reaction at active site s3

4.3 Model Environment and Calibration

The modelling and simulation environment MATLAB Simulink from The MathWorks® (Natick, MA, USA) has been used for model calculation. The kinetic model (**Tab. 4.2**) for the reactions, taking place in the washcoat, was applied on the geometric unit collector cell model (chapter 4.1). The set of mass conservation equations (4.1) to (4.4) constitute a stiff differential equation system. The differential equations were solved by means of the implicit »Rosenbrock« method, implemented in MATLAB Simulink [156].

Calibration of a model means the adjustment of the kinetic parameters (A_i and $E_{A,i}$) in a manner that the calculated reaction mechanism gives results, which are in good agreement with catalytic measurements for a given range of conditions (concentrations, space velocities, temperatures, *etc.*). Optimization is used to achieve this agreement [4]. In this study, the calibration of the kinetic model and fitting parameters *e.g.* the effective diffusivity was found, using a MATLAB tool called »GAIdent« provided by the industrial partner (IAV GmbH). Therein, a genetic algorithm (GA) is used for optimization. On initial stage, the GA choses sets of kinetic parameters by stochastics out of a predefined range. Using the particular parameter sets, model simulations are carried out. Each parameter set is assessed by means of the error function E , giving the discrepancy between model prediction f_{model} and experimental results f_{exp} (see equation (4.9)). On second stage, the GA generates further parameter sets using selection, recombination and mutation processes to minimize the error function and hence to find the optimal model calibration.

$$E = \int (f_{\text{exp}} - f_{\text{model}})^2 dt \quad (4.9)$$

The kinetic model was calibrated against model gas experiments on NH_3 oxidation, NH_3 adsorption/desorption and Standard SCR (experiments and range of conditions as described in chapter 3.4). All kinetic parameters, used in this study, are listed in **Tab. 8.1**.

5 Results and Discussion

5.1 Model-Soot

Varying the air-fuel equivalence ratio λ as well as diluting the fuel gas by N_2 , the miniCAST soot-generator allows a wide range of operation conditions. Aim of this subchapter is the choice of the soot specifications for further investigation. The mean particle size as a function of λ for the possible particle distributions is given in **Fig. 28** (left). Diluting the fuel gas by N_2 results in larger distances between the primary soot particles during combustion and soot particle formation. Hence, the agglomeration process is less effective, ending up with smaller soot particles. To analyze model soot with properties close to real diesel soot, a soot-generator operation point (OP) of $\lambda = 1.07$ (oxygen excess) and 100 ml N_2 mix gas has been chosen for further investigation. The resulting soot has a mean particle size of 80 nm. Its particle size distribution is very similar to engine soot (see **Fig. 28**, right). In **Fig. 29** the soot mass flow as a function of the mean particulate size is plotted. All the data for the analyzed OP are given in **Tab. 8.2** (Appendix). Combining the EEPS data with the MSS data, the mean particle mass for each OP could be evaluated (**Fig. 29**, inset). It shows an over-linear dependence on the particle size. Assuming the soot agglomerates to be spheres, the particle mass as a function of the particle size could be fitted by a cubic function. Thereby, the particle density $\rho_p = (1305 \pm 35) \text{ kg m}^{-3}$ could be revealed as the fit parameter. Comparing to the density of graphene (2260 kg m^{-3}), it is obvious that the agglomerated particles are not spherical, having a fractal dimension as previously found in [99,157]. In previous studies on the chemical composition of propane burner soot [107,109], it was proven to consist of 90 wt.-% to 96 wt.-% EC, which is the same for soot filtered in DPF downstream a DOC (converts most of HCs attached to soot). Hence, the soot chosen for further investigation is a good model replacement for diesel soot.

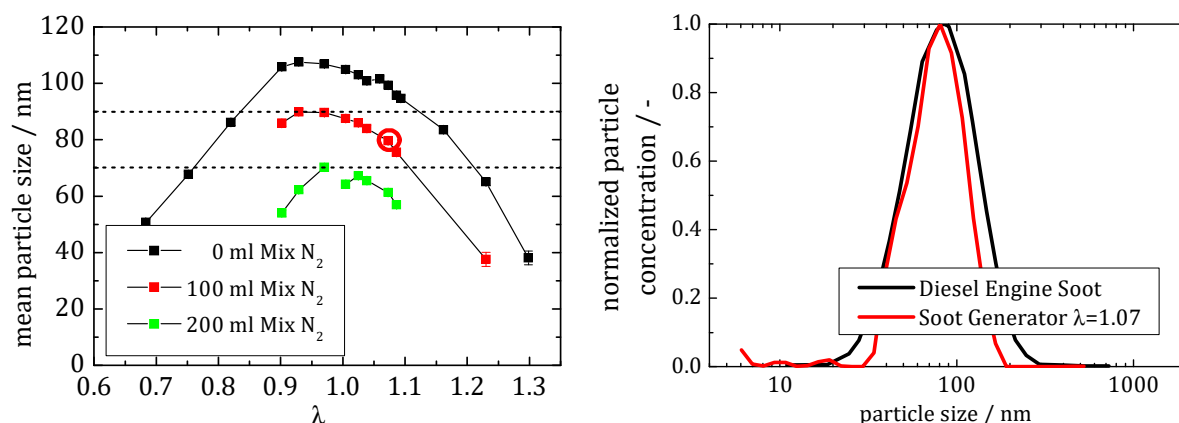


Fig. 28 Left: Mean particle size is a function of the air-fuel equivalence ratio (λ) for operation points possible with the soot-generator analyzed with an EEPS device. The dotted lines indicate the range of mean particle sizes of diesel engine soot. Right: Normalized particle concentration as a function of the particle size for diesel engine soot [126] (black line) compared to soot from soot-generator (red line) at the operation point indicated on the right with a red circle.

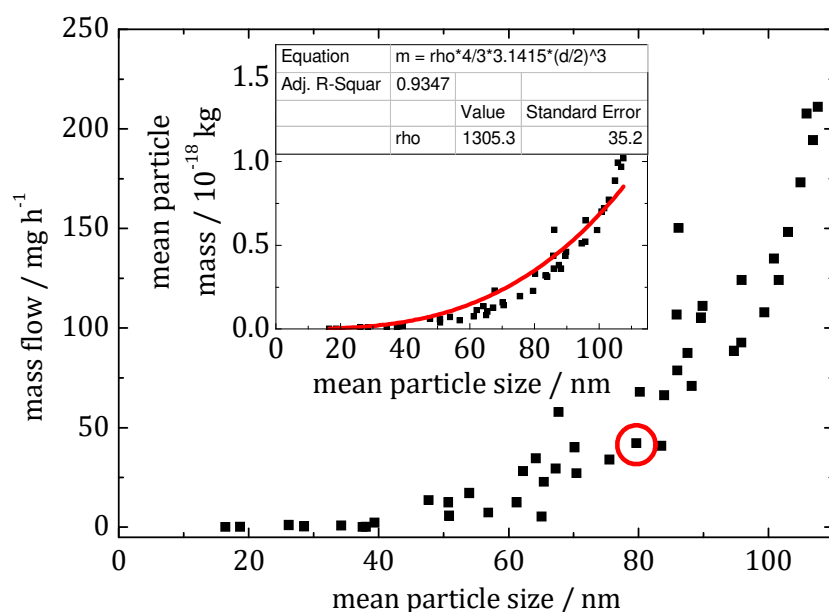


Fig. 29 Soot mass flow as a function of the mean particulate size for the soot-generator OP analyzed by means of an MSS device. The red circle indicates the OP chosen for further investigation. Inset: Average particle mass as a function of the mean particle size. The red line is a cubic fit (function given in the table). The density of the soot particulates is a fit parameter.

5.1.1 NH_3 -Storage Capacity of the Model Soot

To study the interaction of NH_3 with the soot trapped in a DPF (bare filter without zeolite coating, obtained by immersing the SDPF in NaOH-solution), TPD experiments on a DPF have been performed. In **Fig. 30**, the NH_3 outlet concentration of TPD experiments with different soot loadings (soot free, $m_{soot} = 4\ g\ l^{-1}$ and $10\ g\ l^{-1}$) on the bare filter substrate are shown as a function of temperature. It is obvious, that the soot used in this study has the

potential to store NH_3 , which is attributed to acid sites on soot for NH_3 adsorption [143]. The majority of the stored NH_3 is released at temperatures around 780 K. Additionally, the amount of stored and desorbed NH_3 linearly depends on the soot mass deposited. One gram of the studied model-soot could store 22.5 mg NH_3 (see linear fit, **Fig. 30**).

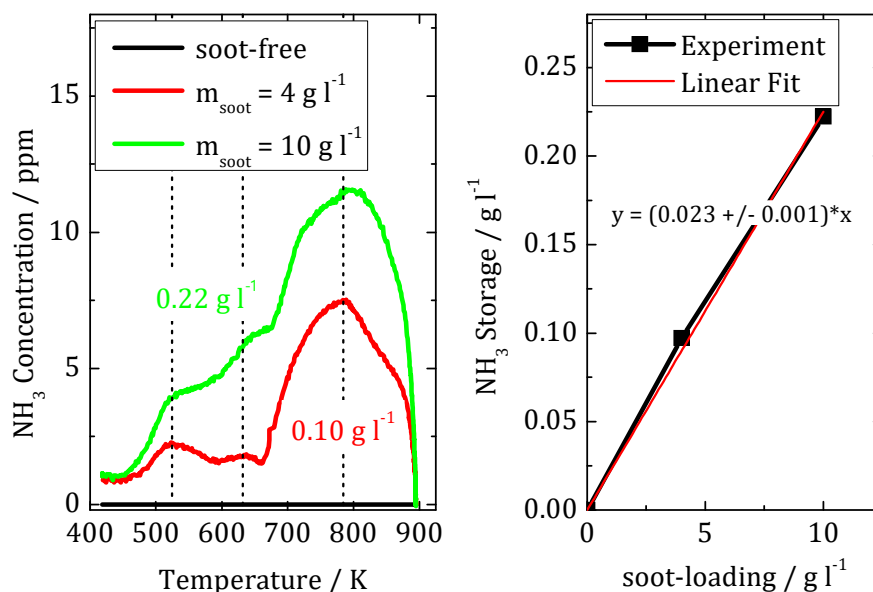


Fig. 30 Left: NH_3 outlet concentration as a function of temperature during TPD on an uncoated DPF (bare filter substrate) sample with no soot (soot free), $m_{\text{soot}} = 4 \text{ g l}^{-1}$ and 10 g l^{-1} . The numbers at the curves indicate the total amount of desorbed NH_3 ($T_{\text{adsorption}} = 423 \text{ K}$, 200 ppm NH_3 in N_2 , GHSV = 40.000 h^{-1}). Right: Calculated NH_3 storage (mass of NH_3 desorbed per filter volume) for the TPD experiments as a function of soot loading in the filter and a linear fit.

5.1.2 Catalytic Properties: NH_3 -SCR

Using a standard SCR experiment and an NO_2 SCR experiment, the catalytic properties in terms of NH_3 De NO_x of the model soot has been evaluated. The sample under study was a bare filter substrate loaded with $m_{\text{soot}} = 10 \text{ g l}^{-1}$. For the standard SCR (**Fig. 31**, left), no NO_x reduction was observed. As stated out by Mehring *et al.* [158], NO_2 is essential for the SCR activity of soot as the catalyst. On the contrary, the NO_2 SCR experiment showed good De NO_x performance of up to 37 % NO_x conversion (**Fig. 31**, right). Without NH_3 dosing (time-on-stream from 0 min to 10 min) about 100 ppm of the incoming NO_2 is reduced to NO , which is due to the soot oxidation at a temperature of 523 K (CO and CO_2 formation observed, not shown here). The stoichiometric ratio $\alpha = \frac{\text{NH}_{3,\text{in}} - \text{NH}_{3,\text{out}}}{\text{NO}_{x,\text{in}} - \text{NO}_{x,\text{out}}}$ was determined to

be 1.25, indicating an overlap of fast SCR ($\alpha=1$) and NO_2 SCR ($\alpha = 4/3$) reaction. The same result was found by Mehring *et al.* [158], who gave a mechanistic explanation for the NO_x

reduction over diesel soot. For the NO₂ SCR experiment up to 6 ppm N₂O formation was observed, indicating an incomplete NO_x-to-N₂ conversion with an N₂O selectivity of 4 %.

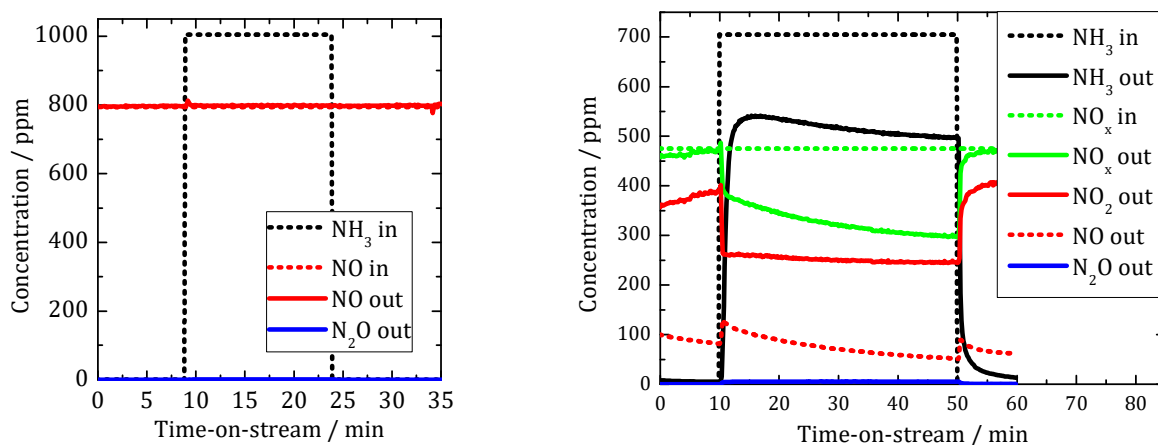


Fig. 31 SCR experiments on bare filter substrates loaded with 10 g l⁻¹. Left: Concentration as a function of the time-on-stream for a stationary standard SCR experiment at 523 K (800 ppm NO permanently dosed, 1000 ppm NH₃ partially dosed). Right: Concentration as a function of the time-on-stream for a stationary NO₂ SCR experiment at 523 K (480 ppm NO₂ permanently dosed, 700 ppm NH₃ partially dosed). Both experiments were performed at GHSV of 40.000 h⁻¹ with 10 vol.-% O₂ in N₂ as feed gas.

5.1.3 Gas Diffusion through a Soot Layer

The effective self-diffusivity D_{eff} of NH₃ probe molecules within the soot layer inside a soot loaded SDPF sample has been studied using PFG-NMR technique. Thereby, the signal intensities of the ¹H free induction decay was measured. It reflects the total amount of protons of the NH₃ molecules in the sample. D_{eff} is obtained by analysis of the spin-echo diffusion attenuations S . The latter followed an exponential dependence on the square gradient intensities q , as given by

$$S(q, t_d) \sim \exp(-Dq^2 t_d) \quad (5.1)$$

where t_d is the diffusion time (or observation time) and $q = \gamma g \delta$ with the gyromagnetic ratio γ , the gradient pulse amplitude g and duration δ . The measurements on a soot loaded SDPF sample ($m_{\text{soot}} = 4 \text{ g l}^{-1}$) have been performed with diffusion times of $t_d = 5 \text{ ms}$, 10 ms and 20 ms of the 13-interval pulse sequence. The experimental data is given in **Fig. 32**. For each t_d , the spin-echo attenuation shows a monoexponential behavior, *i.e.* the diffusion can be described by single effective diffusivity. Thus, a value of $D_{\text{eff}} = (2.5 \pm 0.3) \cdot 10^{-9} \text{ m}^2 \text{ s}^{-1}$ was obtained. Any dependence on the observation time has not been

found. The coincidence of the slopes for different diffusion times reflects the normal (unrestricted) diffusion within the soot layer.

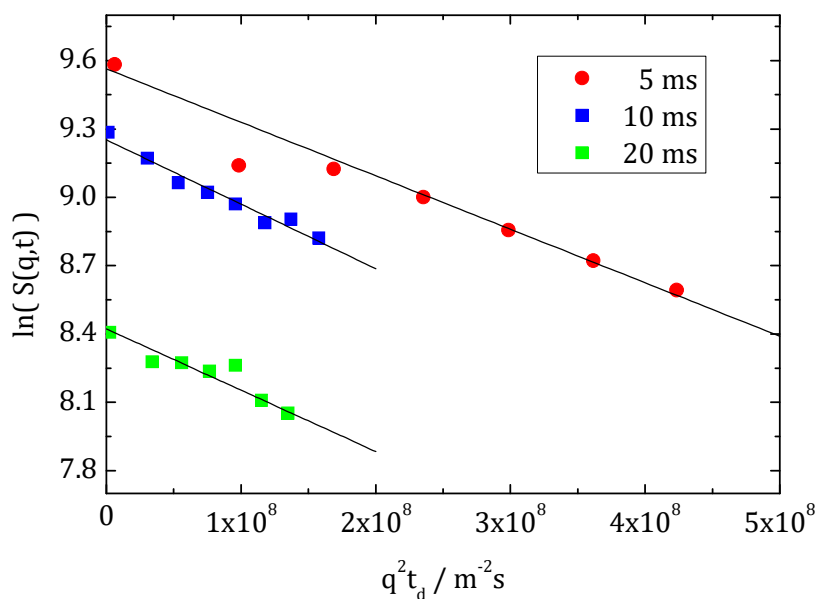


Fig. 32 Spin-echo diffusion attenuations for NH_3 in soot within an SDPF as a function of the square gradient intensities q for diffusion times of 5 ms (circles), 10 ms (squares) and 20 ms (triangles). The solid lines show the linear fits with a slope corresponding to $D_{\text{eff}} = (2.5 \pm 0.3) \cdot 10^{-9} \text{ m}^2 \text{ s}^{-1}$.

As opposed to the soot loaded SDPF sample, the NH_3 stored in zeolite in the soot free SDPF sample shows no contribution to the observed PFG-NMR signal. Thus, the resulting D_{eff} is assumed to originate purely from the diffusion process of the NH_3 probe molecules within the highly porous soot layer.

NH_3 molecules in the system under study exist in the adsorbed (on surface) and in the gaseous phase. Both are in equilibrium with each other. The effective diffusivity in this case can be estimated using

$$D_{\text{eff}} = p_s D_s + p_g D_g \quad (5.2)$$

where D_s is the surface diffusivity and D_g the diffusivity of the gaseous phase in the pores [159]. The coefficients p_s and p_g are the respective relative weights.

The diffusion on a heterogeneous surface was studied among others by Dvoyashkin *et al.* [160]. For n-heptane in Vycor porous glass and electrochemically etched porous silicon they found an increase in diffusivity with increasing surface coverage c . The porous soot (compare **Fig. 60**, Appendix) also has a highly heterogeneous surface. At low NH_3 gas concentration most molecules are trapped on the surface and the contribution from the

gas phase to the molecular transport is relatively low due to notably low p_g . Thus, the observed diffusion coefficient is mostly determined by transport in the adsorbed phase.

For the model gas investigation described in chapter 3.4.2, the NH_3 adsorption at concentrations of 200 ppm (partial pressure of 20 Pa) or 1000 ppm (partial pressure of 100 Pa) at temperature of 423 K was studied. Within this work we assume the self-diffusion observed by PFG-NMR to be the governing process limiting the mass transfer even for the transport regime (Fick's first law implemented in the model). A fit of the filter wall model, presented in chapter 5.3.3, to the model gas experimental data yielded an effective diffusivity of $D_{\text{eff}} = 1.9 \cdot 10^{-10} \text{ m}^2 \text{ s}^{-1}$ for the gas diffusion through the soot. For the low NH_3 concentrations applied during model gas experiments, adsorption of NH_3 at the surface is very likely resulting in a low surface coverage. Thus, the effective diffusion process is limited by surface diffusion ($p_s D_s$) [160].

For PFG-NMR measurement performed within this work, the soot loaded SDPF was saturated with NH_3 at 10^5 Pa . Hence, the contribution of the gas phase to the observed effective diffusivity should be considerably higher. In the PFG-NMR experiment on the soot loaded SDPF sample an effective diffusivity of $D_{\text{eff}} = 2.5 \cdot 10^{-9} \text{ m}^2 \text{ s}^{-1}$ at 298 K was observed. As reported by Valiullin *et al.* [159], D_g can be approximated by the Knudsen diffusion mechanism. Gas phase diffusion ($p_g D_g$) is dominating the diffusion process during PFG-NMR measurement at this level of NH_3 partial pressure. Thus, the value found by PFG-NMR can be considered as the upper limit for the effective diffusivity of NH_3 within soot at given conditions.

5.2 SDPF Sample

In the following chapter the NH_3 storage behavior as well as the activity in SCR-DeNO_x for standard SCR of soot free and soot loaded samples of SDPF1 is investigated. The SCR results are compared to those of SDPF2, having a different pore geometry (compare **Tab. 3.1** and **Fig. 62**, Appendix).

5.2.1 NH_3 Storage Capacity

In the following subchapter the results on the NH_3 storage capacity of SDPF1 (see **Tab. 3.1**) are presented. Prior to a comprehensive study on the NH_3 storage behavior of soot free and soot loaded SDPF samples, the influence of H_2O in the feed gas for the NH_3 adsorption/desorption experiments has been evaluated. In **Fig. 33** two

adsorption/desorption experiments are shown, the black curve with no H₂O in the feed gas, the red curve with 5 vol.-% H₂O dosed together with the 1000 ppm NH₃ in N₂. Applying eq. (3.3), the amounts of adsorbed NH₃ were calculated and are given in the inset: 2.51 g l⁻¹ (without water) and 2.34 g l⁻¹ (with water). As indicated by the arrows, a slightly decreased amount of stored NH₃ was found for the experiment when additionally, H₂O was dosed. This could be explained by the co-adsorption of NH₃ and H₂O, competing for the same Cu-zeolitic storage sites [50]. As the effect is small (loss of 7 wt.-% under the conditions studied here) and to be not affected by side reactions of H₂O to the soot, in the following study on the NH₃ storage capacity it has been renounced on the H₂O dosing. In a preliminary experiment (not shown here) it could be proven, that the used model gas apparatus allowed very high reproducibility. Two adsorption/desorption experiments performed in a row under the same conditions yielded a deviation of maximum 1.5 wt.-% in the amount of stored NH₃.

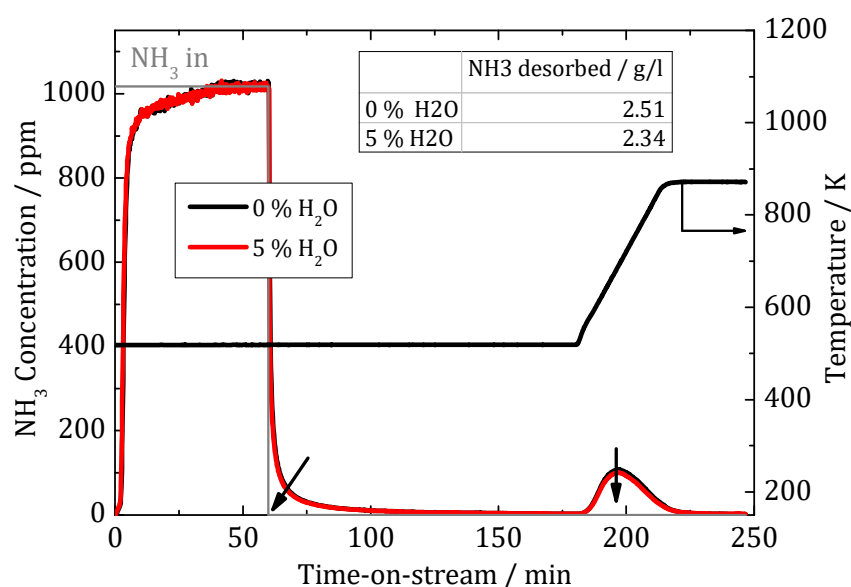


Fig. 33 NH₃ concentration as a function of time-on-stream during NH₃ adsorption and desorption experiments of a soot free sample. First, 1000 ppm NH₃ (black line) or 1000 ppm NH₃ together with 5 vol.-% H₂O (red line) were dosed for 60 min into the N₂ feed at 523 K followed by N₂ flushing for 120 min. Finally, the temperature was raised with 10 K min⁻¹ up to 873 K (GHSV = 40.000 h⁻¹). The arrows indicate the changes in the concentration profile due to water dosing. The inset table gives the amount of NH₃ desorbed during flushing and temperature raise.

The mechanism of NH₃ storage in the Cu-zeolite (of soot free SDPF samples) has been studied by means of NH₃ adsorption/desorption experiments at different adsorption temperatures (T_{ads} = 423 K, 523 K and 623 K) as well as for different NH₃ inlet concentration (200 ppm, 1000 ppm and 3000 ppm). The experimental results for the

TPDs with 200 ppm NH_3 in the feed gas are given in **Fig. 34** (left). The adsorption/desorption of NH_3 shows the typical behavior for multiple site adsorption as widely discussed in literature on kinetic modelling [50,51,68,135]. The higher the adsorption temperature, the more the rate of desorption exceeds the rate of adsorption. Thus, on the energetic landscape the amount of accessible zeolitic storage sites for NH_3 molecules with a bonding energy above the thermal energy decreases with increasing temperature. This could be observed by an NH_3 breakthrough shifting towards earlier time-on-stream in the adsorption (part a). During desorption (temperature ramp) less NH_3 is released when adsorbed at higher temperature. The picture on the right gives the appropriate TPD profiles. For the sample with adsorption at 423 K a NH_3 desorption profile with two maxima is observed, representing the energy distribution of the bonding sites. The weaker bonding sites show a maximum desorption at 550 K while the stronger bonding sites desorb most at 695 K. For the experiment with adsorption at 523 K only the stronger adsorption sites were accessible. The TPD with adsorption at 623 K shows maximum desorption at 770 K. Thus, only the high energy edge of the strong sites contribute.

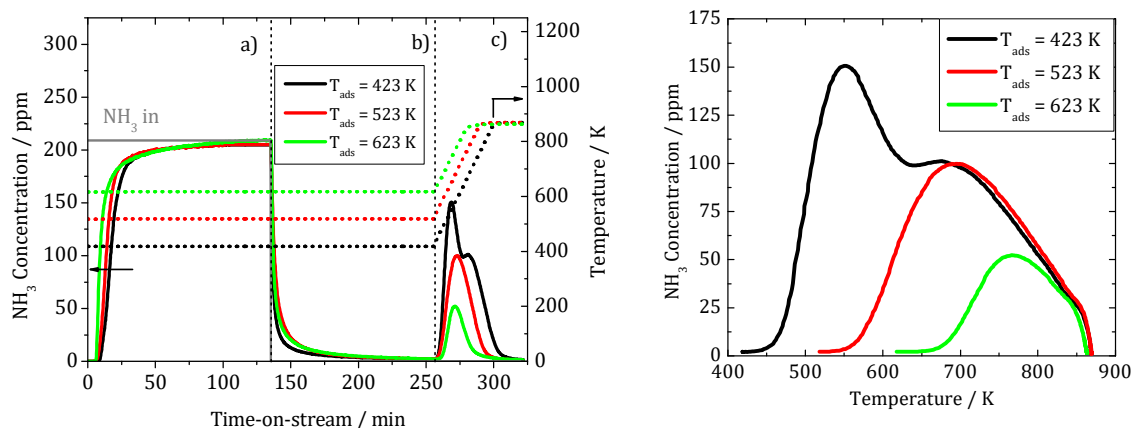


Fig. 34 Left: NH_3 concentration as a function of time-on-stream during NH_3 adsorption and desorption experiments of a soot free sample. At a) 200 ppm NH_3 was dosed into the N_2 feed at 423 K, 523 K and 623 K respectively, b) N_2 flushing and c) feed gas temperature raise with 10 K min^{-1} up to 873 K ($\text{GHSV} = 40.000 \text{ h}^{-1}$). Right: NH_3 concentration as a function of the temperature evaluated from desorption temperature ramp (part c, left picture).

With the aim of a theoretical description of the temperature dependence of the NH_3 storage, the Dubinin-Astakhov (D-A) equation was applied. D-A is a physical model for microporous adsorption [161]. The theory is based on the earlier adsorption potential theory of Polanyi and Dubinin [162,163], suggesting that the governing adsorption process is the filling of micropore volume. With a diameter of 0.26 nm the NH_3 molecule

is able to fill the three-dimensional channel system of the ZSM-5 zeolite, with a free channel diameter of $0.54 \text{ nm} \times 0.56 \text{ nm}$ [164]. The potential theory of Polanyi for multilayer adsorption considers that the adsorption forces act at distances greatly exceeding the dimensions of a single molecule, so that they are not shielded by the first monolayer of the adsorbate. The D-A equation involves the adsorption potential A as given in eqn. (5.3). Thereby, $q(p)$ represents the mass adsorbed at equilibrium pressure p , q_0 represents the maximum mass of adsorbed species, E_{DA} gives the adsorption energy and n the heterogeneity parameter (or Astakhov exponent). The vapor pressure p_0 is taken as the reference state pressure. For NH_3 at temperatures above 343 K, the vapor pressure is calculated using eqn. (5.4) according to [165].

$$q(p) = q_0 \cdot \exp \left[- \left(\frac{A}{E_{DA}} \right)^n \right] = q_0 \cdot \exp \left[- \left(\frac{RT}{E_{DA}} \cdot \ln \left(\frac{p_0}{p} \right) \right)^n \right] \quad (5.3)$$

$$p_{0,\text{NH}_3}(T) = 8.8138 \cdot 10^6 \cdot e^{-\frac{2706.65 \text{ K}}{T}} \text{ kPa} \quad (5.4)$$

Dubinin-Astakhov isotherms have been extensively used for the adsorption of gases and vapors [163,166,167], in lesser extent also for the adsorption of organic solutes from aqueous solution [161,168]. The Dubinin-Radushkevich (D-R) equation (heterogeneity parameter $n=2$ in eqn. (5.3)) represents a special case of the D-A equation. It applies only to solids with uniform micropores.

The NH_3 inlet concentration during the NH_3 adsorption/desorption experiment could be translated into an equilibrium pressure by means of Dalton's partial pressure law. Using eq. (3.3), the stored amount of NH_3 for each experimentally studied combination of adsorption temperature and inlet concentration was evaluated and is depicted in **Fig. 35**. The higher the NH_3 partial pressure, the more NH_3 is stored for each temperature of adsorption. For partial pressures larger than 0.05 kPa the stored amount of NH_3 saturates. The experimental data could be nicely fitted using the D-A adsorption equation. Although NH_3 molecules are known to be chemically bonded to acid sites of the ZSM-5 zeolite [68], the general physical theory of micropore filling also describes the storage of NH_3 molecules in zeolite. The fit yields an adsorption energy E_{DA} of 64.4 kJ mol^{-1} and a heterogeneity parameter of $n=1.65$. The Astakhov exponent less than 2 indicates a heterogeneous porosity of the ZSM-5 [166]. This could be due to Cu ions partially incorporated in the zeolite network, locally changing its pore size.

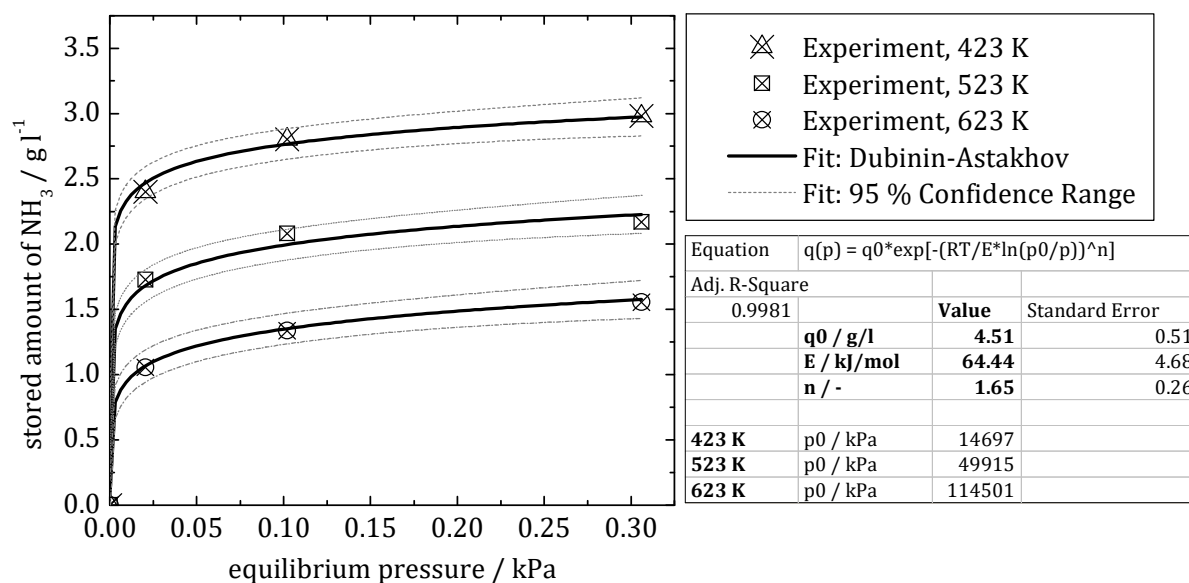


Fig. 35 Left: Stored amount of NH_3 as a function of the equilibrium pressure. The points are experimental data, evaluated from the desorption part (compare part b and part c in **Fig. 34**, left) of NH_3 adsorption/desorption experiments performed at adsorption temperatures of 423 K, 523 K or 623 K while 200 ppm, 1000 ppm or 3000 ppm NH_3 was dosed in N_2 during adsorption (GHSV = 40.000 h^{-1}). The solid black lines are the result of a fit of the Dubinin-Astakhov equation (5.3) to the experimental data. The grey lines represent a 95 % confidence interval to the fitted lines. Right: The table gives the saturation vapor pressure for each adsorption temperature as well as the fit parameters V_0 , E_{DA} and n including their standard error.

5.2.1.1 Hydrothermal Ageing

The evolution of the NH_3 storage capacity under thermal stress is a critical issue for the SCR zeolite in vehicle application. Soot removal by regeneration leads to temperatures up to 1100 K in the SDPF. In **Fig. 36** (left) the NH_3 TPD profiles of a fresh SDPF sample is compared to HT (hydrothermally) aged samples. An ageing of 18 h results in an extreme drop in the NH_3 storage (amount of desorbed NH_3), whereas an additional HT ageing of 21 h has nearly no further influence on the desorption signal. The appropriate loss in NH_3 storage as a function of HT ageing time is given on the right. Most of the loss is already achieved at the first 20 h of ageing under the applied conditions. Hence, the loss in NH_3 storage saturates. A maximum loss of 16 % was observed. The effect of HT ageing of Cu-zeolites (ZSM-5) as SCR-catalysts was already reported in [74,75]. The loss in NH_3 storage was explained by the destruction of zeolite structure (decreased surface area and pore volume) and the agglomeration of active Cu phase.

Studying the NH_3 TPD profiles of HT aged SDPF samples in more detail, it could be revealed that HT ageing leads to a loss of the strong acid storage side. The appropriate graph is given in **Fig. 37**. Furthermore, the weak storage sites slightly increased their

amount of bound NH_3 when HT aged. Similar results were observed by Wilken *et al.* [57]. According to the literature, the changes in the NH_3 binding to the acid sites are the result of thermally induced structural changes of the zeolite.

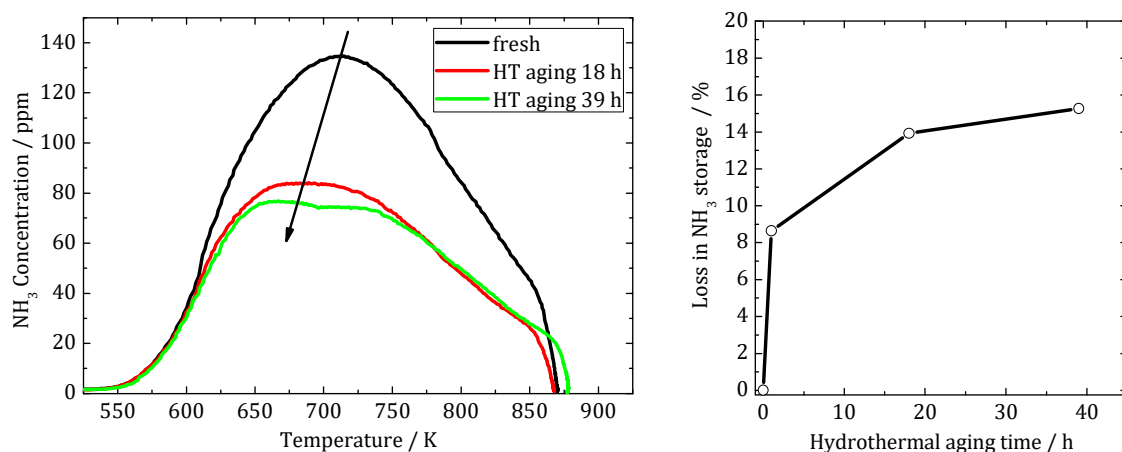


Fig. 36 Left: Desorbed NH_3 concentration as a function of the temperature for TPD experiments on SDPF samples with varying level of ageing. The appropriate adsorption/desorption experiments were performed at $T_{\text{ads}} = 523$ K while dosing 1000 ppm NH_3 in N_2 at space velocity of 40.000 h^{-1} (compare **Fig. 34**, left). The arrow indicates the shift of the desorption maxima. The hydrothermal (HT) ageing was performed in a furnace at 973 K under air flow. Right: Loss in NH_3 storage as a function of the HT ageing time.

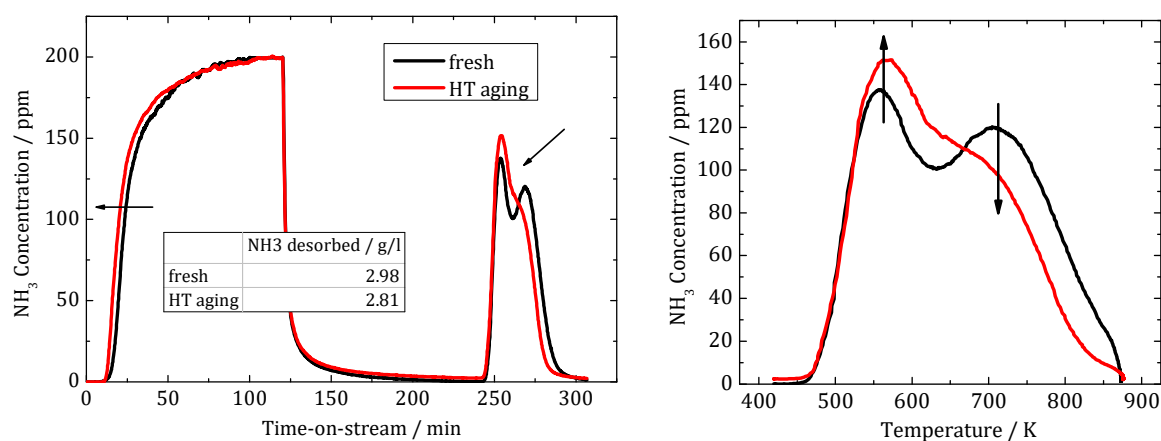


Fig. 37 Left: NH_3 concentration as a function of the time-on-stream for adsorption/desorption experiments performed on fresh (black) and hydrothermally aged (red) SDPF sample. (measurement conditions as in **Fig. 34**, left). The arrows indicate changes in the adsorption and desorption behavior. Right: NH_3 concentration as a function of the temperature evaluated from desorption temperature ramp. The arrows indicate a decreased storage on the strong acid sites and a slight increase in the NH_3 binding on the weaker bonding sites.

5.2.1.2 Soot Loading

The influence of soot on the NH_3 storage behavior of SDPF samples has been studied by means of TPD experiments at different adsorption temperatures with different soot loadings. In **Fig. 38**, the NH_3 concentration profile for a soot free and a soot loaded ($m_{\text{soot}} = 4 \text{ g l}^{-1}$) SDPF sample from a TPD experiment is shown. The characteristics of the adsorption/desorption profile of the soot free sample has been discussed already in chapter 5.2.1. The sample with $m_{\text{soot}} = 4 \text{ g l}^{-1}$, however, exhibits a completely different NH_3 adsorption profile. Already at the start of the NH_3 dosing, NH_3 slip is observed. The adsorption-breakthrough curve is flattened, indicating a decreased rate of NH_3 adsorption in the early stages of the experiment. This features were also observed by Mihai *et al.* [142] or Millo *et al.* [169], but both authors could not give an explanation. The inflection point, notified by the arrow in **Fig. 38**, is typical for all the NH_3 adsorption/desorption experiments on soot loaded SDPF samples performed in this study. During the heat ramp, the desorbed NH_3 concentration shows two maxima (at 572 K and at 720 K) indicating basically two kinds of different adsorption sites in the Cu-zeolite. The results reveal a slightly increased amount of NH_3 desorbed during the temperature ramp for the soot loaded case compared to the soot free case (values given in **Fig. 39**). The same reproducible adsorption profile is also observed at higher temperatures and with different NH_3 concentrations in feed gas (compare **Fig. 63**, in Appendix). For adsorption at 523 K the TPD profile shows only one maximum at 720 K. Desorption from the weaker storage sites are no longer observed. As an elevated adsorption temperature results in a decreased NH_3 storage, the soot-induced change in the shape of the adsorption-curve occurs at an earlier time-on-stream compared to the NH_3 adsorption at 423 K. Qualitatively, the breakthrough is affected in the same way, resulting in a flattened regime with an inflection point. Hence, the adsorption-temperature, implying the amount of accessible storage sites, has no influence on the shape of the adsorption curve. This gives hints to a non-chemical explanation for the changed NH_3 breakthrough during adsorption.

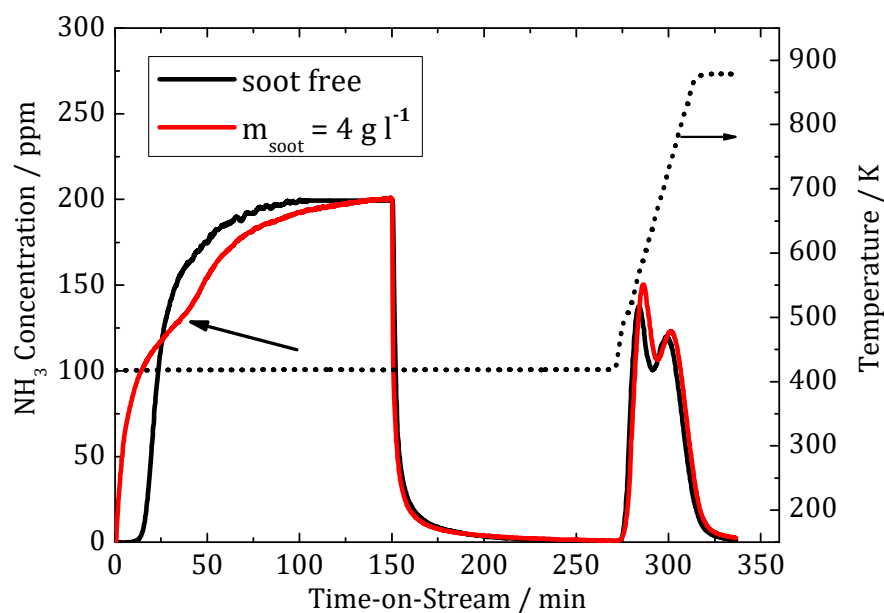


Fig. 38 NH_3 concentration as a function of time-on-stream during NH_3 adsorption and desorption experiments of a soot free and a soot loaded ($m_{\text{soot}} = 4 \text{ g l}^{-1}$) sample. At a) 200 ppm NH_3 was dosed into the N_2 feed at 423 K, b) N_2 flushing and c) feed gas temperature raise with 10 K min^{-1} (GHSV = 40.000 h^{-1}).

The knowledge of the NH_3 storage behavior for the soot loaded SDPF system is very important for automotive applications. Therefore, NH_3 adsorption/desorption experiments were performed on SDPF samples with different soot loadings at adsorption temperatures of 423 K and 523 K, respectively. The NH_3 outlet concentrations as a function of the temperature are shown in **Fig. 39** (left and middle). The right graph gives a bar chart of the volume-based mass of stored NH_3 . For both soot loading cases (soot free and $m_{\text{soot}} = 4 \text{ g l}^{-1}$) the sample that adsorbed at lower temperature reveals the higher NH_3 storage, which is due to the well known adsorption behavior of Cu-ZSM-5 zeolites described in **Fig. 35** or in [50,51]. The temperature dependence of the NH_3 storage of the zeolite has been proven to follow the Dubinin-Astakhov adsorption isotherms (chapter 5.2.1). Additional soot trapped in the filter even leads to a slightly elevated NH_3 storage capacity. These results are in very good agreement with those presented by Schrade *et al.* [135] (0.1 g l^{-1} to 0.2 g l^{-1} more NH_3 stored, if soot is present), Mihai *et al.* [142] ($69 \mu\text{mol}$ more NH_3 stored, if soot is present in the SDPF sample; unfortunately no sample volume or weight given), Tronconi *et al.* [138] ($28 \mu\text{mol g}_{\text{cat}}^{-1}$ more NH_3 stored, if soot is present) and Millo *et al.* [169] (only mentioning a slight increase if soot is present but no numbers are given). They mentioned also an increased NH_3 storage of soot loaded SDPFs compared

to the non-loaded case and soot loaded bare DPFs revealed a slight storage capacity. Nevertheless, the effect of an increase in NH_3 storage, comparing a soot loaded SDPF sample to a soot free SDPF sample, is controversially discussed in literature. Tan *et al.* [141] found a decrease of the NH_3 storage capacity, when soot is trapped inside the filter, while an explanation for this observation was not provided. According to the storage behavior of pure soot (**Fig. 30**), we suggest the overall NH_3 storage of a soot loaded SDPF sample to be the sum of the stored amounts within the zeolite and the soot. This implies that although there is soot trapped inside the porous filter wall, located on top of the washcoat, all the zeolitic active sites are physically accessible for NH_3 molecules on a large time scale. Beside the increased NH_3 -storage, the NH_3 -desorption signal of soot loaded samples slightly shifts to higher desorption temperature (also found in [138,142]), which is due to the release of NH_3 bound to the soot with a maximum desorption at 780 K (see **Fig. 30**).

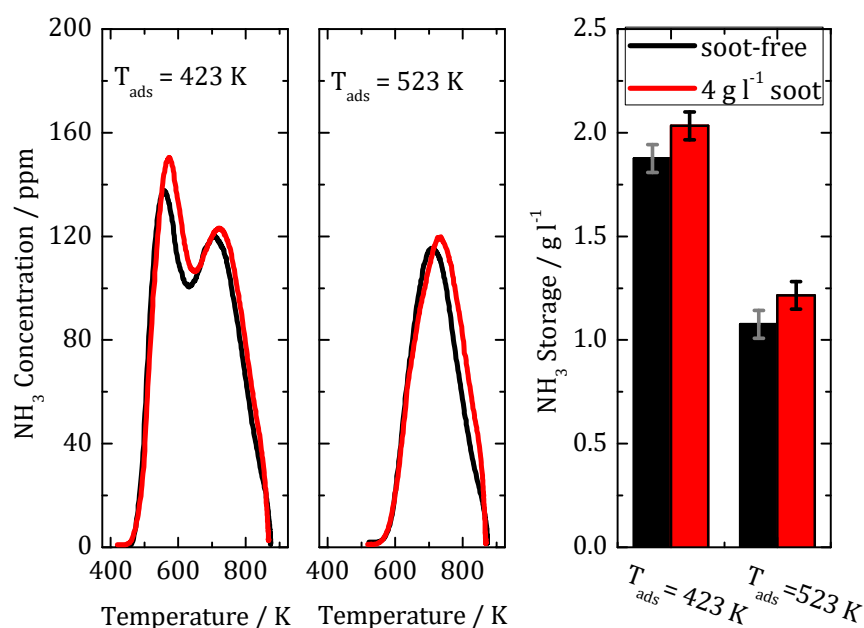


Fig. 39 NH_3 outlet concentration as a function of temperature during TPD on SDPF sample without soot (soot free) and with soot ($m_{\text{soot}} = 4 \text{ g l}^{-1}$ and 10 g l^{-1}). Left: $T_{\text{ads}} = 423 \text{ K}$, 200 ppm NH_3 in N_2 , Middle: $T_{\text{ads}} = 523 \text{ K}$, 1000 ppm NH_3 in N_2 , both at GHSV = 40.000 h^{-1} . Right: Calculated NH_3 storage (integrated curve area in gram NH_3 per filter volume) for the TPD experiments depicted in the left and in the middle part. Error bars ($\pm 0.075 \text{ g l}^{-1}$) are also given, representing an uncertainty of 2 ppm within the concentration measurement.

To study the NH_3 uptake in more detail, NH_3 adsorption/desorption experiments with different times of NH_3 dosing (10 min, 20 min and 150 min) have been investigated. The TPD results are given in **Fig. 40**. The adsorption signal (left) reveals a decreased rate of adsorption for the soot loaded sample. The appropriate mass of chemisorbed NH_3 as a function of time-on-stream during adsorption is depicted in **Fig. 41**. Hence, the adsorption rate is limited by the soot, for incomplete adsorption (NH_3 dosing duration of 10 min and 20 min) the $m_{\text{soot}} = 4 \text{ g l}^{-1}$ sample reveals a smaller amount of NH_3 stored compared to the soot free case. NH_3 reaching the zeolite is initially bound to the stronger adsorption sites with maximum desorption at 700 K for the soot loaded sample. Only when the strong sites are nearly saturated (NH_3 dosing duration > 10 min) the weak adsorption sites are filled. For the soot free sample both binding sites seem to fill up more simultaneously. This feature strongly suggests a reduced rate of NH_3 reaching at the zeolite for the soot loaded sample compared to the soot free sample. The more time the NH_3 molecules have for binding, the more likely is their adsorption at first stage at the stronger binding sites. For complete adsorption (inlet concentration equals outlet concentration) the decreased adsorption rate for the soot loaded sample is no longer an issue regarding the stored amount of NH_3 . Thus, the soot loaded sample ends up with a slightly higher NH_3 amount stored, which could be attributed to the contribution of the soot itself to the storage.

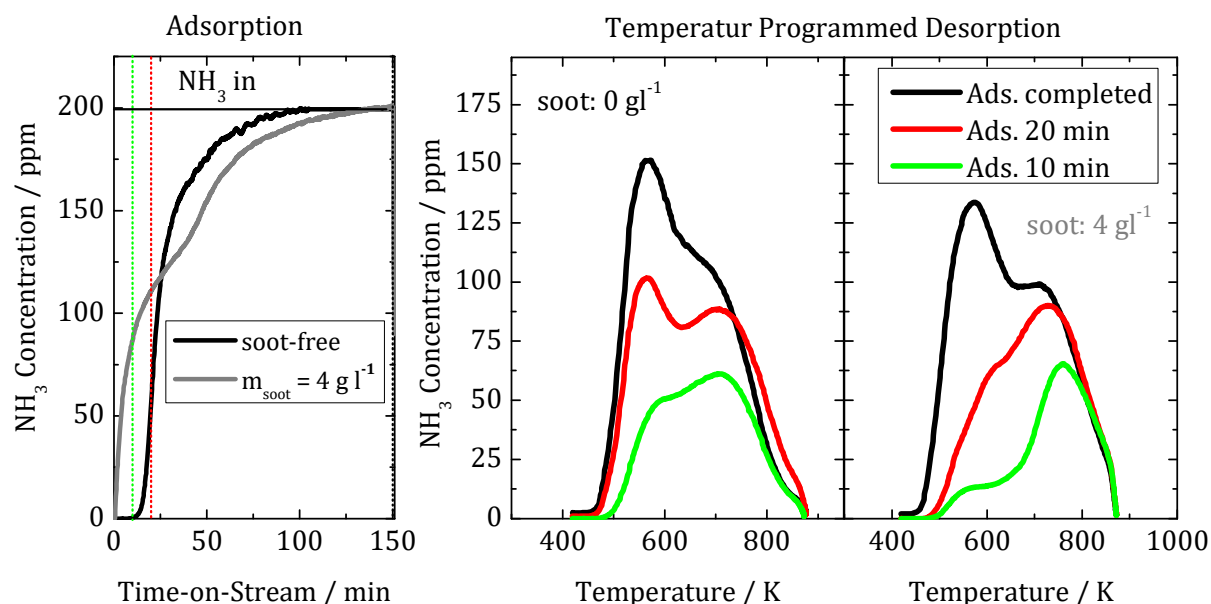


Fig. 40 NH_3 adsorption/desorption experiments for a soot free and a soot loaded $m_{\text{soot}} = 4 \text{ g l}^{-1}$ sample with different times of NH_3 dosing ($T_{\text{ads}} = 423 \text{ K}$, 200 ppm NH_3 in N_2 at GHSV = 40.000 h^{-1}). Left: NH_3 outlet concentration as a function of time-on-stream for complete adsorption (150 min NH_3 dosing until outlet concentrations equal inlet concentration). The green and the red line indicate shorter NH_3 dosing durations of 10 min and 20 min respectively. Middle and right: NH_3

outlet concentration as a function of temperature during temperature programmed desorption for adsorption/desorption experiments with NH_3 dosing durations of 10 min (green), 20 min (red) and for complete adsorption (150 min, black). Results of the soot free sample are given in the middle, results of the $m_{\text{soot}} = 4 \text{ g l}^{-1}$ sample are given in the right.

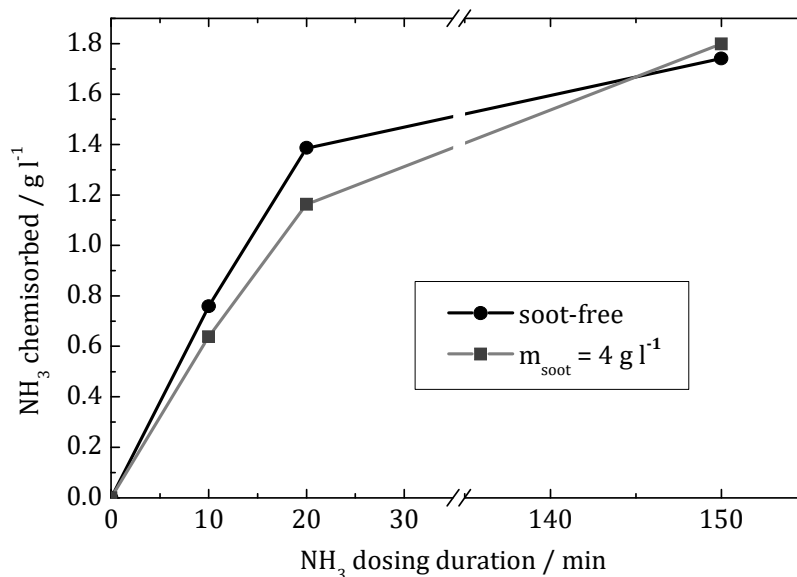


Fig. 41 Amount of chemisorbed NH_3 as a function of the NH_3 dosing duration for a soot free sample and a $m_{\text{soot}} = 4 \text{ g l}^{-1}$ sample. The data is the result of integrating the curve area of **Fig. 40** (middle and right) using eq. (3.3).

5.2.2 Activity of SCR-DeNO_x

The amount of NH_3 stored in zeolites containing transition metals like Cu- and vanadium-impregnated tungsten/titanium mixed oxide catalysts (VWT catalysts) has consistently been reported in literature to be one of the key parameters defining the NO_x conversion [170,171]. The NH_3 adsorption/desorption experiments presented above support the strong influence of the soot deposited in an SDPF on the NH_3 adsorption kinetics. Therefore, in-wall soot is expected to also have an influence on the SCR activity of SDPFs.

In the following subchapter the influence of the soot loading on NO conversion in standard SCR experiments is presented for both SCR coated particulate filters under investigation (see **Tab. 3.1**). As revealed by Hg-intrusion (see **Fig. 62**, Appendix), the pore geometry of both SDPF samples strongly deviates. Thereby, SDPF1 is characterized by a larger porosity of the filter wall of 48.0 % (compared to 41.2 % for SDPF2), a higher mean pore size of $26.6 \mu\text{m}$ (compared to $17.0 \mu\text{m}$ for SDPF2) and a slightly increased pore volume $348 \text{ cm}^3 \text{ g}^{-1}$ (compared to $319 \text{ cm}^3 \text{ g}^{-1}$ for SDPF2). The appropriate backpressure measurements during soot loading are given in chapter 5.3.1. The amount of soot trapped by deep bed filtration inside the porous filter wall ($m_{\text{soot,wall}}$) could be evaluated from

these curves. Thereby, the porous wall of SDPF1 trapped $m_{\text{soot,wall}} = 1 \text{ g l}^{-1}$, while SDPF2 has much less filtration capacity for in-wall soot of $m_{\text{soot,wall}} = 0.36 \text{ g l}^{-1}$.

As pointed out by Tronconi *et al.* [139] and Mehring *et al.* [158], there is no chemical reaction of the standard SCR gas mixture (NO , NH_3 , H_2O and O_2 , no NO_2) with the soot as long as the temperature is sufficiently low to prevent O_2 -based soot-combustion. According to [90], soot oxidation by O_2 becomes significant for temperatures above 673 K. Thus, soot within this study should be not affected during the standard SCR experiments. Soot oxidation by NO_2 already takes place at temperatures above 523 K. Since an influence of the soot loading on the NO_x conversion resulting from NO_2 assisted soot oxidation might be difficult to distinguish from that of diffusive mass transport, additional NO_2 in the reaction gas mixture was not attempted in the present study. That is why standard SCR reaction was chosen here to study the physical influence of soot on the NO conversion. The formation of NO_2 by NO oxidation over the SDPFs under study could be proven to be negligible. **Fig. 42** (left) shows the results of the SCR experiment on a soot free SDPF1 sample vs. the same sample loaded with $m_{\text{soot}} = 1 \text{ g l}^{-1}$. Consequently, for the standard SCR experiment the soot loading of 1 g l^{-1} was chosen to make sure there is only soot deposited inside the porous wall and not on top as a cake layer (see chapter 5.3.1). The experiment shows a decrease in NO conversion for soot loaded sample ($m_{\text{soot}} = 1 \text{ g l}^{-1}$ in-wall soot) compared to the soot free sample up to 20 %. The same extend of NO conversion drop was also reported in [137,138], both using model-soot for their investigation. On the other hand, the same standard SCR experiment performed on SDPF2 (**Fig. 42**, right) revealed a decrease in NO conversion of only up to 7 % for the sample loaded with 1 g l^{-1} soot. As known from the backpressure measurement during loading (see chapter 5.3.1) thereby only 0.36 g l^{-1} have been trapped inside the porous filter wall in close vicinity to the chemically active sites. Only a slight loss in NO conversion (up to 5 %), was also reported in [135,136] (both using engine soot).

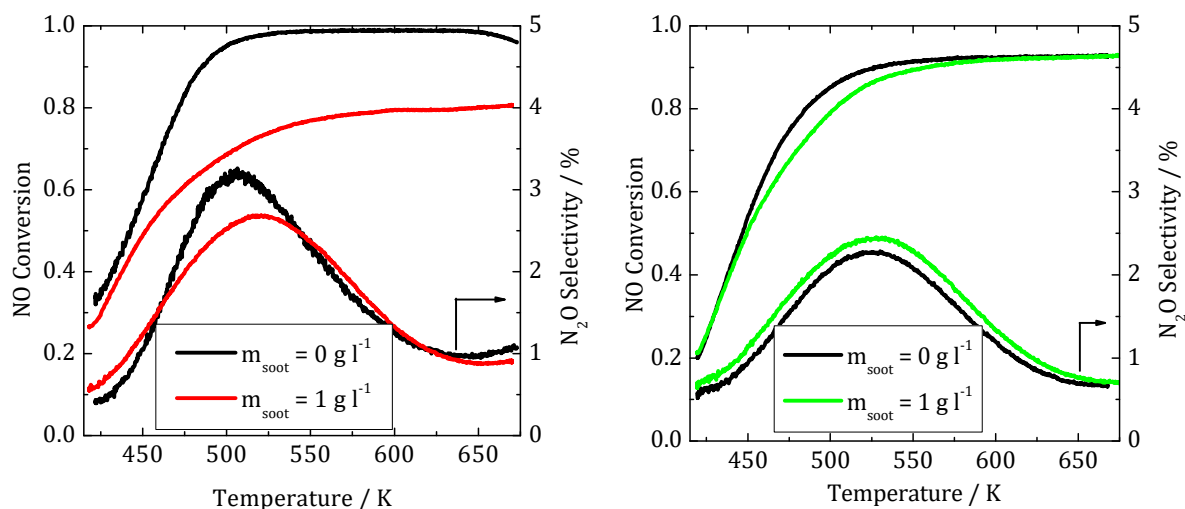


Fig. 42 NO conversion as a function of the temperature (Light-off curves) for a soot free and a soot loaded ($m_{\text{soot}} = 1 \text{ g l}^{-1}$) SDPF sample at $n(\text{NO}_2)/n(\text{NO}_x) = 0$ in an SCR experiment (1000 ppm NH_3 and 800 ppm NO were dosed with 5 vol.-% H_2O and 10 vol.-% O_2 in N_2 while the temperature was ramped linearly from 423 K to 673 K at 2 K min^{-1}). Additionally the N_2O selectivity (belonging to the right ordinate) is plotted. The left picture gives the results of SDPF1, the right picture belongs to SDPF2.

In literature studies, mentioned above, the observed extend of the NO conversion loss as well as the studied soot is reported but no comments are given on the measured backpressure during loading (implying amount of in-wall soot). Thus, based on the literature reports, it is not possible to find the reasons for the deviation in the reported NO conversion losses. The choice of the soot (engine-soot, model-soot, Printex) for studies on soot loaded SDPF may play a role for the resulting NO_x conversion, which is maybe due to differences in the physical (porosity, density, stickiness and thus penetration depths inside the filter wall) or the chemical (NH_3 adsorption [143]) characteristics of the soot that is used. The model soot under study within this work shows higher fraction of EC to OC compared to real diesel soot [107]. Hence, reduced stickiness may leads to deeper penetration depth inside the porous filter wall. Nevertheless, the two filters studied here (SDPF1 and SDPF2) have different amounts of soot trapped inside the porous filter wall but were loaded with the same kind of model soot. This suggests the huge deviation in the soot impact (20 % NO conversion loss and 7 % NO conversion loss, respectively) to have its origin in the amount (and distribution) of the deep bed filtered soot.

As the soot loaded SDPF1 sample only reveals soot inside the porous wall, the origin of the soot-induced change in the catalytic activity has to be attributed to this soot deposits, which could directly interact with the active sites of the zeolite. To address this, some

groups [135,137] argue with the blocking of active sites when the soot inside the wall is closely associated to the Cu-zeolite but without mentioning a chemical explanation. Especially Cavataio *et al.* [137] observed that after exposing the soot loaded sample to 623 K the conversion reached in the non-loaded case could be partially recovered. This finding is explained by the combustion of the volatile organic fraction (VOF) of the soot at low temperatures, which was in close contact to the active sites. Nevertheless, this result could not be reproduced in our study although they were also using a soot-generator based on propane. Unfortunately, they did not mention the operation parameters for their soot-generator. As known from [107], slight changes in the propane to air ratio lead to huge differences in the resulting soot composition (amount of VOF stacking at the elemental carbon core). So, differences in the soot composition are possible. According to [107], the model soot used here, has a high EC ratio of about 95 % and hence nearly no VOC attached to the particles. On the other hand, due to the fact that soot loaded SDPF samples showed an increased storage capacity, the explanation of blocked active sites is not likely. Other researchers [144,145] explain the decreased NO conversion under soot loading by a physical mass transfer phenomenon. The soot trapped inside the porous filter acts as a diffusion barrier for the gas species reaching/leaving the catalyst. They also mentioned the soot in the porous wall to be the main reason for the observed NO conversion drop (cake-layer soot has no influence).

The underlying mechanism of decreasing the NO conversion during SCR-reaction may correspond to the NH₃ adsorption behavior (**Fig. 38**) and thus, the detailed understanding of processes leading to the observed adsorption kinetics may clarify the microscopic phenomena underlying the decrease of the SCR performance in presence of the soot. The appropriate tool for a microscopic study of the phenomena described here is a wall filtration model connected to a chemical model. The model results are presented in chapter 5.3.

Furthermore, the N₂O selectivity for soot free and soot loaded SDPF samples has been studied (see **Fig. 42**). For both samples (SDPF1 and SDPF2) the NO-to-N₂ conversion by standard SCR is very selective. A N₂O selectivity of maximum 3 % has been evaluated. The difference in N₂O selectivity between a soot free and a soot loaded sample was up 0.5 %, which could be attributed to the uncertainty of the concentration measurement for the formed small N₂O concentrations of up to 10 ppm.

5.3 Modelling

5.3.1 Backpressure

During the soot loading procedure of the SDPF samples the backpressure has been utilized as an indicator of the soot loading mode (*i.e.* deep bed or/and cake filtering [114,126]) as well as to estimate the density of soot trapped within the filter. Thus, the backpressure and the soot mass allow to characterize the loading state of the sample, as shown in **Fig. 43**. The transition from the deep bed filtration (part a) to the cake filtration (part b) [98,140] is evident by the change in the slope of the curve, indicated by the vertical line. For SDPF1 it takes place, when $m_{\text{soot,wall}} = 1 \text{ g l}^{-1}$ soot is trapped inside the pores of the filter wall. For SDPF2 the transition in filtration mode is already achieved at a much lower mass of wall trapped soot $m_{\text{soot,wall}} = 0.36 \text{ g l}^{-1}$. The applied soot masses used for our investigations (up to 10 g l^{-1}) correspond to typical situations in a real operation [126]. In general the amount of soot filtered within the filter wall depends on the structural properties of the particulate filter as well as the conditions during soot loading (*e.g.* gas flux and velocity [123]). The influence of the soot loading on the backpressure of the DPF was already discussed and mathematically described in literature [99,125,172]. When the void in the porous wall and especially the surface pores close to the inlet channel fill up, the permeability of the porous wall decreases [126]. Afterwards the cake layer acts as a barrier for the gas flux having a certain permeability. This results in an increased backpressure with elevated soot loading due to the increased thickness of the cake layer. **Fig. 43** shows the measured backpressure (black solid curve) for an SDPF1 sample that is loaded with $m_{\text{soot}} = 7 \text{ g l}^{-1}$ (during loading 1 g l^{-1} in-wall soot as well as 6 g l^{-1} cake-layer soot is deposited). This experiment was used to determine parameters *e.g.* the soot density or the soot mass trapped inside the porous wall for validation of the unit collector model ([126] and chapter 2.3.2). Basically following the backpressure calculation presented in chapter 2.3.2, under usage of a percolation factor of 0.96, the calculated pressure drop (dotted lines in **Fig. 43**) are in good agreement with the experimental data. Thereby, the model implements depth filtered soot within the wall only in close vicinity to the inlet channel (as shown by the blue line in **Fig. 47**, left). As mentioned above, the soot density within the filter is a fitting parameter of the backpressure model to the experimentally observed pressure drop. The soot density $\rho_{\text{s,w}}$ within the filter thereby is a fit parameter. Within this work $\rho_{\text{s,w}} = 65.5 \text{ kg m}^{-3}$ has been

achieved. This value is in good agreement with the value of 70 kg m^{-3} found by Toops *et al.* [130], who used engine exhaust for filter loading. The permeability of the soot cake has been calculated using eq. (2.8). Thereby, a value of $k_{pl} = 3.9 \cdot 10^{-14} \text{ m}^2$ was achieved assuming a collector unit diameter $d_{c,pl} = 100 \text{ nm}$, which perfectly matches the soot permeability reported by Konstandopoulos *et al.* [129]. Similarly, the backpressure curve of SDPF2 loaded with a total amount of $m_{soot} = 4 \text{ g l}^{-1}$ could be described using Serrano's model.

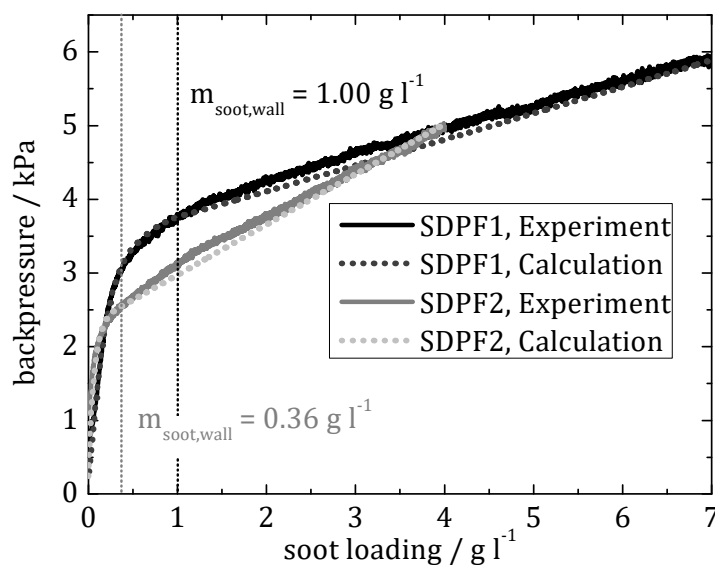


Fig. 43 Backpressure as a function of soot loading during a soot loading of an SDPF1 sample up to $m_{soot} = 7 \text{ g l}^{-1}$ and SDPF2 sample up to $m_{soot} = 4 \text{ g l}^{-1}$ (loading temperature 473 K , GHSV = 40.000 h^{-1}). The vertical dashed lines indicate the transition of the filter mode from depth-filtration to cake-filtration at a soot loading inside the pores of the filter wall of $m_{soot,wall} = 1 \text{ g l}^{-1}$ or $m_{soot,wall} = 0.36 \text{ g l}^{-1}$, respectively. The solid curves represent the measurements, while the dotted curves denote the result of the calculated backpressure according to the unit collector model (see Fig. 27).

5.3.2 Adsorption of NH_3 on soot free SDPF samples

In this subchapter the kinetic model for NH_3 adsorption/desorption was adjusted to describe the experimental data on a soot free SDPF1 sample and validated against model gas experiments. The NH_3 concentration from TPD experiments on a soot free SDPF1 sample is presented along with the calculated results in Fig. 44. The kinetic parametrization found within this work is given in Tab. 8.2. Evidently, the three-site kinetic reaction model presented in chapter 4.2 describes the experimentally observed NH_3 breakthrough very well. The two maxima in the desorption part starting at 300 min time-on-stream are reproduced by the model, thus supporting the multiple site NH_3 storage behavior of the zeolite-containing washcoat. Nevertheless, the calculated amount

of desorbed NH_3 is slightly overestimated. As reported before [141,173], for NH_3 adsorption/desorption experiments the amount of NH_3 adsorbed can be slightly higher than the amount of NH_3 released during the temperature ramp of TPD experiments. Park *et al.* [173] refer to this phenomenon as »non-thermally reversible storage for ammonia«, whereas Tan *et al.* [141] explained it with systematic errors in the NH_3 storage experiments. Since in this study no concentration drift over the time of the experiment was observed, systematic experimental errors can be excluded. Nevertheless, the adsorption part, which is the focus of the following model study on the soot influence on NH_3 adsorption behavior, is very nicely represented by the kinetic model.

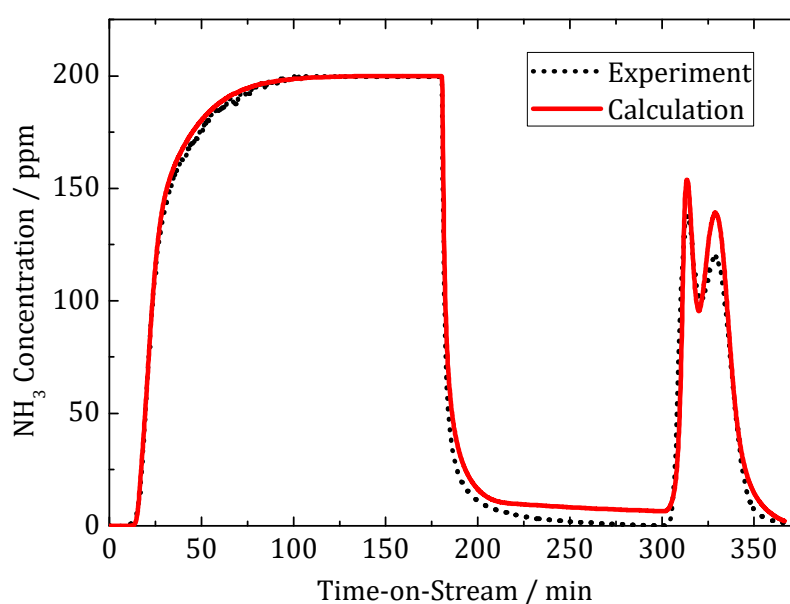


Fig. 44 NH_3 concentration as a function of time-on-stream during NH_3 adsorption and desorption experiment for a soot free SDPF1 sample. Experimental conditions as in **Fig. 38**. The solid curve indicates the model calculation, the dotted line is the result of the experiment.

The dependence of the NH_3 adsorption on the gas velocity yields crucial information for understanding the microscopic processes inside a soot loaded wall of SDPF. To assess the results at first the adsorption behavior for a soot free SDPF sample under different GHSV is studied. In **Fig. 45** the results of a NH_3 adsorption experiment for GHSV of 40 k h^{-1} , 80 k h^{-1} and 120 k h^{-1} is given. For a constant NH_3 inlet concentration (here 200 ppm) an increase in GHSV results in a NH_3 breakthrough at earlier time-on-stream. While for the experiment with 40 k h^{-1} the breakthrough was observed after 15 min of complete adsorption, for the 120 k h^{-1} experiment the breakthrough is achieved already at 2 min of NH_3 dosing. The appropriate adsorption rate calculated from the inlet and the outlet concentration during adsorption is given on the right. The higher GHSV yields a higher

NH_3 mass flow which could be completely adsorbed by the zeolite (not covered by soot). The relative amount of adsorbed NH_3 θ is a calculatory parameter of the kinetic model, representing the filling ratio of the NH_3 storage. Consequently, a filling level of $\theta = 0.5$ is achieved after 5 min on stream. The reduced GHSV of 40 k h^{-1} results in less NH_3 to be provided for adsorption. Although, similarly, all the incoming NH_3 is adsorbed, the lower incoming NH_3 mass flow results in a delayed storage filling. A filling level of $\theta = 0.5$ is found only after 15 min of dosing. In the case of a soot free sample the NH_3 uptake (rate of adsorption) only depends on the adsorption kinetics of the storage sites (eq. (4.4)) and thus, it strongly depends on the GHSV (**Fig. 45**, right). Both, for the 40 k h^{-1} and the 120 k h^{-1} experimental data on the NH_3 adsorption the kinetic model was applied yielding very good agreement. Consequently, dependence of the NH_3 adsorption on the GHSV for the soot free sample is very well implemented in the model. Thus, the kinetic model is an appropriate tool to study the influence of soot trapped inside the wall, which will be presented as follows.

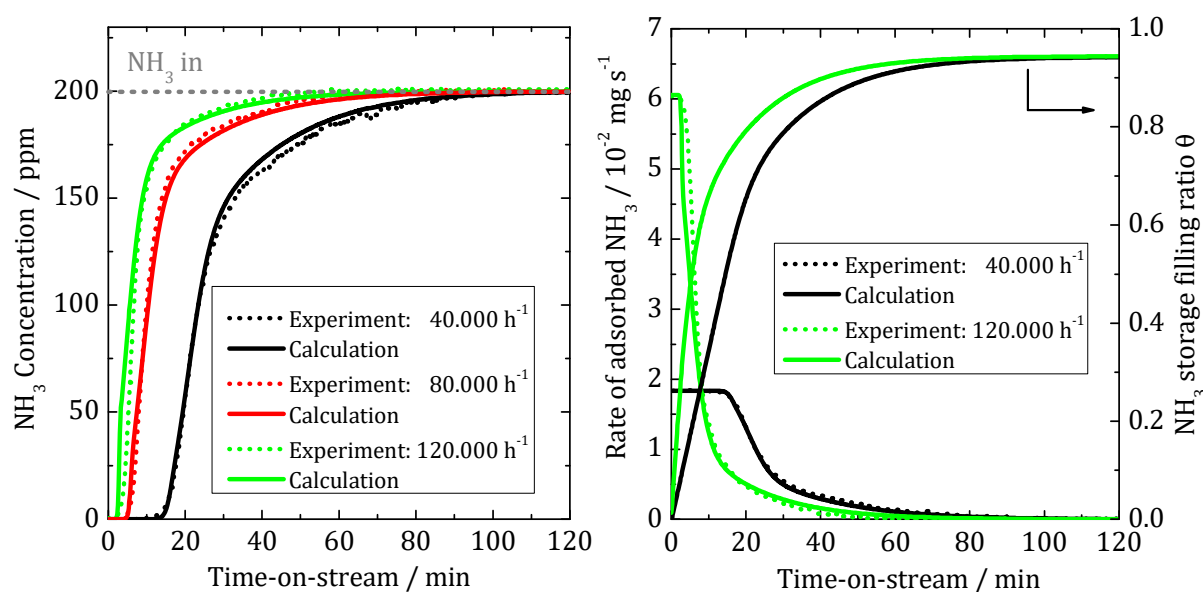


Fig. 45 Left: NH_3 concentration as a function of the time-on-stream for NH_3 adsorption experiments at different GHSV of 40 k h^{-1} , 80 k h^{-1} and 120 k h^{-1} (dotted lines). The inlet NH_3 concentration was 200 ppm dosed in N_2 at 423 K adsorption temperature. The appropriate kinetic model calculations are depicted as solid lines. Right: Rate of adsorbed NH_3 as a function of the time-on-stream during adsorption for the 40 k h^{-1} and 120 k h^{-1} experiment and appropriate calculations. Additionally, the NH_3 storage filling ratio θ as a function of the time-on-stream is depicted for the kinetic model calculations.

5.3.3 Influence of in-wall Soot Distribution on the Adsorption of NH₃

This subchapter deals with the effect of soot, distributed within the porous filter wall, on the NH₃ adsorption behavior. In the presence of soot inside the filter wall, we assume the diffusive transport of NH₃ through the porous soot layer to the zeolitic washcoat to be the governing process (compare **Fig. 27**). Consequently, diffusive mass transfer decreases the overall NH₃ uptake rate of the SDPF, but the amount of NH₃ adsorbed on the zeolite at saturation does not change in the presence of soot. Hence, the underlying kinetics of NH₃ adsorption of the active sites in the zeolite itself is not affected by the soot. The key parameter for the description of the transport process within soot loaded samples is the effective diffusivity D_{eff} of the gas molecules through the porous soot layer (eq. (4.2) and eq. (4.3)). In **Fig. 46** (left) the maximum possible soot layer thickness (5.1 μm for SDPF1) resulting from a complete filling of all the unit collectors within the porous wall is depicted by the brown dashed line. Hence, the order of magnitude of soot layer thickness d_s (μm range) is predefined by the geometry of the unit collector cell model (compare **Fig. 27**). It turns out, that D_{eff} determines the position of the inflection point in the adsorption branch of the TPD (see **Fig. 46**, right) under consideration of a fixed soot distribution throughout the filter wall. Variation of D_{eff} in the model until the experimentally observed and the calculated NH₃ concentration profiles match, results in an effective diffusivity of $D_{\text{eff}} = 1.9 \cdot 10^{-10} \text{ m}^2 \text{ s}^{-1}$ at 423 K for the gas species diffusion through the porous soot layer inside the wall to the washcoat. For the PFG-NMR measurement presented in chapter 5.1.3 an effective self-diffusivity $D_{\text{eff}} = 2.5 \cdot 10^{-9} \text{ m}^2 \text{ s}^{-1}$ at 298 K was found (see **Fig. 32**). The difference of these values seems to originate from a change in the diffusion process. For the sample measured with PFG-NMR (saturated with NH₃ at 10^5 Pa) gas phase diffusion dominates the gas transport. The found diffusivity, thus, represents an upper limit. For the model gas experiments the low NH₃ concentrations result in low surface coverage of the highly heterogeneous soot surface. Hence, we suppose the effective diffusivity is limited by surface diffusion.

Studying the diffusion within activated carbon particles using cyclohexane as probe molecule, Furtado *et al.* [174] found an effective diffusivity of $3.6 \cdot 10^{-10} \text{ m}^2 \text{ s}^{-1}$. Although structural deviations between porous soot and activated carbon are obvious, this value is in good agreement with the diffusivity found here using the kinetic model.

The soot agglomerated inside the porous wall may cause a limited mass flow of the NH₃ molecules to reach the zeolite-containing washcoat, thus, leading to the NH₃ slip through

the wall. The underlying adsorption kinetics of the NH_3 on the active sites in the zeolite itself is not affected by the soot. However, less NH_3 molecules reach the adsorbent per unit time. The brickwise kinetic modelling allows to validate different soot distributions within the filter wall by means of the resulting NH_3 adsorption or NO conversion. Each brick could be assigned with a certain soot mass resulting in a flow of NH_3 either to the washcoat within the brick or slipping to the next brick downstream (schematically shown in **Fig. 48**, left). Applying the unit collector model, the soot mass per brick defines the soot layer thickness $d_{s,n}$ on top of the washcoat for each brick. Thus, the corresponding soot distributions with the restriction of the soot mass conservation (experimentally observed soot loading $m_{\text{soot,wall}}$ and soot density from the backpressure model, chapter 5.3.1) can be found to describe the experimental results on NH_3 adsorption. As shown in **Fig. 46** (right), even the simple model assumption of the homogeneous soot distribution ($m_{\text{soot,wall}} = 1 \text{ g l}^{-1}$) along the porous wall describes the experimentally observed NH_3 slip behavior with an inflection point in the adsorption branch in a qualitative way (indicated with the point in **Fig. 46**, right). However, in the model calculation with the homogeneous soot distribution, half of the NH_3 mass flow is found to slip right after starting the NH_3 dosing. The same model shows a completely different behavior if no influence of soot is considered (see **Fig. 44**). In case of NH_3 slip at the SDPFs outlet observed during NH_3 adsorption using the SDPF wall brick model presented here, a considerable part of NH_3 entering a wall brick upstream slips to the downstream brick, as schematically shown in **Fig. 48** (left).

Obviously, the assumption of the homogeneous soot distribution along the porous wall is not sufficient to describe the observed NH_3 adsorption behavior. The qualitative influence of the soot on NH_3 slip behavior is, however, represented correctly.

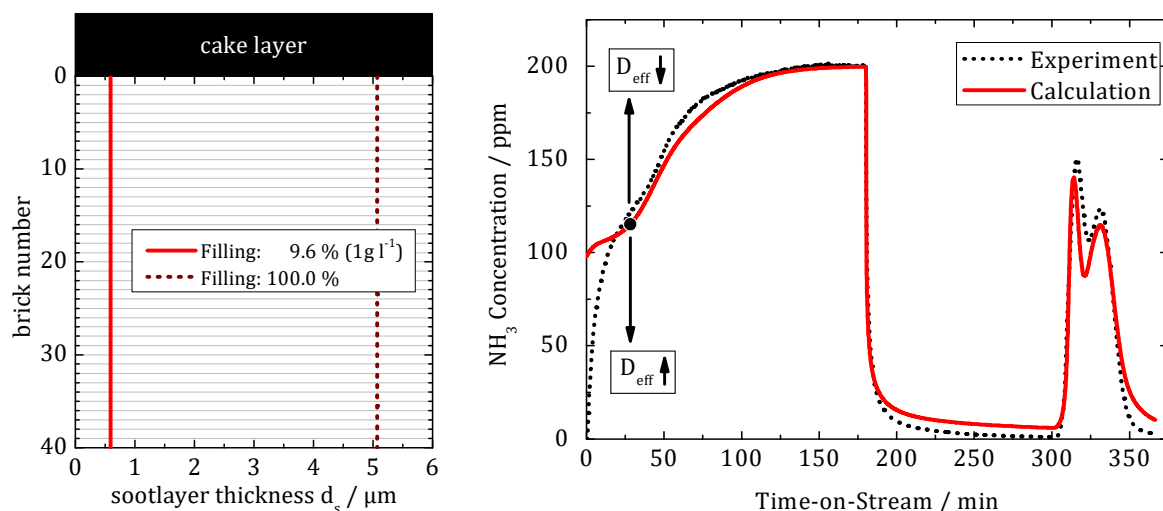


Fig. 46 Left: Spatial distribution of the soot layer thickness covering the zeolite throughout the filter wall (divided into bricks). The top part indicated the inlet channel (cake layer possible), the bottom part is the outlet channel of the SDPF. The red line indicates the case when the 1 g l^{-1} wall-trapped soot is evenly distributed (void volume of the unit collectors is filled up to 9.6 %). The brown dashed line represents the case, when all the collector cells are filled completely with soot (filling 100 %). Right: NH_3 concentration as a function of time-on-stream during a NH_3 adsorption/desorption experiment (experimental conditions as in **Fig. 38**). The black dotted curve corresponds to the experiment on a sample with $m_{\text{soot,wall}} = 1\text{ g l}^{-1}$, the red curve is the result of a model calculation using the soot layer-thickness distribution given on the left. The large black dot indicates the inflection point in the adsorption branch. Increasing or decreasing contribution of the soot represented by D_{eff} results in its shift, notified by the arrows.

Experimental [114,123] as well as theoretical studies [98,122,175] showed that soot deposition within the porous wall of DPFs more likely occurs close to the wall surface of the inlet channel. Depending on particle size, some of the soot particles are carried by the gas stream into the porous filter wall, slightly covering the mid part of the porous wall. Soot depositions in the vicinity of the outlet channel are not very likely. Unfortunately, the exact soot distribution throughout the porous wall could not be determined by the experimental methods available in this work.

Assuming the porous filter wall to be a homogeneous pore system, the filtration model reported in [124] was used to prove the soot distribution to be a monotonically decreasing function of the local coordinate from the inlet channel to the outlet channel (see **Fig. 64**, Appendix). Nevertheless, this filtration model in connection to the kinetic model was not able to describe the NH_3 adsorption very well, which may be due to simple model assumptions *e.g.* a single pore size of the porous wall.

Thus, the corresponding soot layer thickness distributions with the restriction of the soot mass conservation (experimentally observed $m_{\text{soot,wall}} = 1 \text{ g l}^{-1}$ in-wall soot loading) and to be a monotonically decreasing function may be found to describe the experimental results. In **Fig. 47** (left), three different soot profiles are presented. The corresponding TPD model calculation results are shown in **Fig. 47** (right). If the total soot mass is agglomerated close to the inlet channel (blue curve, called »surface distribution«), the resulting NH_3 concentration profile is similar to that of the soot free case. Due to the high diffusion restriction, the active sites of these soot loaded bricks have a negligible contribution to the NH_3 adsorption (over the observed time range). The appropriate NH_3 storage filling θ of the zeolite as a function of the time-on-stream during adsorption is given in **Fig. 48** (right) for the soot distributions under study. Thereby, the time-evolution of θ is the same for the soot free case and the »surface distribution« until all the uncovered washcoat parts are saturated with NH_3 until 20 min of dosing. For further time-on-stream the soot free sample fills up to $\theta = 0.94$, while for the »surface distribution« the restricted NH_3 mass flow to the soot covered washcoat parts results in smaller filling of $\theta = 0.89$ after 120 min of adsorption. A blocking of active sites by the soot is discussed by Schrade *et al.* [135] or Cavataio *et al.* [137]. For the studied time range of adsorption (120 min) this seems to be valid. Nevertheless, as shown in the model, the active sites are not blocked (NH_3 adsorption not prevented by soot) but the mass transfer through the soot layer is extremely slowed down (diffusive barrier). Hence, the soot covered bricks do not noticeably contribute to the overall NH_3 adsorption within 120 min of NH_3 dosing.

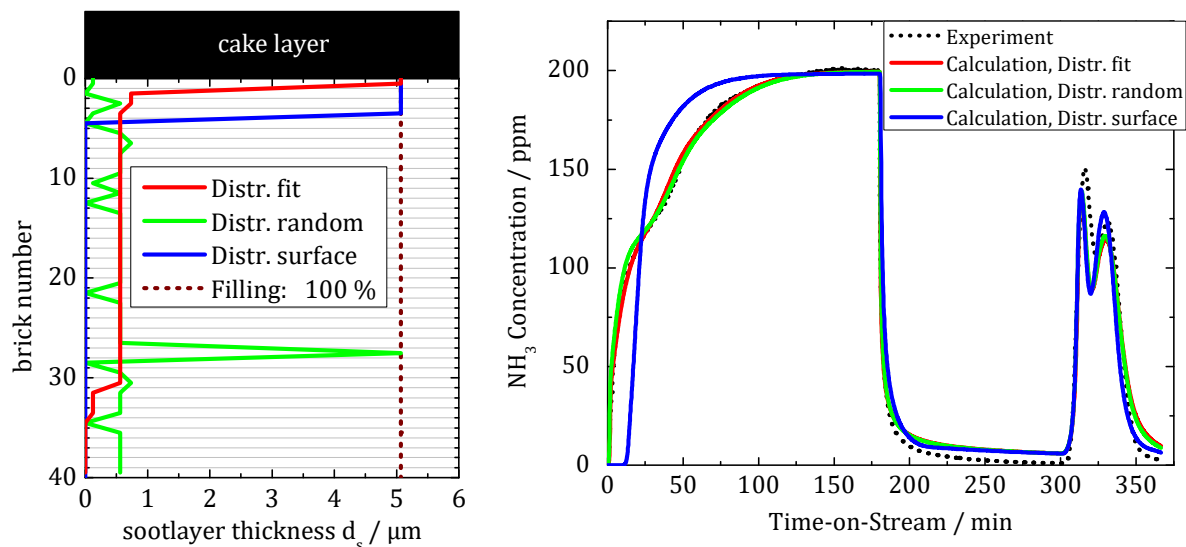


Fig. 47 Left: Spatial soot layer thickness distributions within the filter wall (divided into bricks) of 1 g l^{-1} in-wall soot. Right: NH_3 concentration as a function of time-on-stream during a NH_3 adsorption/ desorption experiment (experimental conditions as in **Fig. 38**). The dotted black curve indicates the experiment on a sample with $m_{\text{soot}} = 4 \text{ g l}^{-1}$, the solid colored lines are the result of a model calculation under usage of the respective soot layer-thickness distribution given on the left.

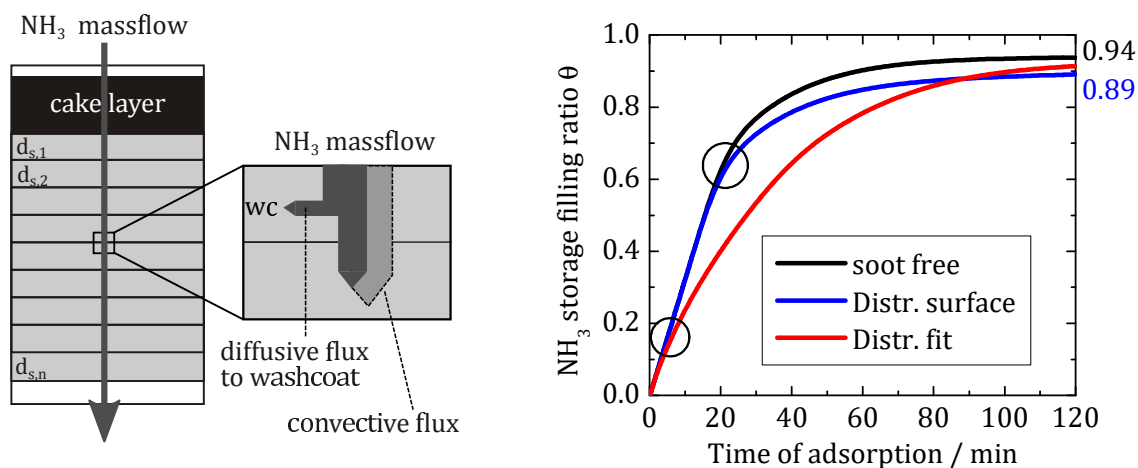


Fig. 48 Left: Schematic representation of the NH_3 mass flow distribution between two neighboring bricks. Within each brick a part of the incoming NH_3 is adsorbed by the washcoat (WC), while the rest slips to the next brick in the direction of the gas flow. The thicker, light grey arrow indicates higher NH_3 mass flow (*e.g.* by GHSV). Right: NH_3 storage filling ratio θ (result of model calculation) as a function of time-on-stream for different soot distribution (see **Fig. 47**, left) under study.

The black curve in **Fig. 47** (right) presents the NH_3 concentration calculated with high soot loading in the upper brick, slightly soot covered bricks below and no soot in the bottom bricks, which appears to be a realistic soot distribution as discussed in literature

[175]. The distribution is chosen here in the way that the resulting calculated NH_3 concentration profile matches the experimental TPD data. The distribution is termed as »fit distribution«. The time evolution of the calculated NH_3 storage filling ratio θ equals the one of the soot free case up to 5 min of NH_3 dosing, which is due to filling of the soot free bricks close to the outlet channel. At further time-on-stream the soot covered bricks fill up, resulting in decreased rate of NH_3 reaching the washcoat and hence in a decreased θ . The same good agreement between the modelled and experimental NH_3 adsorption behavior is, however, achieved by randomizing the previously found »fit distribution«, in a manner that the particular soot thicknesses of the bricks are kept unchanged but their local position within the porous filter wall is randomized (see the green line in **Fig. 47**, left). The obtained distribution fits the experimental results too, as shown in **Fig. 47** (right). However, we believe these profiles do not present a realistic scenario and will not further be discussed here. Thus the »fit distribution«, explaining the experimental data, is not a bijective assignment but it is very likely due to the demanded boundary conditions *e.g.* mass conservation and monotonically decreasing soot layer thickness towards outlet channel.

To check the model validity, other conditions for sample SDPF1, *e.g.*, 523 K adsorption temperature and 1000 ppm NH_3 inlet concentration, which are also relevant for automotive application, were applied. In **Fig. 63** (see Appendix), an appropriate experiment and a model calculation is shown. The experimentally observed and calculated NH_3 concentrations during the adsorption are given for a soot free and a soot loaded SDPF1 sample. The shape of the NH_3 adsorption branch is very similar as for the adsorption at 423 K as discussed above. Despite only the stronger storage sites are accessible at adsorption temperature of 523 K (**Fig. 39**), the inflection point in the adsorption branch of the soot loaded sample appears anyhow also under this experimental conditions. Hence, the NH_3 breakthrough behavior during adsorption is not a feature of partial interaction of the soot to only one of the observed NH_3 bonding sites. Under usage of the previously found »fit distribution« (**Fig. 47**, left, solid red curve), the model calculation of the NH_3 slip behavior agrees with the experimental data, confirming the principle of soot as diffusion barrier.

The NH_3 adsorption/desorption experiments in **Fig. 44** and **Fig. 47** show that soot affects the NH_3 adsorption behavior very much but the NH_3 desorption profiles of soot free and soot loaded samples are much closer to each other. Both directions of molecule transport

are affected by the diffusive barrier, implemented as diffusive flux $\frac{D_{\text{eff},k}}{d_s}(x_{s,k} - x_{wc,k})$ in eq. (4.2) and eq. (4.3). During NH_3 adsorption the gas concentration at the soot layer surface $x_{s,k}$ is limited due to the given inlet concentration. During desorption the NH_3 concentration on the washcoat surface $x_{wc,k}$ is relatively high, which leads to a high diffusive flux through the soot, thus sufficiently decreasing the rate limiting influence of its diffusive barrier. The value of the diffusive flux seems to be comparable to the rate of desorption of NH_3 from the zeolitic washcoat in this experiment. That leads to a similar NH_3 -slip behavior of soot free and soot loaded samples during desorption under given conditions. Nevertheless, the shift of the maxima of the desorbed NH_3 concentration towards higher time-on-stream, shown in **Fig. 39**, is assigned with influence of the diffusive barrier. However, the model is capable of describing this effect as observed by the experiments.

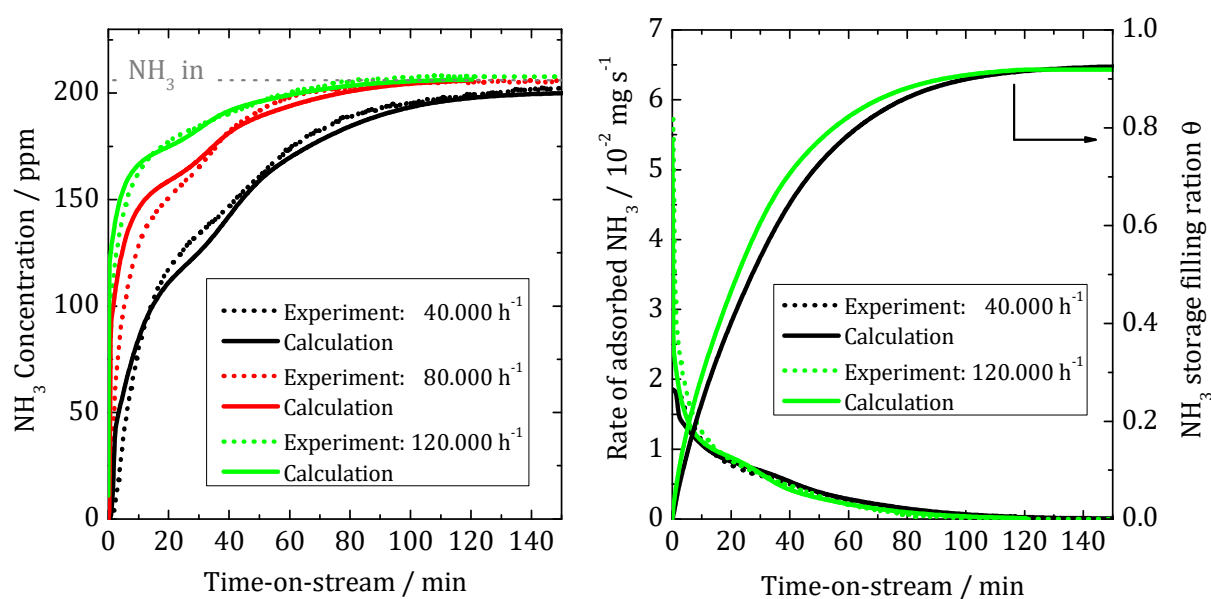


Fig. 49 Left: NH_3 concentration as a function of the time-on-stream for NH_3 adsorption experiments at different GHSV of 40 k h^{-1} , 80 k h^{-1} and 120 k h^{-1} for soot loaded $m_{\text{soot,wall}} = 1 \text{ g l}^{-1}$ SDPF1 sample (dotted lines). The experimental conditions are the same as in **Fig. 45**. The appropriate kinetic model calculations are depicted as solid lines. Right: Rate of adsorbed NH_3 as a function of the time-on-stream for the 40 k h^{-1} and 120 k h^{-1} experiment and appropriate calculations. Additionally, the NH_3 storage filling ratio θ as a function of the time-on-stream is depicted for the kinetic model calculations.

Following the study of the dependence of the NH_3 adsorption on the GHSV for a soot free sample (**Fig. 45**), the soot loaded sample is studied under the same conditions (**Fig. 49**). As typical for soot loaded sample, the NH_3 breakthrough during adsorption was observed starting with dosing for all the GHSV under study (40 k h^{-1} , 80 k h^{-1} and 120 k h^{-1}).

Nevertheless, as an increase in GHSV (at same NH_3 inlet concentration) yields an increase in the NH_3 mass flow. As discussed above, the rate of NH_3 uptake by the zeolite is limited by the diffusion rate of NH_3 through soot. Hence, the slope of the NH_3 breakthrough curve during adsorption becomes steeper with increasing GHSV. Both the 40 k h^{-1} and the 120 k h^{-1} experiment have also been calculated under usage of the »fit distribution« discussed in **Fig. 47**. On the right of **Fig. 49** the appropriate rate of NH_3 adsorption was calculated from the experiment and by means of the kinetic model. Contrary to **Fig. 45** (soot free), the rate of adsorption on a soot loaded sample is nearly independent from the GHSV, which is to be expected from a mass transport barrier (we assume the soot to be). The slight differences in the adsorption rate as well as the NH_3 storage filling ratio are the result of adsorption on the soot free parts of the porous wall. With start of NH_3 dosing these bricks fill up with different adsorption rates depending on the GHSV (the higher the GHSV, the higher the adsorption rate).

In the subchapter above a theoretical soot distribution has been found to describe the earlier NH_3 breakthrough behavior, experimentally observed during NH_3 adsorption experiments on soot loaded samples. Considering soot as diffusion barrier, the shape of the NH_3 breakthrough curve was studied in detail. Thereby, the diffusivity of NH_3 molecules through the soot layer could be found as fit parameter to the kinetic model.

5.3.4 Influence of in-wall Soot Distribution on the SCR DeNO_x Behavior

In this subchapter the kinetic model was applied to study the NO conversion in a temperature programmed SCR reaction on soot free and soot loaded SDPF1 samples. In **Fig. 50**, the experimental and the calculated light off curves for the soot free and the soot loaded (1 g l^{-1}) SDPF1 samples are shown. For the soot loaded case the same soot distribution as for the TPD experiments was considered (»fit distribution« in **Fig. 47**, left). A good agreement was found for the calculated and the experimentally observed NO conversion for a soot free case (black lines), representing a good model calibration of the kinetic parameters.

For the model description of temperature programmed SCR reactions on soot loaded samples, the temperature dependence of the diffusivity $D_{\text{eff}}(T)$ is very important. As the diffusion of the gas species through the soot layer was found to be the governing process (chapter 5.1.3), according to Dvoyashkin *et al.* [160] the following temperature dependence was applied:

$$D_{\text{eff}}(T) = D_0 \cdot \exp(-E_{a,D}/RT) \quad (5.5)$$

Thereby, the pre-exponential factor D_0 was chosen in order to hold $D_{\text{eff}}(423 \text{ K}) = 1.9 \cdot 10^{-10} \text{ m}^2 \text{ s}^{-1}$ (found in chapter 5.3.3). An activation energy of $E_{a,D} = 2.5 \text{ kJ mol}^{-1}$ was found as fit parameter of the kinetic model in order to meet the temperature dependence of the experimentally observed NO conversion on soot loaded SDPF sample in the temperature range of 423 K to 673 K. As, to the best of our knowledge, the diffusion of gas molecules in a soot layer has not been reported in literature before, the activation energy found here as a fit parameter of the kinetic model could not be finally assessed.

Nevertheless, without further optimization or assumptions, the model under usage of the »fit distribution« discussed above and the found temperature dependence of the diffusivity $D_{\text{eff}}(T)$ fits very well to the SCR experimental results for the sample with $m_{\text{soot}} = 1 \text{ g l}^{-1}$ (see **Fig. 43**, SDPF1). This again supports the conclusion made above, *i.e.*, that the underlying mechanism is the diffusion of reactants through the in-wall soot layer is the underlying mechanism limiting the NH_3 adsorption and SCR reaction kinetics.

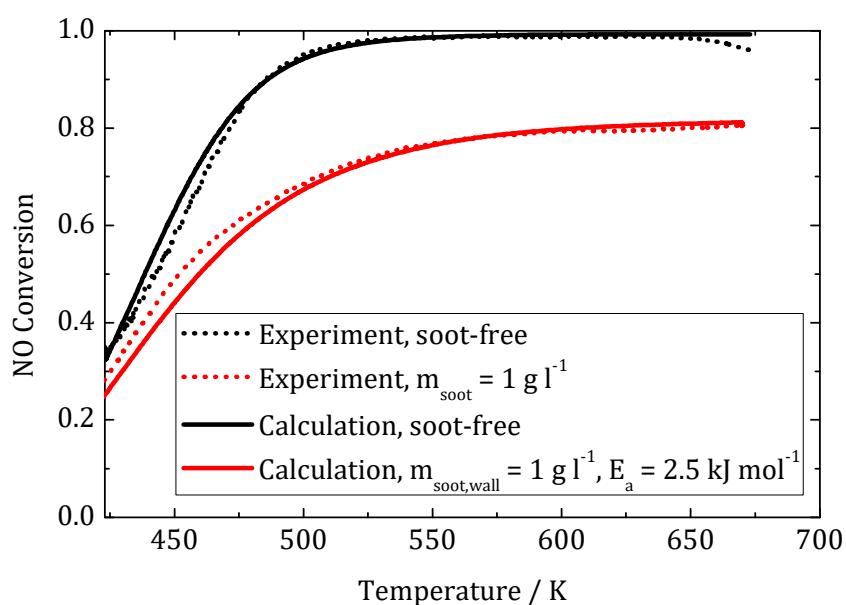


Fig. 50 NO conversion as a function of the temperature (Light-off curves) for a soot free and a soot loaded ($m_{\text{soot}} = 1 \text{ g l}^{-1}$) SDPF1 sample at $n(\text{NO}_2)/n(\text{NO}_x) = 0$ in an SCR experiment. The dotted lines represent the experimental data (conditions as in **Fig. 42**, left). The solid lines are the calculated light-off curves for a soot free and a soot loaded ($m_{\text{soot,wall}} = 1 \text{ g l}^{-1}$) sample. The activation energy for the temperature dependence of the diffusion coefficient (2.5 kJ mol^{-1}) was found as fit parameter.

In following, the effect of a variation of the in-wall soot distribution by constant soot amount ($m_{\text{soot,wall}} = 1 \text{ g l}^{-1}$ for SDPF1) on the SCR activity has been studied by means of the model. Under the boundary condition that a downstream brick only implements a soot amount which is equal or less than the appropriate soot amount within the brick above, possible soot loading regimes have been considered within this study. According to theoretical works on filtration models of *e.g.* [124,175], this way of distributing the soot within the wall is assumed to cover all the realistic loading regimes. Thereby, a soot distribution of all the soot in close vicinity to the inlet channel and a homogeneous soot distribution covering the entire catalyst represent the theoretical limiting cases of distributing 1 g l^{-1} soot within the porous filter wall (**Fig. 51**, left).

Implementing these possible soot distributions within the kinetic model, it turned out that explicitly the both limiting cases of soot distributions of 1 g l^{-1} in-wall soot lead to the lowest and the highest NO conversion, found within this work for SDPF1. The appropriate results are depicted in **Fig. 51** (right). For the solid blue distribution («surface distribution») all the soot is located close to the inlet channel inside the porous wall (only 10 % soot penetration into porous wall). The NO reduction mainly occurs within the soot free part of the filter wall, which results in an overall NO conversion very similar to that of the non-loaded case (see dotted black line). The NO conversion is only up to 3 % lower compared to that of the soot free sample. The same result was found experimentally by Schrade *et al.* [135]. Nevertheless, they did not report on the soot distribution within the filter wall. Consequently, the study presented here suggests that all the soot inside the porous wall for the SDPF samples under study of Schrade *et al.* was covering only few of the active sites. This might be due to a special filter concept (stop-layer [120]) or a high VOF of the engine soot, making it sticky and promoting soot deposition inside the wall close to the inlet channel. The lowest calculated NO conversion (solid black line) is achieved when the soot loading of 1 g l^{-1} is equally distributed throughout the whole filter wall. As the entire catalyst inside the wall is then covered by soot at any position of the wall, the gas flux to the active sites is limited by the gas diffusion through the soot layer. Thus, the distribution of the soot within the porous filter wall strongly influences the maximum NO conversion. A difference in NO conversion of 45 % was observed just by different soot distributions. Tronconi *et al.* [138] reported on loss in NO conversion up to 20 % investigating a physical mixture of soot (PrintexU) and powered catalyst. In the study of Tronconi *et al.*, 5 mg of soot were mixed with 50 mg Cu-zeolite and 50 mg

powdered cordierite (4.8 wt.-% soot). In our work, $m_{\text{soot}} = 1 \text{ g l}^{-1}$ loaded in an SDPF1 sample resulted in 0.2 wt.-% soot. Obviously, the situation for a soot loaded filter wall is different compared to a physical mixture of soot and powdered SDPF. Hence, 24 times more soot is needed to cover the catalyst particles within the physical mixture and thus, to achieve a similar NO conversion loss of about 20 %. In **Fig. 51** (right) additional experimental NO conversion curves are shown for SDPF1 samples with $m_{\text{soot}} = 1 \text{ g l}^{-1}$ and 7 g l^{-1} (1 g l^{-1} soot in wall + 6 g l^{-1} soot in cake layer, see **Fig. 43**). Both measured NO conversions are located in the range, defined by the calculatory minimal and maximal possible conversion. Accordingly the soot distributions for the samples used in the experiment have to be something in between the both extreme cases *e.g.* the »fit distribution« in **Fig. 47** (left), explaining the measured NO conversion of 1 g l^{-1} soot loading. Assuming that during the soot loading of the sample with 7 g l^{-1} (loading process lasts 7 times as long as for 1 g l^{-1}), in-wall soot will be wafted closer to the outlet, shifting the soot distribution towards the extreme case for minimal NO conversion (**Fig. 51**, solid black line), the slight decrease towards lower conversion for the 7 g l^{-1} sample could be explained.

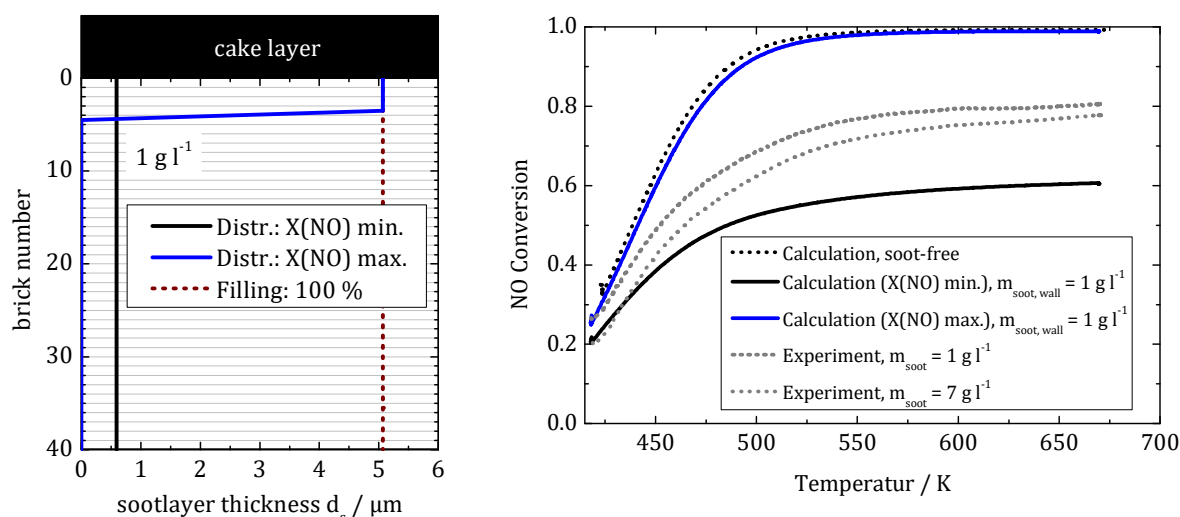


Fig. 51 Left: Spatial distributions of the soot layer thickness throughout the filter wall (divided into bricks) for the two cases revealing the minimal (solid black line) and the maximal possible (solid blue line) NO conversion in standard SCR experiments for the same amount ($m_{\text{soot, wall}} = 1 \text{ g l}^{-1}$) of soot trapped inside the filter wall. Right: NO conversion as a function of the temperature for standard SCR experiments on soot loaded ($m_{\text{soot}} = 1 \text{ g l}^{-1}$ and 7 g l^{-1}) SDPF samples (given as dashed grey lines, experimental conditions as in **Fig. 42**). The two solid lines are the result of a model calculation under usage of the respective soot layer-thickness distribution given on the left for minimum and maximum NO conversion under soot loading. The dotted black line represents the calculated NO conversion for the sample without soot.

All the experimental and model calculation results presented here, suggest that the difference of the NO conversion and of the NH_3 adsorption/desorption profiles comparing the soot free to the soot loaded cases originate from a pure diffusion limitation phenomenon through soot inside the porous wall. Although soot is present, all active sites are accessible (compare **Fig. 39**). Therefore, the intrinsic kinetic rates of the chemical reactions at the active sites of the zeolite are not affected, but the rate of molecular transport towards the zeolite is reduced by the soot barrier on top of the washcoat. On the contrary, Park *et al.* [145] attributed the influence of soot on the DeNO_x behavior in reduced kinetic reaction rates. Nevertheless, and in accordance with Park *et al.* the soot-induced changes in the catalytic activity have a physical rather than a chemical origin as they result from a diffusion barrier presented by the soot. As shown in **Fig. 51** (right, grey line) already a slight but homogeneous distribution of soot on top of the washcoat inside the porous wall material (**Fig. 51** left, grey line) leads to a dramatic loss of the SCR performance. Consequently, from the point of catalytic activity it is advisable to prevent soot penetration inside the washcoated filter wall. This could be realized by a “stop-layer” design described by Koltsakis *et al.* [120]. As the cake filtration provides approximately

perfect filtration, the target should be to reach the cake filtration regime as soon as possible, avoiding the deep bed filtration regime. Koltsakis *et al.* [120] showed that the stop-layer design notably reduces the duration to reach cake filtration. This almost completely avoids the formation of soot trapped inside the porous wall, which, as shown by the backpressure model, has the largest contribution to the filter backpressure. Furthermore in-wall filtered soot, which was proven here to have a negative influence on the catalytic activity, can thus be avoided. According to Mizutani *et al.* [84] the stop-layer leads to improved fuel economy (decreased backpressure) and a linear relation between pressure drop and soot loading (no deep bed filtration). This enables an easier on-board estimation of the soot amount loaded in the particulate filter for application. As shown in [114], a filter design without a stop-layer (as investigated here) leads to soot penetration depths inside the porous wall of about 40 μm (10 % of the wall thickness). However, there will still be a slight soot amount that passes the surface pores until these are plugged, distributing within the rest of the porous filter wall. According to the results of the presented study, even a thin soot layer (0.6 μm) slightly covering all of the catalyst (see **Fig. 51**, curve for minimum NO conversion), reducing the NO conversion for up to 45 %. In consequence our study strongly supports the layered SDPF design [120] or a washcoating concept where most of the washcoat is impregnated in the wall part close to the outlet channel.

In the subchapter above different theoretical soot distributions have been studied by means of the kinetic model. Thus, the decrease in NO conversion under soot loading found by experiments in this work as well as reported in literature could be entirely explained. A temperature dependence of the diffusivity could be found as result of fitting the kinetic model to temperature programmed standard SCR experiments.

5.3.4.1 Parameter Study on the Diffusion Barrier in the kinetic Model

Within this subchapter parameter dependencies of the diffusion barrier on the DeNO_x behavior are discussed in detail. The theoretical considerations are thereby supported by proper model gas experiments. According to the mass conservation equations (4.2) and (4.3) the ratio of the effective diffusivity and the thickness of the soot barrier $\frac{D_{\text{eff}}}{d_s}$ is responsible for the restriction of the gas transport to the active sites and hence for a change in NH₃ adsorption or NO conversion. Consequently, an increase in d_s and a

decrease in D_{eff} lead to the same increase in mass transport limitation and *vice versa*. In the following, reasons for a changing d_s or D_{eff} are discussed.

At first, the model is validated under extreme loading conditions. In **Fig. 52** (right) the result of a NH_3 adsorption experiment for a SDPF1 sample with soot loading of $m_{\text{soot}} = 25 \text{ g l}^{-1}$ is shown. For vehicle application $m_{\text{soot}} = 10 \text{ g l}^{-1}$ [126] is the upper limit for soot mass in the filter, which is due to avoid damage by the thermal stress during regeneration (up to 1300 K). That is why the scenario with $m_{\text{soot}} = 25 \text{ g l}^{-1}$ is very unrealistic, nevertheless, the principle of the diffusive barrier should also hold. Indeed, an extreme shaping of the NH_3 breakthrough curve for the soot loaded sample was observed. Right after dosing starts, nearly 150 ppm NH_3 (out of 200 ppm NH_3 dosed) slips through the filter without being adsorbed. Afterwards a flattened regime of NH_3 outlet concentration is measured, indicating adsorption at very low NH_3 adsorption rate until after 180 min of NH_3 dosing the adsorption of the zeolite saturates (as inlet concentration equals outlet concentration; only 90 min for soot free SDPF sample in **Fig. 44**). The experimentally observed NH_3 adsorption curve is even flatter than a model calculation under usage of the soot distribution covering all zeolite over the porous wall thickness (red dashed line, $m_{\text{soot}} = 1 \text{ g l}^{-1}$), which is the calculatory case, yielding the maximum loss in catalytic activity (discussed in **Fig. 51**). Consequently, the ratio $\frac{D_{\text{eff}}}{d_s}$ delivers values which are too large to fulfill the experimentally observed NH_3 adsorption behavior under extreme high load condition. Nevertheless, two effects are conceivable to explain the experiment. On the one hand, during soot loading of the sample with 25 g l^{-1} (loading process lasts 25 times as long as for 1 g l^{-1}), in-wall soot is very likely to be wafted closer to the outlet. At the inlet channel soot particles break away from the cake layer and deposit inside the porous filter wall. Hence, the in-wall soot mass $m_{\text{soot,wall}}$ increases. Under assumption of the soot density ($\rho_{s,w} = 65.5 \text{ kg m}^{-3}$) to remain constant, the thickness of the soot depositions within the wall (d_s) will increase. With constant $\rho_{s,w}$ also soot structure and thus the diffusivity will not change. Hence, the ratio $\frac{D_{\text{eff}}}{d_s}$ is determined by the soot layer thickness d_s . Under usage of the kinetic model, a soot layer thickness distribution with $m_{\text{soot,wall}} = 3 \text{ g l}^{-1}$ was found («high load distribution», dark grey line in **Fig. 52**), explaining the experimental NH_3 adsorption profile very well. Comparing it to the «fit distribution» ($m_{\text{soot,wall}} = 1 \text{ g l}^{-1}$), it is obvious that d_s increased for each brick, resulting in increased mass transport limitation. Unfortunately, the process of a slight filling of the porous filter wall

during the whole soot loading time as a consequence of a slight wafting of soot particulates from the cake layer into the wall can not be observed by the backpressure measurement. In **Fig. 65** (Appendix) the backpressure curve of the 25 g l^{-1} soot-loading is depicted. As the measured pressure at each time is a snapshot, also this curve yields the information of 1 g l^{-1} in-wall soot by the change in slope indicating transition from deep bed to cake filtration. In **Fig. 53** the modelled NO conversion under usage of the soot distributions given in **Fig. 52** (left) is depicted. It is expected that the »high load distribution« (which explains the NH_3 adsorption behavior) would lead to a maximum NO conversion of 53 % (at 673 K). The »fit distribution« (which explains the NH_3 adsorption behavior and NO conversion for medium soot loadings up to $m_{\text{soot}} = 4 \text{ g l}^{-1}$) yields a maximum of 81 %. Hence, additional 2 g l^{-1} of in-wall soot result in further conversion drop of 18 %.

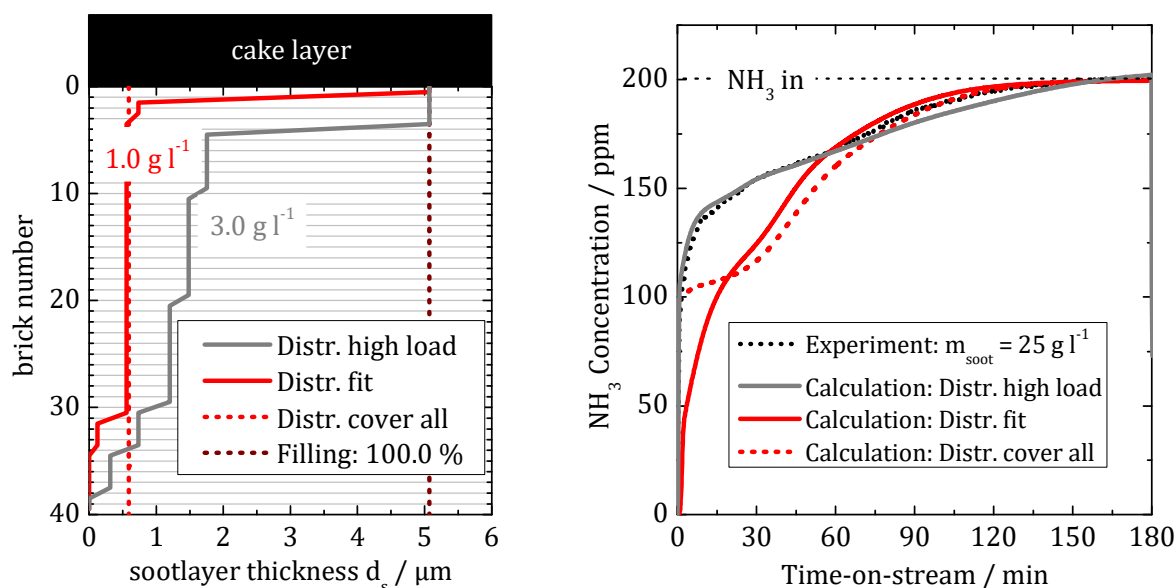


Fig. 52 Left: Spatial soot layer thickness distributions within the filter wall (divided into bricks) of $m_{\text{soot,wall}} = 1 \text{ g l}^{-1}$ (»fit distribution«) and the distribution equally covering all the washcoat) and 3 g l^{-1} (»high load distribution«). Right: NH_3 outlet concentration during adsorption as a function of time-on-stream (experimental conditions of the model gas experiment as in **Fig. 38**). The dotted curve indicates the experiment with the sample with very high soot loading of $m_{\text{soot}} = 25 \text{ g l}^{-1}$, the solid lines and the dashed line are the result of a model calculation under usage of the respective soot layer-thickness distribution given on the left.

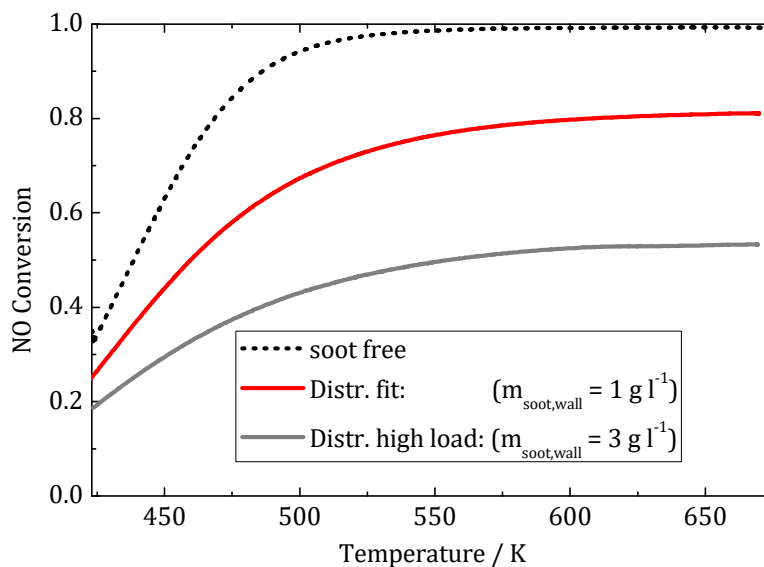


Fig. 53 NO conversion as a function of the temperature for kinetic model calculation of standard SCR for a soot free sample (dashed line) and under application of the soot distributions given in **Fig. 52** (left).

On the other hand, a likely scenario yielding a reduction of the ratio $\frac{D_{\text{eff}}}{d_s}$ is by reducing the effective diffusivity. As found by Yapaulo *et al.* [123] a higher gas velocity during soot loading results in higher soot mass deposited inside the porous wall. Thereby, the soot penetration depth has not been changed significantly. Hence, a densification of the soot deposits inside the porous wall is implied. As suggested by Park *et al.* [145], the Knudsen diffusion is the fundamental process for gas diffusion through a soot layer. According to eq. (2.20) a densification will lead to reduced soot porosity ϵ_{pl} and pore width d_p connected with an increase in tortuosity τ_k , thus a reduction in Knudsen diffusivity D_k is achieved.

In **Fig. 54** (left) experimentally observed temperature dependence of the observed NO conversion rates is depicted. During soot loading (up to $m_{\text{soot}} = 4 \text{ g l}^{-1}$) the GHSV of the exhaust from the soot-generator was varied. The case of 100 k h^{-1} represents the standard loading procedure used in this study, for the case of 48 k h^{-1} the dilution gas (10 l min^{-1}) was switched off. The light off curve achieved at lower GHSV during soot loading clearly shows a higher NO conversion compared to the 100 k h^{-1} case. Up to 7 % increase in NO conversion was observed just by a variation of the soot loading GHSV in the range given above. According to Yapaulo *et al.* an increased gas velocity during loading results in more soot mass deposited inside the porous filter wall as a consequence of higher soot density. On the right side of **Fig. 54** a model calculation of the NO conversion is depicted for

different effective diffusivities under study. Thereby, the pre-exponential factor of the temperature dependence of the diffusivity (eq. (5.5) with $E_{a,D} = 2.5 \text{ kJ mol}^{-1}$) was varied in order to achieve an effective diffusivity in the range of $5 \cdot 10^{-9} \text{ m}^2 \text{ s}^{-1}$ to $5 \cdot 10^{-11} \text{ m}^2 \text{ s}^{-1}$ at 423 K. The »fit distribution« was used as soot layer thickness distribution and kept constant for all the calculated light off curves, thus the diffusivity is the parameter changing the ratio $\frac{D_{\text{eff}}}{d_s}$. The dependency could be clearly observed: the lower the effective diffusivity, the lower the resulting NO conversion. Whereas $D_{\text{eff}} = 5 \cdot 10^{-9} \text{ m}^2 \text{ s}^{-1}$ results only in a minor diffusive barrier and therefore in a NO conversion curve close to the soot free case (98 % maximum conversion), $D_{\text{eff}} = 5 \cdot 10^{-11} \text{ m}^2 \text{ s}^{-1}$ (2 orders of magnitude lower) leads to a dramatic loss in NO conversion (maximum value of 64 %). Hence, effective diffusivities could be found, explaining the experimentally observed drop in NO conversion by the variation of the GHSV during soot loading (dashed lines). While $D_{\text{eff}} = 2 \cdot 10^{-10} \text{ m}^2 \text{ s}^{-1}$ at 423 K is the diffusivity explaining the NO conversion on the samples loaded at GHSV of 100 k h^{-1} (standard condition used for all other soot loading experiments and model calculations done in this work), the experimentally observed conversion for the sample loaded at 48 k h^{-1} could be described by the model under usage of a diffusivity of $D_{\text{eff}} = 4 \cdot 10^{-10} \text{ m}^2 \text{ s}^{-1}$ at 423 K (2 times higher). Koltsakis *et al.* [176] found the soot density within the porous wall $\rho_{s,w}$ to vary from 25 to 100 kg m^{-3} . Thereby, it depends (among others) on the flow velocity during loading. Referring the soot porosity on the density of graphene (2260 kg m^{-3}), a soot porosity value of $\epsilon_{s,w} = 1 - \frac{\rho_{s,w}}{2260 \text{ kg m}^{-3}} = 0.97$ was found for $\rho_{s,w} = 65.5 \text{ kg m}^{-3}$ (soot density is a result of backpressure measurement, chapter 5.3.1, for soot loading at GHSV of 100 k h^{-1}). According to the equation for Knudsen diffusion (2.20) the soot porosity alone could not explain a change in diffusivity by a factor of 2 as consequence of reduced soot density (due to reduced gas velocity during soot loading). Hence, a decrease in tortuosity τ_k or an increase in the pore width d_p of the soot layer could be possible explanations for the increased diffusivity and thus for the observed increase in NO conversion when gas velocity during soot loading is reduced. Otherwise this could also suggest that Knudsen diffusion is not the present diffusion process governing gas transport of gas molecules in the soot under study.

Within this subchapter the meaning of the ratio $\frac{D_{\text{eff}}}{d_s}$ for the kinetic modelling of the NO conversion under soot loading has been emphasized. Experimental scenarios either

changing d_s or D_{eff} have been discussed. Nevertheless, a model based determination of one of the parameters always implies a fixing of the other parameter under certain error.

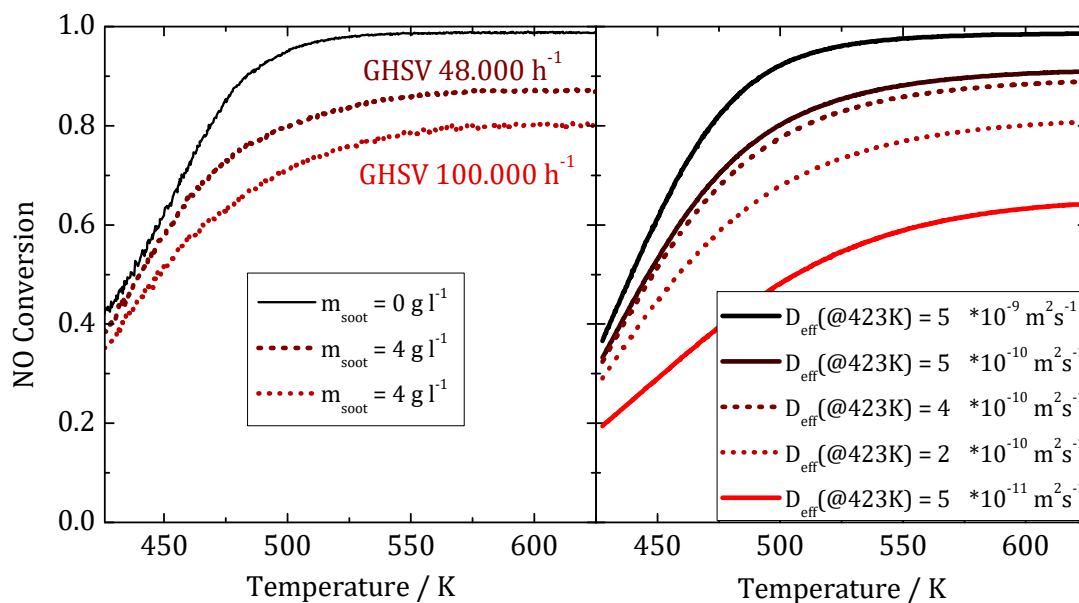


Fig. 54 NO conversion as a function of the temperature. Left: Temperature programmed SCR experiment on a soot free SDPF1 (solid black line) sample and two SDPF1 samples with $m_{soot} = 4 \text{ g l}^{-1}$ (experimental conditions as in **Fig. 42**, left). During soot loading the GHSV of the exhaust from the soot-generator was varied: 48 k h^{-1} (dashed) and 100 k h^{-1} (dotted), all other soot loading conditions as described in chapter 3.3.3. Right: Model calculations of temperature programmed SCR under variation of the effective diffusion coefficient. The dashed lines indicate the model calculations representing the experimentally observed NO conversion on the right.

5.3.4.2 Model Results for SDPF with changed Pore Geometry

To prove model validity, within this subchapter the kinetic model was applied on another SDPF sample (SDPF2). This sample reveals less pore volume (**Fig. 62**, Appendix) and a smaller pore width (mean pore size of $17 \mu\text{m}$, **Tab. 3.1**) compared to SDPF1. In **Fig. 42** experimental as well as model calculations of the temperature dependence on the NO conversion is depicted. In the experiment on NO conversion a decrease up to 7 % was observed for the $m_{soot} = 1 \text{ g l}^{-1}$ soot loaded SDPF2 sample. Thereby, an in-wall soot mass of $m_{soot,wall} = 0.36 \text{ g l}^{-1}$ has been evaluated by means of backpressure measurement (**Fig. 43**). On contrary for SDPF1 the conversion dropped by 20 % under $m_{soot,wall} = 1 \text{ g l}^{-1}$ soot loading, strongly suggesting that the soot mass inside the porous wall has a major influence on the resulting catalytic activity. The unit collector model has been applied to the geometric parameters of SDPF2. As can be seen in **Fig. 55** (left) the unit collector cells of the SDPF2 configuration are much smaller. While for SDPF1 a maximum soot layer thickness of $d_s = 5.1 \mu\text{m}$ was possible, for SDPF2 only a soot layer of $3.4 \mu\text{m}$ is possible to

cover the washcoat. Under the restriction of $m_{\text{soot,wall}} = 0.36 \text{ g l}^{-1}$ a soot layer thickness distribution could be found, explaining the experimentally observed decrease in NO conversion for up to 7 % (given on the right). The found distribution features soot penetration depth inside the porous wall up to brick 6 (equals 15 % of the wall thickness). Thereby, most of the soot is distributed close to the inlet channel. The rest of the washcoated filter wall is not covered by soot. Hence, the large volume of the porous wall which is soot free (85 %) still enables good catalytic activity (similar to soot free case). Furthermore, the two theoretical soot distributions yielding the calculatory minimum and maximum in NO conversion are studied. When soot ($m_{\text{soot,wall}} = 0.36 \text{ g l}^{-1}$) slightly covers the entire catalytic surface the minimal NO conversion results, which is up to 10 % less than the soot free case. On contrary for SDPF1 with $m_{\text{soot,wall}} = 1 \text{ g l}^{-1}$ a drop of up to 40 % resulted as calculatory minimum case. For the »fit distribution« of SDPF1 a soot penetration down the filter wall up to 85 % was found (using the model), ongoing with a loss in SCR-catalytic activity leading to a decrease of up to 20 % of NO conversion. Consequently, the soot penetration into the porous wall (covering the zeolite) is the crucial parameter to explain the observed effect of the soot loading on the SCR activity as well as the NH_3 adsorption.

The model assisted investigation presented here is thus giving the explanation for the deviation in NO_x conversion of soot loaded samples from other literature reports. Schrade *et al.* [135] and Mihai *et al.* [136] observed a decrease in NO conversion up to 5 %, while Cavataio *et al.* [137] and Tronconi *et al.* [139] observed up to 20 % loss in catalytic activity for a soot loaded samples compared to the soot free case. All these studies did not mention the backpressure curves or the mass of in-wall soot for the SDPF samples under their investigation. That is why a quantitative evaluation of their results is not possible. Nevertheless, model assisted investigation on both SDPF samples presented here (SDPF1 and SDPF2) strongly suggests, that the mass of in-wall soot and its penetration depth inside the porous wall seems to be the key to explain the huge deviation in the reported NO conversion values.

Within this subchapter it could be proven, that a decreased pore width of the SDPF filter wall, ongoing with a decrease of the soot mass trapped inside the pores ($m_{\text{soot,wall}}$), results in a less NO conversion drop.

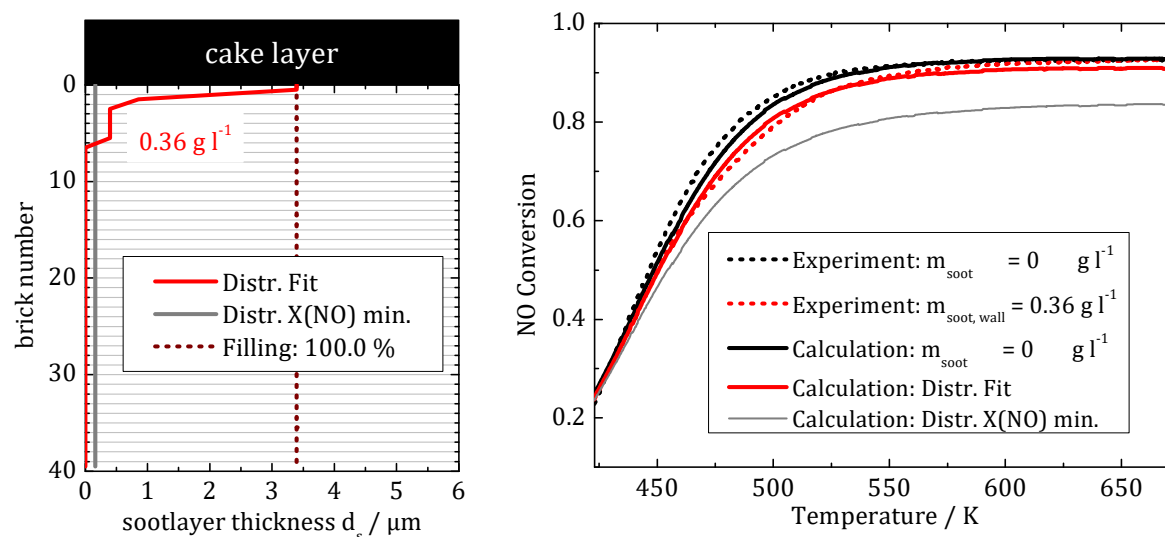


Fig. 55 Left: Spatial soot layer thickness distributions within the filter wall (divided into bricks) of $m_{\text{soot,wall}} = 0.36 \text{ g l}^{-1}$ explaining the NO conversion in a standard SCR experiment for SDPF2 (»Distr. fit«). Additionally, the soot distribution revealing the minimum NO conversion in model calculation is depicted. The dashed line ($d_s = 3.4 \mu\text{m}$) indicates the soot layer thickness for complete filling of the unit collectors for SDPF2. Right: NO conversion as a function of the temperature for standard SCR experiments (experimental conditions as in **Fig. 42**) on soot free and soot loaded ($m_{\text{soot,wall}} = 0.36 \text{ g l}^{-1}$) SDPF2 samples (dashed lines). The appropriate model calculations under usage of the soot distributions given on the left are depicted as solid lines.

5.3.5 Adaption to Flow-Through Catalysts

The effect of the soot, acting as diffusive barrier inside the porous filter wall, should be valid for any catalyst coated monoliths that are in contact with soot. To validate this, two flow-through catalysts have been studied. A commercial flow-through SCR-catalyst and a commercial NSC (specification given in **Tab. 3.1**) were slightly covered by soot. Thereby, the samples were kept in the exhaust gas stream of the soot-generator for 7.5 h (soot loading conditions as described in chapter 3.3.3). Compared to particulate filter samples, the flow-through catalysts reveal much less filtration efficiency (< 1). For flow-through catalysts »Interception« and »Brownian motion« (see chapter 2.3.2 or [115]) are expected to be the dominating deposition modes concerning small particles. Larger particles will have a very poor deposition rate due to their inertia. The loaded amount of soot within the catalyst was achieved by balancing (eq. (3.2)) the measured CO and CO₂ concentrations during forced soot oxidation (regeneration) afterwards the model gas experiments on NH₃ adsorption and NO conversion were finished. Compared to SDPF1 studied above ($m_{\text{soot,wall}} = 1 \text{ g l}^{-1}$) the loading of the SCR-catalyst $m_{\text{soot}} = 0.3 \text{ g l}^{-1}$ and of the NSC $m_{\text{soot}} = 0.2 \text{ g l}^{-1}$ are much smaller.

The results on NO and NO₂ adsorption for the soot free and the soot loaded NSC are shown in **Fig. 56**. Corresponding results on NH₃ adsorption on the SCR catalyst are depicted in **Fig. 57** (right). Both types of adsorption experiments revealed the onset of the adsorbate gas breakthrough during dosing to be shifted towards an earlier time-on-stream under soot loading. Furthermore, the breakthrough curve is flattened when the catalyst is covered by soot. Thus, for both flow-through catalysts (adsorbing NH₃ molecules or NO and NO₂ molecules respectively) the adsorption behavior was observed to be influenced in the same manner as for NH₃ on SDPF samples studied in chapter 5.3.3. Consequently, the principle of the soot acting as diffusive barrier for the gas transport to the active catalytic sites also holds for flow-through structured monoliths slightly covered with soot and is not a feature of NH₃ molecules only.

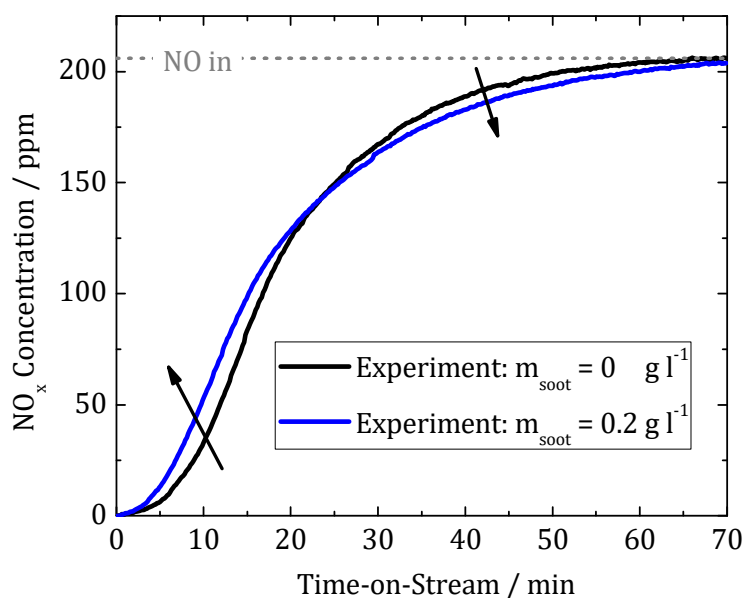


Fig. 56 Adsorption experiments on a flow-through NSC (given in Tab. 3.1). NO_x outlet concentration as a function of time-on-stream for soot free and soot loaded ($m_{\text{soot}} = 0.2 \text{ g l}^{-1}$) NSC. Experimental condition described in chapter 3.4.4 ($T_{\text{ads}} = 423 \text{ K}$). The arrows indicate the typical directions in which the adsorption curve shifts, when soot loaded.

For the SCR-catalyst the kinetic model, described in chapter 4 was applied to the flow-through structure. The model was adjusted and validated using model gas experiments on soot free samples. Both the NH₃ breakthrough during adsorption (**Fig. 57**, right, black lines) as well as the NO conversion light off (**Fig. 58**, black lines) are explained well by the kinetic model. For the soot free sample, the NH₃ breakthrough establishes after 22 min time-on-stream, whereas the soot loaded sample shows NH₃ slip even after only 15 min

of NH_3 dosing. For the NO conversion only a very minor influence of the soot loading is experimentally observed. The soot loaded SCR-catalyst shows 2 % reduction in catalytic activity. To consider the influence of soot, two soot distributions were studied (**Fig. 57**, left). A thin soot layer covering the entire catalytic surface ($0.05 \mu\text{m}$ thick, green line) and a soot distribution with local clusters (parts of the catalytic surface that are not covered by soot, red line). Comparing the model results on NH_3 adsorption for both distributions (**Fig. 57**, right), it can be seen that an entire soot covering of the catalyst yields a NH_3 breakthrough starting at the beginning of NH_3 dosing, which is not in accordance to the experiment. The clustered distribution leads to a NH_3 breakthrough after 15 min of full adsorption, representing the experimental results. Hence, a clustered distribution seems to be the more realistic scenario. Nevertheless, at 25 min time-on-stream and above the flattening of the calculated adsorption curves is much more evident compared to the experiment. The deviations might be a consequence of the deposition of very small soot particles (5 nm to 10 nm). These depositions may represent defective structures at the zeolite surface, which affect the molecular uptake rate of the zeolite as previously studied by Kontunov *et al.* [177]. A change in the zeolitic molecular uptake behavior under soot loading has not been implemented in the model, yet. Consequently, also the model calculation of the NO conversion of soot loaded SCR catalyst samples results in slight deviations to the experiment (**Fig. 58**). Nevertheless, the local distribution is more narrow to the experimental NO conversion under soot loading.

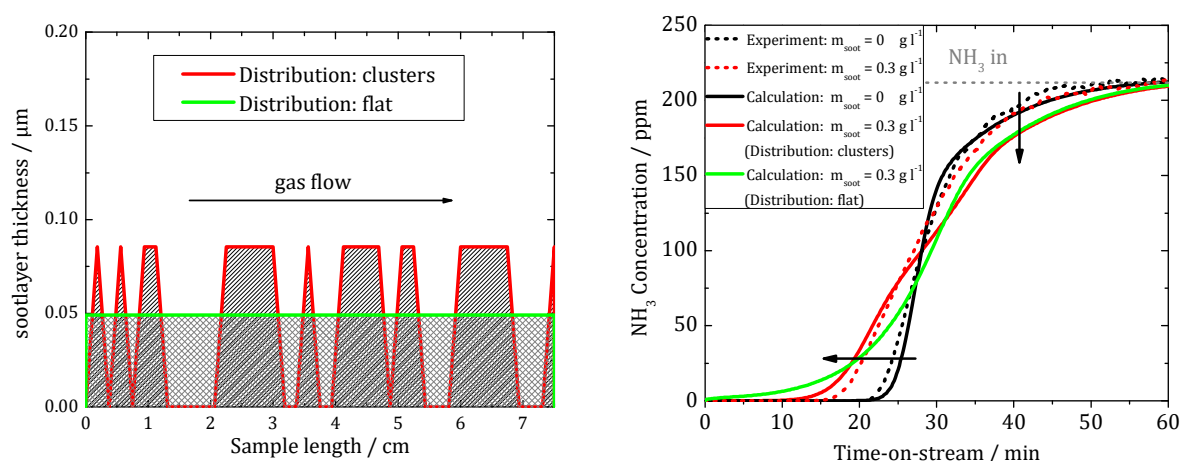


Fig. 57 Left: Soot distribution within the flow-through SCR-catalyst: soot layer thickness as a function of sample length for distribution locally covering the catalyst by clusters and a distribution covering the entire catalytic surface ($m_{\text{soot}} = 0.3 \text{ g l}^{-1}$). Right: Adsorption experiment on a flow-through SCR catalyst (given in Tab. 3.1). NH_3 outlet concentration during adsorption as a function of the time-on-stream for the SCR-catalyst in soot free and soot loaded ($m_{\text{soot}} = 0.3 \text{ g l}^{-1}$) condition. Experiments performed at conditions as described in chapter 3.4.2

(200 ppm NH_3 dosing in 40.000 h^{-1} GHSV, $T_{\text{ads}} = 423 \text{ K}$). The calculated curves are the result of a model calculation under usage of the soot distributions on the left.

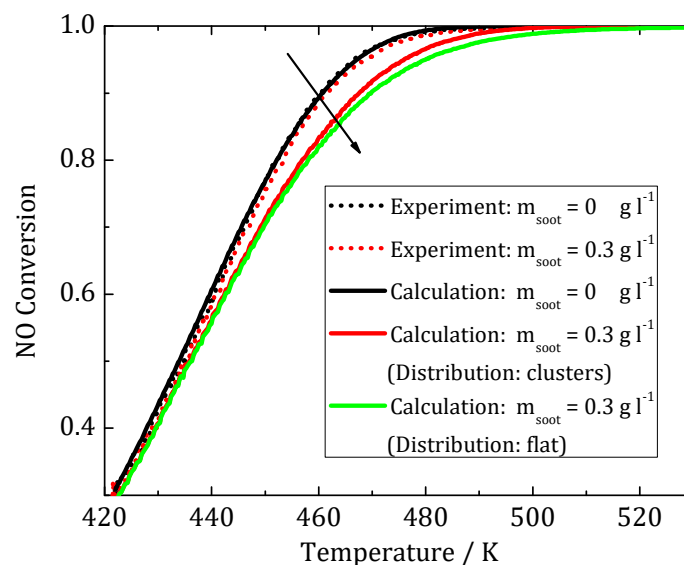


Fig. 58 Experimentally and calculated NO conversion as a function of temperature under usage of the soot distributions given in **Fig. 57** (left). The SCR experiments were performed under the conditions described in chapter 3.4.3 at GHSV of 40 k h^{-1} .

In case of NSC, the NO_x breakthrough behavior is affected in the same manner as the NH_3 breakthrough of SDPF samples under soot loading. The principle of the diffusive barrier is supported by Vaclavik *et al.* [178]. With the aim of investigating transport limitation in double-layer systems consisting of oxidation (DOC) and Lean NO_x Trap (LNT, NO_x storage) catalysts, the authors introduced a thin inert Al_2O_3 layer as diffusion barrier. It was placed on top of the washcoated channels inside a LNT. By means of model gas experiments on NO adsorption and C_3H_6 light-off, Vaclavik *et al.* have proven that transport limitation results from the diffusion barrier. The Al_2O_3 diffusion layer studied by Vaclavik *et al.* had a thickness of $\delta = 108 \mu\text{m}$. Its effective diffusivity was determined to be $D_{\text{eff}} = 3.5 \cdot 10^{-6} \text{ m}^2 \text{ s}^{-1}$ at 473 K . Thus, the corresponding characteristic diffusion time ($\delta^2/2D_{\text{eff}}$) results in 1.65 ms . For the soot layer studied here, a characteristic diffusion time of 0.95 ms could be evaluated for SDPF1, assuming a soot layer thickness of $0.6 \mu\text{m}$ (**Fig. 46**, left). Thus, the timescales of both diffusion barriers are in the same order of magnitude. As the conditions of their model gas experiments on NO_x adsorption are similar to those applied in this work, Vaclavik *et al.* similarly observed NO_x breakthrough at earlier time-on-stream during adsorbate supply, followed by a flattened breakthrough curve compared to the case without the Al_2O_3 diffusive barrier.

Within this subchapter, it was shown, that soot within the channels of flow-through catalysts provides a diffusion barrier, too. Next to the uptake of NH_3 molecules, also the NO molecules uptake is hindered by the soot, validating the diffusion barrier as a general principle.

6 Conclusions and Outlook

In recent years, a more stringent emission legislation for diesel engine vehicles combined with special demands on the packaging of the exhaust gas aftertreatment components has led the development of the diesel particulate filter coated with a catalyst for the selective catalytic reduction of NO_x with NH_3 (SDPF). The overlap of functionalities in one component, *e.g.* soot storage and NO_x reduction, comes along with an influence of the trapped soot on the catalytic properties, which is still controversially discussed in literature. Thus, aim of this work was a fundamental understanding of the physico-chemical interaction of soot on the NH_3 adsorption and NO_x conversion kinetics of SDPF samples.

For that purpose, a soot loading apparatus was set up to provide defined and reproducible soot loading of SDPF samples. Based on model gas experiments on soot free and soot loaded samples (up to 25 g l^{-1} soot), the influence of soot on the SCR DeNO_x behavior was studied. For the first time, a dramatic change in the NH_3 slip behavior (NH_3 breakthrough with onset of NH_3 dosing) in the presence of soot within the SDPF was observed by means of NH_3 adsorption/desorption experiments. A slightly increased NH_3 storage amount was found for soot loaded SDPF samples compared to soot free samples. The effect could be attributed to the soot itself, exhibiting additional acid sites which lead to an increase of the entire NH_3 storage capacity (22.5 mg of NH_3 per gram of model soot trapped in the filter). Temperature programmed standard SCR experiments in the temperature range of 423 K to 673 K revealed a decreased in NO conversion up to 20 % under soot loading.

With the aim of setting up a model for model based analysis of the influence of soot inside the SDPF on its catalytic activity, SEM measurements were performed for structural investigation of the soot loaded porous filter wall of SDPF samples. Based on the experimental observation a microscopic filter wall model was set up, implementing gas transport within the porous filter wall and through the wall trapped soot (wall represented by unit collector model) and a kinetic model. The established 1-D SDPF wall model describes the experimental observations on NH_3 breakthrough behavior and NO conversion drop very well. In this model, soot is implemented as a layer acting as physical diffusion barrier limiting the transport of the reactants to the washcoat surface (zeolite). This assumption is supported by the observation of a diffusion process of gas molecules through the wall trapped soot layer using PFG-NMR (unrestricted diffusion). The diffusion

through the soot strongly reduces the overall NH_3 adsorption- and SCR reaction-rates as the availability of reactant molecules is reduced but has no direct influence on the intrinsic adsorption or reaction kinetics of the washcoat itself (bottleneck principle). The considerable NO conversion drop between 3 % and 20 % experimentally found for SDPFs upon soot loading could be explained by means of variations in the soot distribution within the porous filter wall (soot located close to the inlet channel only vs. entirely covering all the chemically active sites). According to the model results of the present study, even a thin soot layer (0.6 μm) homogeneously covering the entire catalyst surface may reduce the NO conversion by up to 45 %. As consequence, any soot penetration inside the washcoated filter wall should be prevented by the SDPF design to maintain high NO_x conversion. Thus, a high backpressure will be avoided enabling improved fuel economy. As most of the soot is trapped inside the filter wall close to the inlet channel, a washcoating concept in which the washcoat is impregnated in the wall part close to the outlet channel is also advisable to prevent the soot to cover active sites reducing SCR De NO_x performance. The gained knowledge on the NH_3 slip behavior under soot loading may be helpful for application to improve reducing agent exploitation and economic performance of the exhaust gas aftertreatment system.

7 References

- [1] R.E. Hayes, S.T. Kolaczowski, Introduction to catalytic combustion, Gordon and Breach, Australia, 1997.
- [2] C. Brinkmeier, G. Eigenberger, J. Bernnat, U. Tuttlies, V. Schmeißer, F. Opferkuch, Chemie Ingenieur Technik 77 (2005) 1333-1355.
- [3] O. Deutschmann, J.-D. Grunwaldt, Chemie Ingenieur Technik 85 (2013) 595-617.
- [4] Robert Eschrich, Aging of Catalysts for Diesel Exhaust Aftertreatment on Multiple Timescales, Dissertation, Universität Leipzig, Leipzig, 2015.
- [5] G.P. Merker, C. Schwarz, R. Teichmann (Eds.), Grundlagen Verbrennungsmotoren: Funktionsweise, Simulation, Messtechnik, 5., vollständig überarbeitete, aktualisierte und erweiterte Auflage, 2011, Vieweg+Teubner Verlag / Springer Fachmedien Wiesbaden GmbH Wiesbaden, Wiesbaden, 2012.
- [6] Y.B. Zeldovich, Acta Physicochim. URSS 21 (1946) 577-628.
- [7] A. Stanislaus, A. Marafi, M.S. Rana, Catalysis Today 153 (2010) 1-68.
- [8] European Environment Agency, European Environment Agency (Ed.), European Union emission inventory report 1990–2014 under the UNECE Convention on Long-range Transboundary Air Pollution (LRTAP), 2016.
- [9] R.D. Stewart, J.E. Peterson, E.D. Baretta, R.T. Bachand, M.J. Hosko, A.A. Herrmann, Archives of Environmental Health: An International Journal 21 (1970) 154-164.
- [10] L.M. McKenzie, R.Z. Witter, L.S. Newman, J.L. Adgate, The Science of the total environment 424 (2012) 79-87.
- [11] P. Pacher, J.S. Beckman, L. Liaudet, Physiological reviews 87 (2007) 315-424.
- [12] B.C. Kone, American Journal of Kidney Diseases 30 (1997) 311-333.
- [13] J.D. Spengler, M. Brauer, P. Koutrakis, Environ. Sci. Technol. 24 (1990) 946-956.
- [14] J. Kagawa, Toxicology 181-182 (2002) 349-353.
- [15] A. Valavanidis, K. Fiotakis, T. Vlachogianni, J. Environ. Sci. Health. C Environ. Carcinog. Ecotoxicol. Rev. 26 (2008) 339-362.
- [16] K. Ravindra, A.K. Mittal, R. van Grieken, Reviews on environmental health 16 (2001) 169-189.
- [17] International Agency for Research on Cancer, others, IARC monographs on the evaluation of carcinogenic risks to humans 105 (1988).
- [18] International Agency for Research on Cancer (IARC), press release No. 213, Press Release, 12.06.2012.
- [19] D. Chatterjee, O. Deutschmann, J. Warnatz, Faraday Disc. 119 (2001) 371-384.
- [20] Z. Hu, C.Z. Wan, Y.K. Lui, J. Dettling, J.J. Steger, Catalysis Today 30 (1996) 83-89.
- [21] M. Zheng, G.T. Reader, J.G. Hawley, Energy Conversion and Management 45 (2004) 883-900.
- [22] Regulation (EG) No. 443/2009, Off. J. Eur. Union L 140 / 1 (2009).
- [23] Regulation (EU) No. 510/2011, Off. J. Eur. Union L 145 / 1 (2011).
- [24] Regulation (EG) No. 595/2009, Off. J. Eur. Union L 188 / 1 (2009).
- [25] Regulation (EU) No. 582/2011, Off. J. Eur. Union L 167 / 1 (2011).
- [26] Emission Standards for passenger cars and light commercial vehicle, available at <https://www.dieselnet.com/standards/eu/ld.php> (accessed on 10.07.2016).
- [27] Landesanstalt für Umwelt, Messungen und Naturschutz Baden-Württemberg (Ed.), PEMS-Messungen an drei Euro 6-Diesel-Pkw auf Streckenführungen in Stuttgart und München sowie auf Außerortsstrecken, 2015.
- [28] G.J. Thompson, D.K. Carder, M.C. Besch, A. Thiruvengadam, H.K. Kappana, Retrieved from the International Council on Clean Transportation website

- http://www.theicct.org/sites/default/files/publications/WVU_LDDV_in-use_ICCT_Report_Final_may2014.pdf (2014).
- [29] Umweltbundesamt (Ed.), Grenzwerte für Schadstoffemissionen für PKW, available at http://www.umweltbundesamt.de/sites/default/files/medien/378/bilder/dateien/2_tab_grenzwerte-pkw.pdf (accessed on 11.07.2016).
- [30] Kraftfahrt-Bundesamt, Kraftfahrt-Bundesamt (Ed.), Fahrzeugzulassungen (FZ): Neuzulassungen von Kraftfahrzeugen und Kraftfahrzeuganhängern - Monatsergebnisse, FZ 8.
- [31] Kraftfahrt-Bundesamt, Kraftfahrt-Bundesamt (Ed.), Fahrzeugzulassungen (FZ): Neuzulassungen von Kraftfahrzeugen nach Umwelt-Merkmalen, FZ 14, 2015.
- [32] R. Tatschl, J. Wurzenberger, in: G.P. Merker, R. Teichmann (Eds.), Grundlagen Verbrennungsmotoren: Funktionsweise, Simulation, Messtechnik, 7., vollst. überarb. Aufl. 2014, Springer Fachmedien Wiesbaden, Wiesbaden, 2014, pp. 749-773.
- [33] H.J. Stein, Applied Catalysis B: Environmental 10 (1996) 69-82.
- [34] S. Salomons, M. Votsmeier, R.E. Hayes, A. Drochner, H. Vogel, J. Gieshof, Catalysis Today 117 (2006) 491-497.
- [35] A. Winkler, D. Ferri, M. Aguirre, Applied Catalysis B: Environmental 93 (2009) 177-184.
- [36] A. Morlang, U. Neuhausen, K.V. Klementiev, F.-W. Schütze, G. Miehe, H. Fuess, E.S. Lox, Applied Catalysis B: Environmental 60 (2005) 191-199.
- [37] T.W. Beutel, J.C. Dettling, D.O. Hollobaugh, T.W. Mueller, Pt-Pd diesel oxidation catalyst with CO/HC light-off and HC storage function, Google Patents, 2009.
- [38] Y. Murata, T. Morita, K. Wada, H. Ohno, SAE Int. J. Fuels Lubr. 8 (2015).
- [39] P. Forzatti, L. Lietti, I. Nova, E. Tronconi, Catalysis Today 151 (2010) 202-211.
- [40] S. Roy, A. Baiker, Chemical reviews 109 (2009) 4054-4091.
- [41] F. Rodrigues, L. Juste, C. Potvin, J.F. Tempère, G. Blanchard, G. Djéga-Mariadassou, Catalysis Letters 72 (2001) 59-64.
- [42] W. Weisweiler, Chem.-Ing.-Tech. 72 (2000) 441-449.
- [43] J.P. Breen, M. Marella, C. Pistarino, J.R.H. Ross, Catalysis Letters 80 (2002) 123-128.
- [44] Y. Traa, B. Burger, J. Weitkamp, Microporous and Mesoporous Materials 30 (1999) 3-41.
- [45] M.D. Amiridis, T. Zhang, R.J. Farrauto, Applied Catalysis B: Environmental 10 (1996) 203-227.
- [46] M.K. Kim, P.S. Kim, H.J. Kwon, I.-S. Nam, B.K. Cho, S.H. Oh, Chemical Engineering Journal 209 (2012) 280-292.
- [47] M.K. Kim, P.S. Kim, J.H. Baik, I.-S. Nam, B.K. Cho, S.H. Oh, Applied Catalysis B: Environmental 105 (2011) 1-14.
- [48] A.M. Bernhard, D. Peitz, M. Elsener, A. Wokaun, O. Kröcher, Applied Catalysis B: Environmental 115-116 (2012) 129-137.
- [49] M. Colombo, I. Nova, E. Tronconi, Catalysis Today 151 (2010) 223-230.
- [50] H. Sjövall, R.J. Blint, L. Olsson, J. Phys. Chem. C 113 (2009) 1393-1405.
- [51] H. Sjövall, R.J. Blint, L. Olsson, Appl. Catal., B 92 (2009) 138-153.
- [52] P.S. Metkar, M.P. Harold, V. Balakotaiah, Chemical Engineering Science 87 (2013) 51-66.
- [53] K. Rahkamaa-Tolonen, T. Maunula, M. Lomma, M. Huuhtanen, R.L. Keiski, Catal. Today 100 (2005) 217-222.
- [54] A. Grossale, I. Nova, E. Tronconi, Catal. Lett. 130 (2009) 525-531.

- [55] I. Nova, C. Ciardelli, E. Tronconi, D. Chatterjee, B. Bandl-Konrad, *Catal. Today* 114 (2006) 3-12.
- [56] J.H. Baik, S.D. Yim, I.-S. Nam, Y.S. Mok, J.-H. Lee, B.K. Cho, S.H. Oh, *Topics in Catalysis* 30/31 (2004) 37-41.
- [57] N. Wilken, K. Wijayanti, K. Kamasamudram, N.W. Currier, R. Vedaiyan, A. Yezerets, L. Olsson, *Applied Catalysis B: Environmental* (2011).
- [58] A. Grossale, I. Nova, E. Tronconi, *Catal. Today* 136 (2008) 18-27.
- [59] X. WU, Z. SI, G. LI, D. WENG, Z. MA, *Journal of Rare Earths* 29 (2011) 64-68.
- [60] J. Li, H. Chang, L. Ma, J. Hao, R.T. Yang, *Catalysis Today* 175 (2011) 147-156.
- [61] X. Tang, J. Hao, W. Xu, J. Li, *Catalysis Communications* 8 (2007) 329-334.
- [62] J. PARK, H. PARK, J. BAIK, I. NAM, C. SHIN, J. LEE, B. CHO, S. Oh, *Journal of Catalysis* 240 (2006) 47-57.
- [63] A.-Z. Ma, W. Grünert, *Chem. Commun.* (1999) 71-72.
- [64] R.Q. Long, R.T. Yang, *J. Am. Chem. Soc.* 121 (1999) 5595-5596.
- [65] O. Kröcher, M. Devadas, M. Elsener, A. Wokaun, N. Söger, M. Pfeifer, Y. Demel, L. Musmann, *Appl. Catal., B* 66 (2006) 208-216.
- [66] G. Cavataio, J. Girard, J.E. Patterson, C. Montreuil, Y. Cheng, C.K. Lambert, in: *SAE World Congress & Exhibition, SAE International* 400 Commonwealth Drive, Warrendale, PA, United States, 2007.
- [67] P.S. Metkar, M.P. Harold, V. Balakotaiah, *Applied Catalysis B: Environmental* 111-112 (2012) 67-80.
- [68] L. Olsson, H. Sjövall, R.J. Blint, *Appl. Catal., B* 81 (2008) 203-217.
- [69] L. Olsson, H. Sjövall, R.J. Blint, *Appl. Catal., B* 87 (2009) 200-210.
- [70] H. Sjövall, L. Olsson, E. Fridell, R.J. Blint, *Appl. Catal., B* 64 (2006) 180-188.
- [71] H. Sjövall, R.J. Blint, A. Gopinath, L. Olsson, *Ind. Eng. Chem. Res.* 49 (2010) 39-52.
- [72] I. Nova, C. Ciardelli, E. Tronconi, D. Chatterjee, B. Bandl-Konrad, *AIChE J.* 52 (2006) 3222-3233.
- [73] A. Grossale, I. Nova, E. Tronconi, *J. Catal.* 265 (2009) 141-147.
- [74] S.J. Schmieg, S.H. Oh, C.H. Kim, D.B. Brown, J.H. Lee, C.H.F. Peden, D.H. Kim, *Catalysis Today* 184 (2012) 252-261.
- [75] L. Ma, Y. Cheng, G. Cavataio, R.W. McCabe, L. Fu, J. Li, *Chemical Engineering Journal* 225 (2013) 323-330.
- [76] J.H. Kwak, D. Tran, S.D. Burton, J. Szanyi, J.H. Lee, C.H.F. Peden, *J. Catal.* 287 (2012) 203-209.
- [77] J.H. Kwak, R.G. Tonkyn, D.H. Kim, J. Szanyi, C.H.F. Peden, *Journal of Catalysis* 275 (2010) 187-190.
- [78] T. Yu, J. Wang, M. Shen, W. Li, *Catal. Sci. Technol.* 3 (2013) 3234.
- [79] J. Xue, X. Wang, G. Qi, J. Wang, M. Shen, W. Li, *Journal of Catalysis* 297 (2013) 56-64.
- [80] K. Wijayanti, S. Andonova, A. Kumar, J. Li, K. Kamasamudram, N.W. Currier, A. Yezerets, L. Olsson, *Applied Catalysis B: Environmental* 166-167 (2015) 568-579.
- [81] D.W. Fickel, E. D'Addio, J.A. Lauterbach, R.F. Lobo, *Appl. Catal., B* 102 (2011) 441-448.
- [82] J.H. Kwak, D. Tran, J. Szanyi, C.H.F. Peden, J.H. Lee, *Catal. Lett.* 142 (2012) 295-301.
- [83] www.physitron.eu, Wall Flow Principle, available at http://www.physitron.eu/joomla_2/index.php/en/products/active-regeneration-strategy (accessed on 10.07.2016).
- [84] T. Mizutani, S. Iwasaki, Y. Miyairi, K. Yuuki, M. Makino, H. Kurachi, *SAE Technical Paper* 2010-01-0531.

- [85] K. Chen, K.S. Martirosyan, D. Luss, *Ind. Eng. Chem. Res.* 48 (2009) 3323-3330.
- [86] A. Yezerets, N.W. Currier, D.H. Kim, H.A. Eadler, W.S. Epling, C.H.F. Peden, *Appl. Catal., B* 61 (2005) 120-129.
- [87] K.S. Martirosyan, K. Chen, D. Luss, *Chem. Eng. Sci.* 65 (2010) 42-46.
- [88] H. Muroyama, S. Hano, T. Matsui, K. Eguchi, *Catalysis Today* 153 (2010) 133-135.
- [89] K. HINOT, H. BURTSCHER, A. WEBER, G. KASPER, *Appl. Catal., B* 71 (2007) 271-278.
- [90] A. Setiabudi, M. Makkee, J.A. Moulijn, *Appl. Catal., B* 50 (2004) 185-194.
- [91] Z. Liu, Y. Ge, J. Tan, C. He, A.N. Shah, Y. Ding, L. Yu, W. Zhao, *Journal of Environmental Sciences* 24 (2012) 624-631.
- [92] G. Pontikakis, *Modeling, Reaction Schemes and Kinetic Parameter Estimation in Automotive Catalytic Converters and Diesel Particulate Filters*, Dissertation, University of Thessaly, Thessaloniki, 2003.
- [93] Alexander Sappok, *The nature of lubricant-derived ash-related emissions and their impact on diesel aftertreatment system performance*, Dissertation, Massachusetts Institute of Technology, Massachusetts, 2009.
- [94] S. HONG, M. WOOLDRIDGE, H. IM, D. ASSANIS, H. PITTSCH, *Combust. Flame* 143 (2005) 11-26.
- [95] F. Mauss, B. Trilken, H. Breitbach, N. Peters, in: H. Bockhorn (Ed.), *Soot Formation in Combustion: Mechanisms and Models*, Springer, Berlin, Heidelberg, 1994, pp. 325-349.
- [96] M. Fiebig, M. Knauer, J. Schmid, N. Ivleva, H.-H. Grotheer, K. Hoffmann, C. Wahl, S. Pischinger, R. Nießner, M. Aigner, *FVV* (2011).
- [97] M. Freklach, H. Wang, in: H. Bockhorn (Ed.), *Soot Formation in Combustion: Mechanism and Model*, Springer-Verlag, Heidelberg, 1994.
- [98] J. Yang, M. Stewart, G. Maupin, D. Herling, A. Zelenyuk, *Chem. Eng. Sci.* 64 (2009) 1625-1634.
- [99] G. Falcucci, *Proc. IMechE Part D: J. Automobile Engineering* 226 (2012) 987-998.
- [100] S.J. Harris, M.M. Maricq, *Journal of Aerosol Science* 32 (2001) 749-764.
- [101] R.L. Vander Wal, A. Yezerets, N.W. Currier, D.H. Kim, C.M. Wang, *Carbon* 45 (2007) 70-77.
- [102] T. Lu, Z. Huang, C.S. Cheung, J. Ma, *The Science of the total environment* 438 (2012) 33-41.
- [103] J. Neeft, *Fuel* 76 (1997) 1129-1136.
- [104] R.H. Moore, L.D. Ziemba, D. Dutcher, A.J. Beyersdorf, K. Chan, S. Crumeyrolle, T.M. Raymond, K.L. Thornhill, E.L. Winstead, B.E. Anderson, *Aerosol Science and Technology* 48 (2014) 467-479.
- [105] M. Knauer, M. Carrara, D. Rothe, R. Niessner, N.P. Ivleva, *Aerosol Science and Technology* 43 (2009) 1-8.
- [106] M. Knauer, M.E. Schuster, D. Su, R. Schlögl, R. Niessner, N.P. Ivleva, *J. Phys. Chem. A* 113 (2009) 13871-13880.
- [107] N. Blatt, *Characterisation of Soot Aerosols by thermal Analysis*, Diploma Thesis, Karlsruhe Institute of Technology, Karlsruhe, 2002.
- [108] J.C. Caroca, F. Millo, D. Vezza, T. Vlachos, A. de Filippo, S. Bensaid, N. Russo, D. Fino, *Ind. Eng. Chem. Res.* 50 (2011) 2650-2658.
- [109] Rainer Stefan Peck, *Experimentelle Untersuchung und dynamische Simulation von Oxidationskatalysatoren und Diesel-Partikelfilter*, Dissertation, Universität Stuttgart, Stuttgart, 2006.
- [110] E. Wirojsakunchai, E. Schroeder, C. Kolodziej, D.E. FOSTER, N. Schmidt, T. Root, T. Kawai, T. Suga, T. Nevius, T. Kusaka, *SAE Technical Paper* 2007-01-0320.

- [111] J. Adler, *Int. J. Appl. Ceram. Technol.* 2 (2005) 429-439.
- [112] Rolf Brück, Peter Hirth, Meike Reizig, Peter Treiber, Jürgen Breuer, SAE Technical Paper (2001).
- [113] S. Bensaid, D.L. Marchisio, N. Russo, D. Fino, *Catal. Today* 147 (2009) 295-300.
- [114] R. Sanui, K. Hanamura, SAE Technical Paper 2015-01-1018.
- [115] D. Psarianos, Development of a System for the Measurement of Soot Maldistribution and Pressure Drop Characteristics in Diesel Particulate filters, Postgraduate Specialization Thesis, University of Thessaly, Thessaloniki, 2002.
- [116] Dimitri L. Psarianos, Development of a System for the Measurement for Soot Maldistribution and Pressure Drop Characteristics in Diesel Particulate Filters.
- [117] N.V. Heeb, R. Haag, C. Seiler, P. Schmid, M. Zennegg, A. Wichser, A. Ulrich, P. Honegger, K. Zeyer, L. Emmenegger, Y. Zimmerli, J. Czerwinski, M. Kasper, A. Mayer, *Environ. Sci. Technol.* 46 (2012) 13317-13325.
- [118] A. Mayer, A. Ulrich, N.V. Heeb, J. Czerwinski, T. Neubert, in: SAE World Congress & Exhibition, SAE International 400 Commonwealth Drive, Warrendale, PA, United States, 2008.
- [119] J.J. Swanson, W.F. Watts, R.A. Newman, R.R. Ziebarth, D.B. Kittelson, *Environ. Sci. Technol.* 47 (2013) 4521-4527.
- [120] G.C. Koltsakis, T. Bollerhoff, Z. Samaras, I. Markomanolakis, SAE Technical Paper 2012-01-1298.
- [121] G.A. Merkel, T. Tao, W.A. Cutler, A. Chiffey, P.R. Phillips, M.V. Twigg, A.P. Walker, in: Proceedings of the 6th International Congress on Catalysis and Automotive Pollution Control 2003.
- [122] K. Yamamoto, S. Oohori, H. Yamashita, S. Daido, *P. Combust. Inst.* 32 (2009) 1965-1972.
- [123] R.A. Yapaulo, E. Wirojsakunchai, T. Orita, D.E. Foster, M. Akard, L.R. Walker, M.J. Lance, *Int. J. Engine Res.* 10 (2009) 287-304.
- [124] A.G. Konstandopoulos, M. Kostoglou, E. Skaperdas, E. Papaioannou, et al., Fundamental Studies of Diesel Particulate Filters: Transient Loading, Regeneration and Aging, SAE International, Warrendale, PA, 2000.
- [125] O.A. Haralampous, I.P. Kandylas, G.C. Koltsakis, Z.C. Samaras, *Int. J. Engine Res.* 5 (2004) 149-162.
- [126] J.R. Serrano, F.J. Arnau, P. Piqueras, Ó. García-Afonso, *Energy* 58 (2013) 644-654.
- [127] A.G. Konstandopoulos, SAE Technical Paper 2003-01-0846.
- [128] W.W. Pulkrabek, W.E. Ibele, *International Journal of Heat and Mass Transfer* 30 (1987) 1103-1109.
- [129] A.G. Konstandopoulos, E. Skaperdas, M. Masoudi, SAE Technical Paper 2002-01-1015.
- [130] T.J. Toops, J.A. Pihl, C.E.A. Finney, J. Gregor, H. Bilheux, *Emiss. Control Sci. Technol.* 1 (2015) 24-31.
- [131] G. Smedler, O. Sonntag, P. Marsh, M. Decker, in: J. Liebl, C. Beidl (Eds.), *Internationaler Motorenkongress 2016: Mit Konferenz Nfz-Motorentechnologie*, Springer Fachmedien Wiesbaden, Wiesbaden, 2016, pp. 709-724.
- [132] X. Song, J.H. Johnson, J.D. Naber, *Int. J. Engine Res.* 2014.
- [133] S. Bensaid, V. Balakotaiah, D. Luss, *AIChE J.* 63 (2017) 238-248.
- [134] S. Olowojebutu, T. Steffen, in: SAE International 400 Commonwealth Drive, Warrendale, PA, United States, 2017.
- [135] F. Schrade, M. Brammer, J. Schaeffner, K.-J. Langeheinecke, L. Kraemer, *SAE Int. J. Engines* 5 (2012) 958-974.

- [136] O. Mihai, S. Tamm, M. Stenfeldt, C. Wang-Hansen, L. Olsson, *Ind. Eng. Chem. Res.* 54 (2015) 11779-11791.
- [137] G. Cavataio, J.R. Warner, J.W. Girard, J. Ura, D. Dobson, C.K. Lambert, *SAE Int. J. Fuels Lubr.* 2 (2009) 342-368.
- [138] F. Marchitti, I. Nova, E. Tronconi, *Catalysis Today* (2016).
- [139] E. Tronconi, I. Nova, F. Marchitti, G. Koltsakis, D. Karamitros, B. Maletic, N. Markert, D. Chatterjee, M. Hehle, *Emiss. Control Sci. Technol.* 1 (2015) 134-151.
- [140] K.G. Rappé, *Ind. Eng. Chem. Res.* 53 (2014) 17547-17557.
- [141] J. Tan, C. Solbrig, S.J. Schmieg, *SAE Technical Paper* 2011-01-1140.
- [142] O. Mihai, S. Tamm, M. Stenfeldt, L. Olsson, *Phil. Trans. R. Soc. A* 374 (2016) 20150086.
- [143] M. Mehring, M. Elsener, O. Kröcher, *ACS Catal.* 2 (2012) 1507-1518.
- [144] Y. Yang, G. Cho, C. Rutland, *SAE Technical Paper* 2015-01-1060.
- [145] S.-Y. Park, K. Narayanaswamy, S.J. Schmieg, C.J. Rutland, *Ind. Eng. Chem. Res.* 51 (2012) 15582-15592.
- [146] Sergej Naumov, *Hysteresis Phenomena in Mesoporous Materials*, Dissertation, Universität Leipzig, Leipzig, 2009.
- [147] Jörg Kärger, Harry Pfeifer, Wilfried Heink, *Advances in Magnetic and Optical Resonance* 12 (1988) 1-89.
- [148] F. Stallmach, P. Galvosas, in: G.A. Webb (Ed.), *Annual reports on NMR spectroscopy*, Academic Press, London, New York, 2007, pp. 51-131.
- [149] O. Geier, *J. Catal.* 213 (2003) 321-323.
- [150] R.M. Cotts, M.J.R. Hoch, T. Sun, J.T. Markert, *Journal of Magnetic Resonance* (1969) 83 (1989) 252-266.
- [151] Lianpeng Jing, *OFMET Info* (Ed.), *Neuer Russgenerator für Verbrennungsrussteilchen zur Kalibrierung von Partikelmessgeräten*, 7th edition, 2000.
- [152] S. Bensaid, D.L. Marchisio, D. Fino, G. Saracco, V. Specchia, *Chem. Eng. J.* 154 (2009) 211-218.
- [153] R. Eschrich, J. Schröder, F. Hartman, R. Gläser, *MTZ Motortech Z* 76 (2015) 68-75.
- [154] J. Gong, K. Narayanaswamy, C.J. Rutland, *Ind. Eng. Chem. Res.* 55 (2016) 5874-5884.
- [155] M. Koebel, M. Elsener, *Chemical Engineering Science* 53 (1998) 657-669.
- [156] H.H. Rosenbrock, *The Computer Journal* 5 (1963) 329-330.
- [157] M.M. Maricq, N. Xu, *Journal of Aerosol Science* 35 (2004) 1251-1274.
- [158] M. Mehring, M. Elsener, O. Kröcher, *Top. Catal.* 56 (2013) 440-445.
- [159] R. Valiullin, P. Kortunov, J. Korger, V. Timoshenko, *The Journal of chemical physics* 120 (2004) 11804-11814.
- [160] M. Dvoyashkin, A. Khokhlov, S. Naumov, R. Valiullin, *Microporous and Mesoporous Materials* 125 (2009) 58-62.
- [161] V.J. Inglezakis, *Microporous and Mesoporous Materials* 103 (2007) 72-81.
- [162] S.G. Chen, R.T. Yang, *Langmuir* 10 (1994) 4244-4249.
- [163] A. Gil, P. Grange, *Colloids and Surfaces A: Physicochemical and Engineering Aspects* 113 (1996) 39-50.
- [164] D.H. Olson, G.T. Kokotailo, S.L. Lawton, W.M. Meier, *J. Phys. Chem.* 85 (1981) 2238-2243.
- [165] Ammonia Vapor Pressure & Temperature Equations, available at <http://profmaster.blogspot.de/2009/08/ammonia-vapor-pressure-temperature.html> (accessed on 22.08.2016).
- [166] Y.H. Hu, E. Ruckenstein, *Chem. Phys. Lett.* 425 (2006) 306-310.

- [167] M.M. DUBININ, V.A. ASTAKHOV, in: E.M. Flanigen (Ed.), *Molecular sieve zeolites: The second international conference co-sponsored by the Division of Colloid and Surface Chemistry ... at Worcester Polytechnic Institute, Worcester, Mass., Sept. 8-11, 1970*, American Chemical Soc, Washington, DC, 1971, pp. 69-85.
- [168] G.O. Wood, *Carbon* 39 (2001) 343-356.
- [169] F. Millo, M. Rafigh, D. Fino, P. Miceli, *Fuel* 198 (2017) 183-192.
- [170] C. Ciardelli, I. Nova, E. Tronconi, D. Chatterjee, B. Bandl-Konrad, M. Weibel, B. Krutzsch, *Appl. Catal., B* 70 (2007) 80-90.
- [171] G. Busca, *Appl. Catal., B* 18 (1998) 1-36.
- [172] G.A. Stratakis, D.L. Psarianos, A.M. Stamatelos, *Proc. IMechE Part D: J. Automobile Engineering* 216 (2002) 773-784.
- [173] S.-Y. Park, C.J. Rutland, K. Narayanaswamy, S.J. Schmieg, Y.-S. He, D.B. Brown, *Proc. IMechE Part D: J. Automobile Engineering* 225 (2011) 1641-1659.
- [174] F. Furtado, P. Galvosas, M. Gonçalves, F.-D. Kopinke, S. Naumov, F. Rodríguez-Reinoso, U. Roland, R. Valiullin, J. Kärger, *J. Am. Chem. Soc.* 133 (2011) 2437-2443.
- [175] K. Yamamoto, K. Yamauchi, *P. Combust. Inst.* 34 (2013) 3083-3090.
- [176] G.C. Koltsakis, A. Konstantinou, O.A. Haralampous, Z.C. Samaras, in: *SAE 2006 World Congress & Exhibition*, SAE International 400 Commonwealth Drive, Warrendale, PA, United States, 2006.
- [177] P. Kortunov, S. Vasenkov, C. Chmelik, J. Kärger, D.M. Ruthven, J. Wloch, *Chem. Mater.* 16 (2004) 3552-3558.
- [178] M. Václavík, V. Novák, J. Březina, P. Kočí, G. Gregori, D. Thompsett, *Catalysis Today* (2016).

8 Appendix

8.1 Additional Data

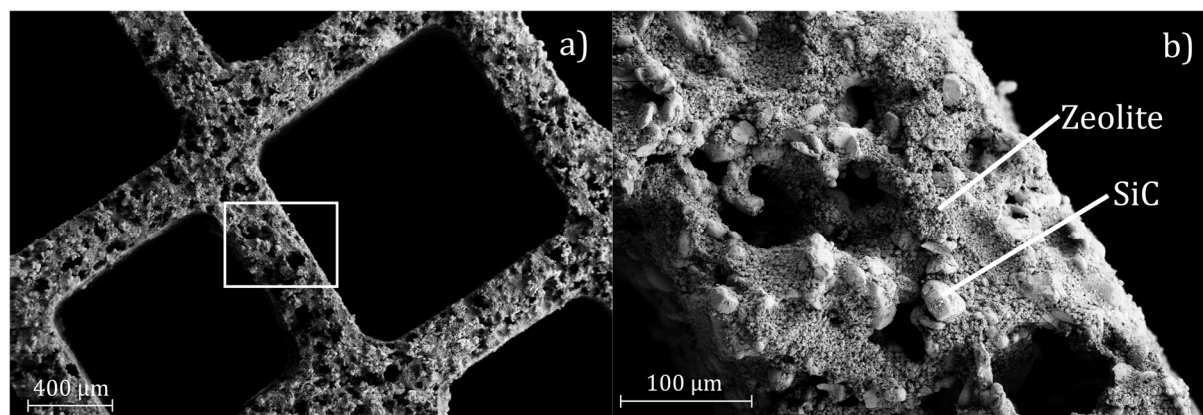


Fig. 59 SEM images of the cross section of some SDPFs filter channels, left: cross section of the filter channels with 40 times magnification, right: porous filter wall cross section at 250 times magnification revealing the areas of the SiC filter material and the zeolite containing washcoat.

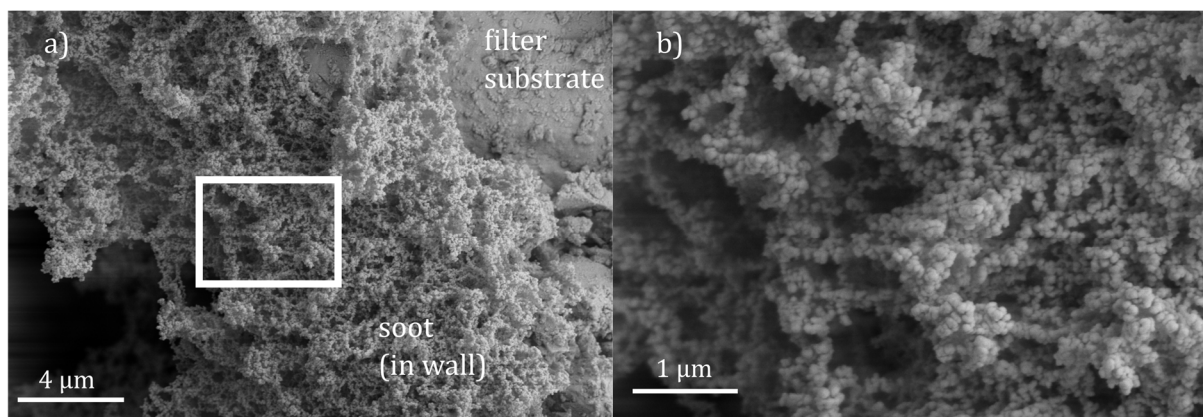


Fig. 60 Left: SEM image of the cross section of a soot loaded SDPFs filter wall at 5.000 times magnification. Right SEM image of the soot deposit within the porous filter wall at 20.000 times magnification.

Tab. 8.1 List of the whole set of mass balance equations used in the kinetic model. The kinetic parameters (pre-exponential factors, activation energies and storage capacities) for each reaction are given in the bottom part of the table.

Mass Conservation Equations

NH₃

$$\begin{aligned}\frac{dx_{g,NH_3}}{dt} &= \frac{\dot{V}}{n_{cell}V_{void}}(x_{in,NH_3} - x_{g,NH_3}) - \beta_{NH_3} \frac{A_s}{V_{void}}(x_{g,NH_3} - x_{s,NH_3}) \\ \frac{dx_{s,NH_3}}{dt} &= \beta_{NH_3} \frac{A_s}{V_{s,layer}}(x_{g,NH_3} - x_{s,NH_3}) - \frac{A_{wc}}{V_{s,layer}} \frac{D_{eff,NH_3}}{d_s}(x_{s,NH_3} - x_{wc,NH_3}) \\ \frac{dx_{wc,NH_3}}{dt} &= \frac{A_{wc}}{V_{wc}} \frac{D_{eff,NH_3}}{d_s}(x_{s,NH_3} - x_{wc,NH_3}) - k_{s1,ads}(1 - \theta_{s1})x_{wc,NH_3} + k_{s1,des}\theta_{s1} \\ &\quad - k_{s2,ads}(1 - \theta_{s2})x_{wc,NH_3} + k_{s2,des}\theta_{s2} - k_{s3,ads}(1 - \theta_{s3})x_{wc,NH_3} \\ &\quad + k_{s3,des}\theta_{s3} \\ \frac{d\theta_{s1}}{dt} &= \frac{c_{id,gas}}{\Gamma_{s1}}(k_{s1,ads}(1 - \theta_{s1})x_{wc,NH_3} - k_{s1,des}\theta_{s1}) \\ \frac{d\theta_{s2}}{dt} &= \frac{c_{id,gas}}{\Gamma_{s2}}\left(k_{s2,ads}(1 - \theta_{s2})x_{wc,NH_3} - k_{s2,des}\theta_{s2} - \frac{k_{s2,StdSCR}\theta_{s2}x_{wc,NO}x_{wc,O_2}}{G_{s2,Inhib}} - \right. \\ &\quad \left. k_{s2,NH_3Oxi}\theta_{s2}x_{wc,O_2}\right) \\ \frac{d\theta_{s3}}{dt} &= \frac{c_{id,gas}}{\Gamma_{s3}}\left(k_{s3,ads}(1 - \theta_{s3})x_{wc,NH_3} - k_{s3,des}\theta_{s3} - \frac{k_{s3,StdSCR}\theta_{s3}x_{wc,NO}x_{wc,O_2}}{G_{s3,Inhib}} - \right. \\ &\quad \left. k_{s3,NH_3Oxi}\theta_{s3}x_{wc,O_2}\right)\end{aligned}$$

NO

$$\begin{aligned}\frac{dx_{g,NO}}{dt} &= \frac{\dot{V}}{n_{cell}V_{void}}(x_{in,NO} - x_{g,NO}) - \beta_{NO} \frac{A_s}{V_{void}}(x_{g,NO} - x_{s,NO}) \\ \frac{dx_{s,NO}}{dt} &= \beta_{NO} \frac{A_s}{V_{s,layer}}(x_{g,NO} - x_{s,NO}) - \frac{A_{wc}}{V_{s,layer}} \frac{D_{eff,NO}}{d_s}(x_{s,NO} - x_{wc,NO}) \\ \frac{dx_{wc,NO}}{dt} &= \frac{A_{wc}}{V_{wc}} \frac{D_{eff,NO}}{d_s}(x_{s,NO} - x_{wc,NO}) - \frac{k_{s2,StdSCR}\theta_{s2}x_{wc,NO}x_{wc,O_2}}{G_{s2,Inhib}} \\ &\quad - \frac{k_{s3,StdSCR}\theta_{s3}x_{wc,NO}x_{wc,O_2}}{G_{s3,Inhib}}\end{aligned}$$

O₂

$$\begin{aligned}
\frac{dx_{g,O_2}}{dt} &= \frac{\dot{V}}{n_{cell} V_{void}} (x_{in,O_2} - x_{g,O_2}) - \beta_{O_2} \frac{A_s}{V_{void}} (x_{g,O_2} - x_{s,O_2}) \\
\frac{dx_{s,O_2}}{dt} &= \beta_{O_2} \frac{A_s}{V_{s,layer}} (x_{g,O_2} - x_{s,O_2}) - \frac{A_{wc}}{V_{s,layer}} \frac{D_{eff,O_2}}{d_s} (x_{s,O_2} - x_{wc,O_2}) \\
\frac{dx_{wc,O_2}}{dt} &= \frac{A_{wc}}{V_{wc}} \frac{D_{eff,O_2}}{d_s} (x_{s,O_2} - x_{wc,O_2}) - \frac{1}{4} \frac{k_{s2,StdSCR} \theta_{s2} x_{wc,NO} x_{wc,O_2}}{G_{s2,Inh}ib} \\
&\quad - \frac{1}{4} \frac{k_{s3,StdSCR} \theta_{s3} x_{wc,NO} x_{wc,O_2}}{G_{s3,Inh}ib} - \frac{3}{4} k_{s2,NH3Oxi} \theta_{s2} x_{wc,O_2} \\
&\quad - \frac{3}{4} k_{s3,NH3Oxi} \theta_{s3} x_{wc,O_2}
\end{aligned}$$

Kinetic Model Parametrisation of Sample SDPF1

Pre-exponential factor A_i / s ⁻¹	Activation energy E_A / kJ mol ⁻¹
$A_{s1,ads} = 1.1 \cdot 10^5$	$E_{A,s1,ads} = 0$
$A_{s1,des} = 3.7 \cdot 10^0$	$E_{A,s1,des} = 0$
$A_{s2,ads} = 2.8 \cdot 10^3$	$E_{A,s2,ads} = 0$
$A_{s2,des} = 2.3 \cdot 10^5$	$E_{A,s2,des} = 76.7$
$A_{s3,ads} = 3.2 \cdot 10^2$	$E_{A,s3,ads} = 0$
$A_{s3,des} = 1.1 \cdot 10^6$	$E_{A,s3,des} = 66.5$
$A_{s2,StdSCR} = 1.2 \cdot 10^{12}$	$E_{A,s2,StdSCR} = 73.7$
$A_{s2,Inh}ib = 5.5 \cdot 10^7$ (no unit)	$E_{A,s2,Inh}ib = 73.7$
$A_{s2,NH3Oxi} = 1.7 \cdot 10^6$	$E_{A,s2,NH3Oxi} = 77.7$
$A_{s3,StdSCR} = 6.8 \cdot 10^{11}$	$E_{A,s3,StdSCR} = 70.5$
$A_{s3,Inh}ib = 1.0 \cdot 10^8$ (no unit)	$E_{A,s3,Inh}ib = 70.5$
$A_{s3,NH3Oxi} = 2.9 \cdot 10^7$	$E_{A,s3,NH3Oxi} = 72.3$

NH ₃ storage capacity of Γ_j / mol m ⁻³ _{wc}
$\Gamma_1 = 1.37 \cdot 10^3$
$\Gamma_2 = 3.03 \cdot 10^3$
$\Gamma_3 = 3.40 \cdot 10^3$

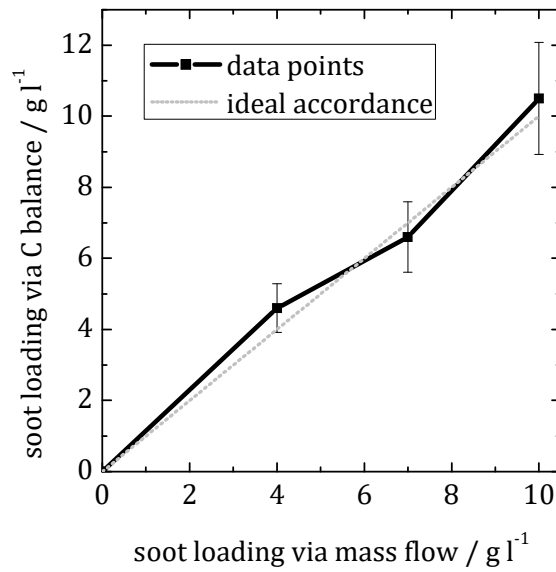


Fig. 61 Comparison of methods for calculating the soot loaded mass of the SDPF: evaluated soot loading via carbon balance from FTIR signal (eq. (3.2)) as a function of the evaluated soot loading calculated via soot mass flow. The error bars indicate an uncertainty of 15 % for the evaluation via C balance, as the FTIR under usage only measures the CO₂ concentration in vol.-% while the CO concentration could be measured in ppm. The grey line is a guide for the eye for an ideal accordance of both methods.

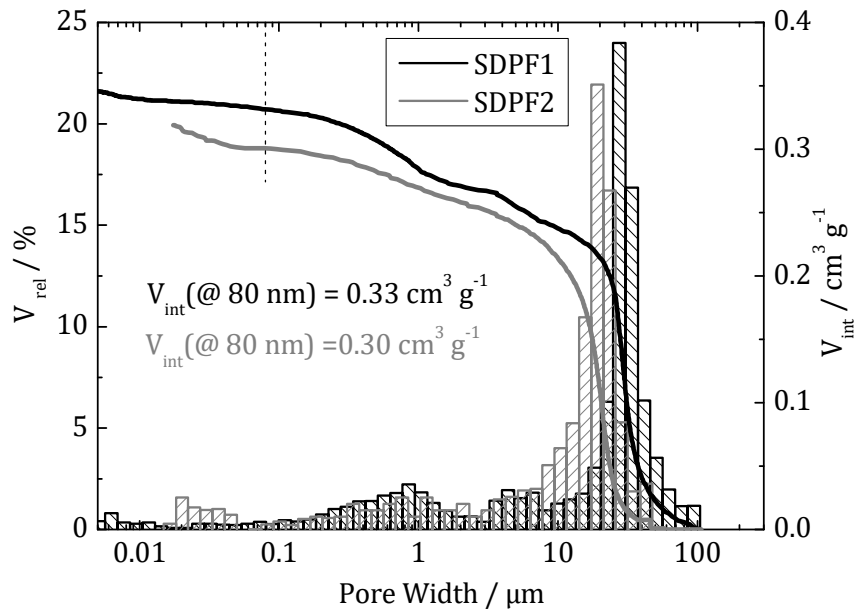


Fig. 62 Relative volume (V_{rel}) and volume intruded (V_{int}) as a function of pore width for the Hg-intrusion profile and pore width distribution histogram of SDPF1 (black) and SDPF2 (grey). The intruded volumina up to 80 nm pore width is given as numbers (due to particle size **Fig. 28**, smaller pores are unlikely to be filled with soot particles).

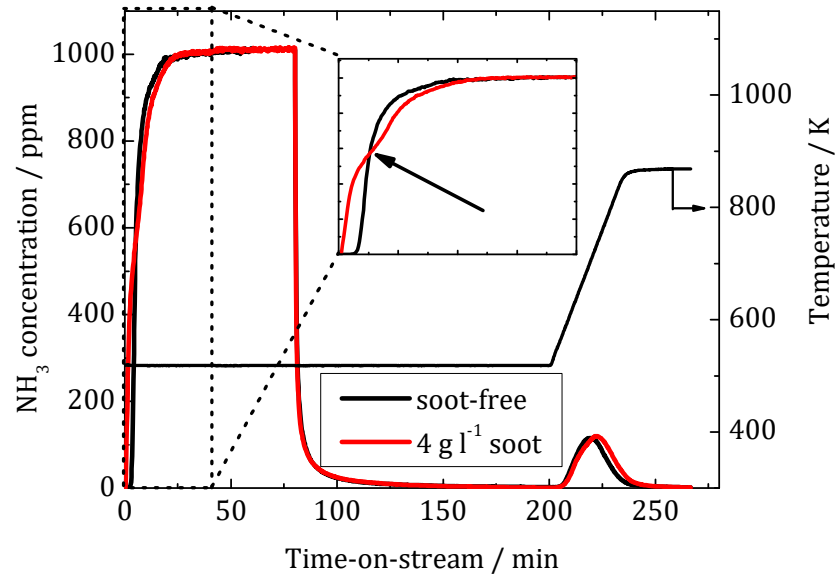


Fig. 63 NH₃ concentration at the reactor outlet as a function of time-on-stream for NH₃ adsorption and desorption experiments of a soot free and a soot loaded ($m_{\text{soot}} = 4 \text{ g l}^{-1}$) SDPF sample. A stream of NH₃ (1000 ppm) in N₂ was led through the reactor at 523 K adsorption temperature until 80 min on-stream (GHSV = 40.000 h⁻¹). Then, a pure nitrogen flow was applied and after 200 min on-stream the temperature was increased linearly until 873 K for NH₃ desorption. The arrow in the insert indicates the inflection point for the soot loaded sample.

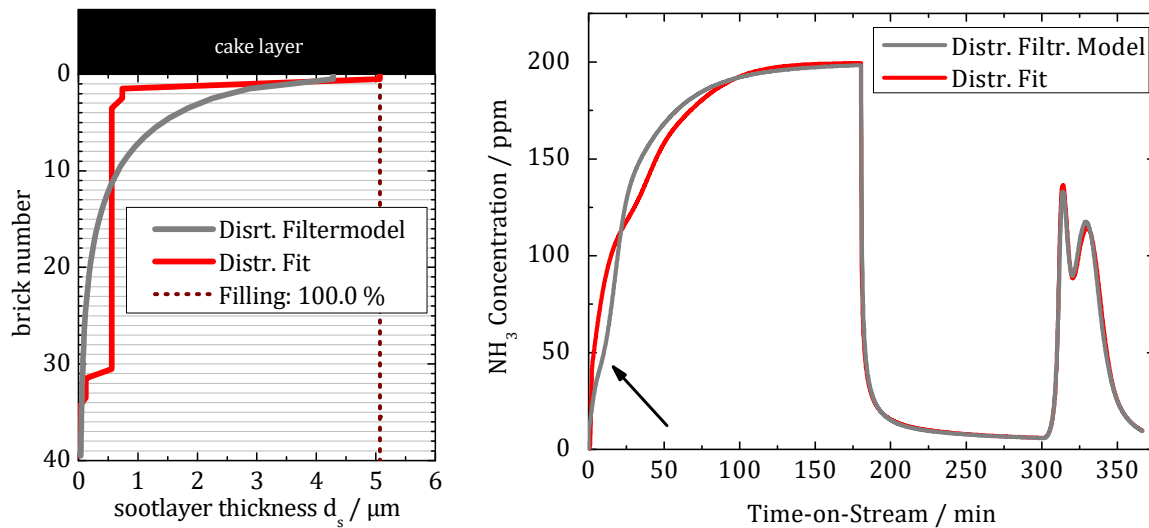


Fig. 64 Left: Spatial soot layer thickness distributions of $m_{\text{soot,wall}} = 1 \text{ g l}^{-1}$. The black line is the »fit distribution« (explained in chapter 5.3.3), the grey lines gives a distribution using the filtration model proposed by Konstandopoulos *et al.* [124]. Right: NH₃ concentration as a function of time-on-stream for model calculations of NH₃ adsorption/desorption under usage of the soot distributions given on the left. The arrow indicates the position of the inflection point using the filtration model distribution.

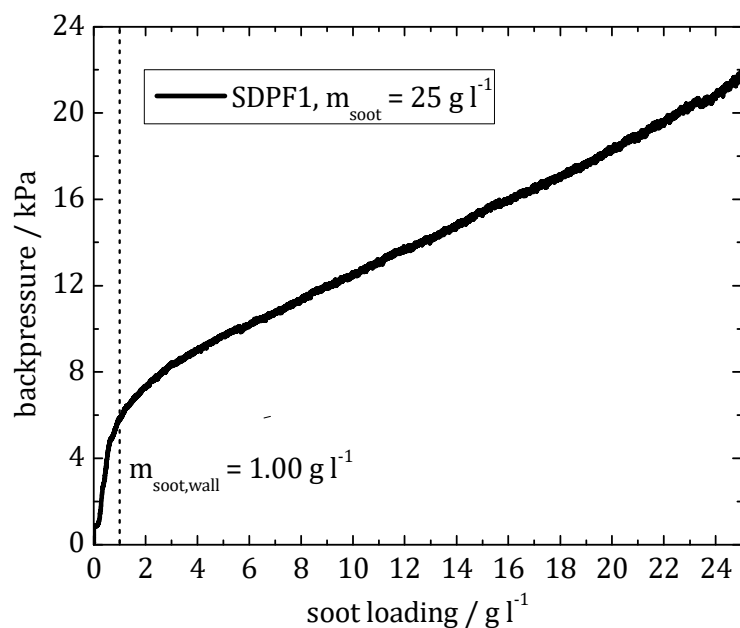


Fig. 65 Backpressure as a function of soot loading (in g l^{-1}) for SDPF1 sample at the high loading test with $m_{\text{soot}} = 25 \text{ g l}^{-1}$. The dashed line gives the transition from deep bed to cake filtration at $m_{\text{soot, wall}} = 1 \text{ g l}^{-1}$.

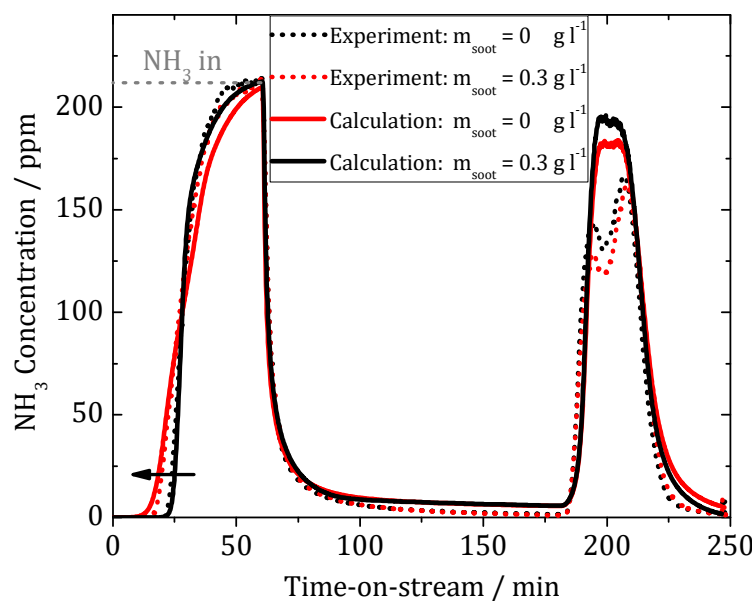


Fig. 66 NH_3 concentration as a function of time-on-stream for a NH_3 adsorption/desorption experiment on the flow-through SCR-catalyst. The dotted lines are the experimental data, whereas the solid lines are the result of kinetic model calculation. The experimental conditions are described in chapter 3.4.2 ($\text{GHSV} = 40 \text{ k h}^{-1}$ and $T_{\text{ads}} = 423 \text{ K}$).

Tab. 8.2 Table of the soot-generator operation points tested in this study by means of particle size distribution and soot mass flow.

	C_3H_8	Air	λ	N_2	N_2	Dilution	Mean	Standard.	Particle	Soot Mass	Standard
				Mix Gas	Quench Gas	Air	Particle Size	Deviation	Concentration	Flow	Deviation
	ml min ⁻¹	l min ⁻¹	-	ml min ⁻¹	l min ⁻¹	l min ⁻¹	nm	nm	#/cm ³	mg h ⁻¹	mg h ⁻¹
OP1	60	1.55	1.059	0	7	20	95.9	1.1	1.11E+08	124.1	1.8
OP2	60	1.52	1.039	100	7	20	80.2	1.1	1.20E+08	67.9	1.6
OP3	60	1.47	1.005	200	7	20	64.2	1.1	1.49E+08	34.6	0.5
OP4	60	1.42	0.970	250	7	20	47.7	1.1	1.28E+08	13.5	0.2
OP5	60	1.36	0.929	300	7	20	26.2	1.2	9.32E+07	1.1	0.0
OP6	60	1.32	0.902	330	7	20	18.7	1.3	6.38E+07	0.2	0.0
OP7	60	1.25	0.854	330	7	20	16.4	1.4	4.98E+07	0.1	0.0
OP8	60	1.55	1.059	50	7	20	88.2	1.1	1.14E+08	70.9	3.0
OP9	60	1.55	1.059	150	7	20	70.4	1.1	1.12E+08	27.1	0.4
OP10	60	1.55	1.059	250	7	20	50.8	1.2	8.73E+07	5.8	0.1
OP11	60	1.6	1.093	0	7	20	94.7	1.1	1.01E+08	88.6	1.7
OP12	60	1.7	1.162	0	7	20	83.5	1.1	7.44E+07	40.8	1.2
OP13	60	1.8	1.230	0	7	20	65.1	1.2	3.84E+07	5.4	0.3
OP14	60	1.8	1.230	100	7	20	37.5	2.5	6.07E+06	0.0	0.0
OP15	60	1.9	1.298	0	7	20	38.0	2.4	6.00E+06	0.2	0.0
OP16	60	1.57	1.073	0	7	20	99.4	1.1	1.06E+08	107.8	1.6
OP17	60	1.57	1.073	100	7	20	79.6	1.1	1.08E+08	42.2	0.9
OP18	60	1.57	1.073	200	7	20	61.2	1.2	9.58E+07	12.5	0.4
OP19	60	1.57	1.073	300	7	20	34.3	1.3	4.24E+07	0.8	0.1
OP20	60	1.59	1.087	0	7	20	95.8	1.1	1.04E+08	92.7	1.7
OP21	60	1.59	1.087	100	7	20	75.5	1.1	1.00E+08	33.9	1.3
OP22	60	1.59	1.087	200	7	20	56.9	1.2	8.23E+07	7.3	0.2
OP23	60	1.59	1.087	300	7	20	28.5	1.4	3.15E+07	0.4	0.0

OP24	60	1.52	1.039	0	7	20	100.8	1.1	1.12E+08	134.9	2.3
OP25	60	1.52	1.039	100	7	20	83.9	1.1	1.24E+08	66.2	1.5
OP26	60	1.52	1.039	200	7	20	65.4	1.1	1.27E+08	22.8	0.3
OP27	60	1.52	1.039	300	7	20	39.4	1.2	7.25E+07	2.3	0.1
OP28	60	1.5	1.025	0	7	20	103.0	1.1	1.12E+08	148.2	3.9
OP29	60	1.5	1.025	100	7	20	86.0	1.1	1.27E+08	78.6	2.2
OP30	60	1.5	1.025	200	7	20	67.2	1.1	1.36E+08	29.4	0.6
OP31	60	1.47	1.005	0	7	20	105.0	1.1	1.14E+08	173.1	3.1
OP32	60	1.47	1.005	100	7	20	87.5	1.1	1.34E+08	87.5	1.8
OP33	60	1.42	0.970	0	7	20	106.9	1.1	1.18E+08	194.4	4.1
OP34	60	1.42	0.970	100	7	20	89.6	1.1	1.41E+08	105.2	1.7
OP35	60	1.42	0.970	200	7	20	70.2	1.1	1.48E+08	40.2	1.7
OP36	60	1.36	0.929	0	7	20	107.6	1.1	1.22E+08	211.1	3.5
OP37	60	1.36	0.929	100	7	20	89.9	1.1	1.41E+08	111.1	1.7
OP38	60	1.36	0.929	200	7	20	62.2	1.1	1.47E+08	28.2	0.5
OP39	60	1.32	0.902	0	7	20	105.9	1.1	1.23E+08	207.7	3.0
OP40	60	1.32	0.902	100	7	20	85.9	1.1	1.43E+08	106.9	1.7
OP41	60	1.32	0.902	200	7	20	53.9	1.1	1.39E+08	17.1	0.3
OP42	60	1.2	0.820	0	7	20	86.1	1.1	1.50E+08	150.1	3.9
OP43	60	1.1	0.752	0	7	20	67.7	1.1	1.50E+08	57.8	2.0
OP44	60	1	0.683	0	7	20	50.7	1.1	1.27E+08	12.6	0.3
OP45	60	1.55	1.059	0	7	20	101.6	1.1	1.00E+08	124.1	1.8

8.2 Curriculum Vitae

Name	Marcus Purfürst
Date of birth	10.03.1988, Schleiz
Nationality	German
Family status	married (one child)
Email	marcus.purfuerst@uni-leipzig.de

EDUCATION

08/2013 – 04/2018	<p>PhD Studies</p> <p>Universität Leipzig, Faculty of Physics and Earth Sciences (Prof. Dr. Marius Grundmann) and Faculty of Chemistry and Mineralogy (Prof. Dr. Roger Gläser)</p> <p>Topic of Research: <i>Influence of soot on SCR-coated diesel particulate filters</i></p> <p>Thesis submission at Faculty of Physics and Earth Sciences, Universität Leipzig, May 2017</p> <p>Alumnus of the Graduate School Build MoNa (Leipzig School of Natural Sciences – Building with Molecules and Nano-objects) – Universität Leipzig</p>
10/2011 – 07/2013	<p>Master in Physics</p> <p>Universität Leipzig, Faculty of Physics and Earth Sciences (Prof. Dr. Marius Grundmann)</p> <p>Topic of thesis: <i>Preparation and Characterization of Ultraviolet Photodiodes based on Gallium-Indium-Oxide</i></p>
10/2008 – 09/2011	<p>Bachelor in Physics</p> <p>Universität Leipzig, Faculty of Physics and Earth Sciences (Prof. Dr. Marius Grundmann)</p> <p>Topic of thesis: <i>Photoluminescence Investigation on Quantum-Well-Structures</i></p>
08/2004 – 07/2007	<p>A level</p> <p>Technisches Gymnasium, BSZ e.o. plauen, Uferstraße 8, 08527 Plauen</p>
08/1988 – 07/2004	Intermediate School
08/1994 – 07/1998	Primary School

WORK EXPERIENCE

10/2017 – Present	<p>Software Calibration Engineer</p> <p>Vistec Electron Beam GmbH, Ilmstraße 4, 07743 Jena</p>
09/2015 – 09/2017	<p>Development Engineer</p> <p>IAV GmbH, TP-TF2 (Prof. Dr. K.-J. Langeheinecke), Rockwellstraße 16, 38518 Gifhorn</p>
08/2013 – 07/2015	<p>Research Assistant</p> <p>Universität Leipzig, Institute of Chemical Technology, Linnéstraße 3, 04103 Leipzig</p> <p>PhD-work as industrial cooperation to IAV GmbH (Prof. Dr. K.-J. Langeheinecke)</p>
08/2012 – 02/2013	<p>Internship</p> <p>Leibniz-Institute of Tropospheric Research, Permoserstraße 15, 04318 Leipzig</p> <p>Development of a MATLAB-tool for statistical analyses of measured and simulated data</p>
02/2012 – 03/2012	<p>Internship</p> <p>Solarion AG, Ostende 5, 04288 Leipzig</p> <p>Experimental characterization of CIGS thin-layer solarcells</p>
08/2007 – 05/2008	<p>Alternative service</p> <p>Youth-Hostel Plothen, Hausteichstraße 1, 07907 Plothen</p>

8.3 List of Publications

8.3.1 Oral Presentations

- M. Purfürst, S. Naumov, K.-J. L., R. Gläser, *Influence of Soot of SCR-Coated Diesel Particulate Filters*, Annual Conference of the Graduate School BuildMoNa, Leipzig, March 23rd to 24th, 2015.
- M. Purfürst, S. Naumov, K.-J. Langeheinecke, R. Gläser, *Influence of Soot on Species Transport Mechanism inside the Filterwall of SDPFs*, 24th North American Catalysis Society Meeting, Pittsburgh (Pennsylvania), June 14th to 19th, 2015.
- M. Purfürst, S. Naumov, K.-J. Langeheinecke, R. Gläser, *Influence of Soot on the Transport Mechanisms inside the Filter Wall of SCR-Coated Diesel Particulate Filters*, 6th International Conference on MinNOx, Berlin, June 22nd to 23rd, 2016.

8.3.2 Journal Publications

- H. von Wenckstern, D. Splith, M. Purfürst, Z. Zhang, Ch. Kranert, S Müller, M. Lorenz and M. Grundmann, *Structural and optical properties of (In,Ga)2O₃ thin films and characteristics of Schottky contacts thereon*, 2015, *Semicond. Sci. Technol.* 30 024005, doi:10.1088/0268-1242/30/2/024005
- M. Purfürst, S. Naumov, K.-J. Langeheinecke and R. Gläser, *Influence of soot on ammonia adsorption and catalytic DeNO_x-properties of diesel particulate filters coated with SCR-catalysts*, 2017, *Chem. Eng. Sci.* 168, p. 423-436, doi:10.1016/j.ces.2017.04.052

8.3.3 Poster Presentations

- R. Eschrich, J. Böhm, D. Worch, M. Purfürst (Presenter), J. Schröder, F. Hartmann, F. Müller-Langer, R. Gläser, *Simulating the Deactivation of DOCatalysts by Varying Material Properties*, GT Power Conference, Frankfurt a. M., October 10th, 2014.
- M. Purfürst, S. Naumov, K.-J. Langeheinecke, R. Gläser, *Influence of Soot of SCR-Coated Diesel Particulate Filters*, 48. Jahrestreffen Deutscher Katalytiker, Weimar, March 11th to 13th, 2015.
- M. Purfürst, S. Naumov, K.-J. Langeheinecke, R. Gläser, *Impact of Soot on the Catalytic Activity of SCR-Coated Diesel Particulate Filters*, Annual Conference of the Graduate School BuildMoNa, Leipzig, March 14th to 15th, 2016.
- M. Purfürst, S. Naumov, K.-J. Langeheinecke, R. Gläser, *Impact of Soot on the Catalytic Activity of SCR-Coated Diesel Particulate Filters*, Annual Conference of the Graduate School BuildMoNa, Leipzig, March 6th to 7th, 2017.